THE UNIVERSITY OF QUEENSLAND
AUSTRALIA

Quantum metrology in curved space-time

Sebastian Kish
B.Sc. (Hons)

A thesis submitted for the degree of Doctor of Philosophy
at
The University of Queensland in 2019
School of Mathematics and Physics

Abstract

The precision of physical parameters is fundamentally limited by irreducible levels of noise set by quantum mechanics. Quantum metrology is the study of reaching these limits of noise by employing optimal schemes for parameter estimation. Techniques in quantum metrology can assist in developing devices to measure the fundamental interplay between quantum mechanics and general relativity at state-of-the-art precision. An example of this is the recent detection of gravitational waves by the LIGO interferometer. In this thesis, we focus on using quantum metrology for estimating space-time parameters. We show the optimal quantum resources that are needed for estimating the gravitational redshift of light propagating in the Schwarzschild space-time of Earth including the inevitable losses due to atmospheric distortion. We also propose a quantum interferometer using higher order Kerr non-linearities to improve the sensitivity of estimating gravitational time dilation. In principle, we would be able to downsize interferometers and probe gravity over a small scale potentially making it practical for measuring gravitational gradients. We then study the interesting features of the metric around a rotating massive body known as the Kerr metric and propose implementing a stationary interferometer to measure the effect of frame dragging. Finally, we consider loss in the visibility of quantum interference of single photons in rotating reference frames, and analogously in the Kerr metric. In essence, the quantum interference of photons will be affected by the relativistic effect of rotation. We find experimentally feasible parameters requiring long optical fibre for long coherence lengths of photons. Our results will hopefully contribute to the efforts of building future quantum technologies that will enter a new regime where general relativistic effects can be measured.

Declaration by author

This thesis is composed of my original work, and contains no material previously published or written by another person except where due reference has been made in the text. I have clearly stated the contribution by others to jointly-authored works that I have included in my thesis.

I have clearly stated the contribution of others to my thesis as a whole, including statistical assistance, survey design, data analysis, significant technical procedures, professional editorial advice, financial support and any other original research work used or reported in my thesis. The content of my thesis is the result of work I have carried out since the commencement of my higher degree by research candidature and does not include a substantial part of work that has been submitted to qualify for the award of any other degree or diploma in any university or other tertiary institution. I have clearly stated which parts of my thesis, if any, have been submitted to qualify for another award.

I acknowledge that an electronic copy of my thesis must be lodged with the University Library and, subject to the policy and procedures of The University of Queensland, the thesis be made available for research and study in accordance with the Copyright Act 1968 unless a period of embargo has been approved by the Dean of the Graduate School.

I acknowledge that copyright of all material contained in my thesis resides with the copyright holder(s) of that material. Where appropriate I have obtained copyright permission from the copyright holder to reproduce material in this thesis and have sought permission from co-authors for any jointly authored works included in the thesis.

Publications included in this thesis

1. **S. P. Kish**, T. C. Ralph, *Estimating space-time parameters with a quantum probe in a lossy environment*, Phys. Rev. D 93, 105013 (2016).
2. **S. P. Kish**, T. C. Ralph, *Quantum limited measurement of space-time curvature with scaling beyond the conventional Heisenberg limit*, Phys. Rev. A 96, 041801(R) (2017).
3. **S. P. Kish**, T. C. Ralph, *Quantum metrology in the Kerr metric*, Phys. Rev. D 99, 124015 (2019).

Submitted manuscripts included in this thesis

None.

Other publications during candidature

No other publications

Contributions by others to the thesis

No contributions by others

Statement of parts of the thesis submitted to qualify for the award of another degree

No works submitted towards another degree have been included in this thesis.

Research involving human or animal subjects

No animal or human subjects were involved in this research.

Acknowledgments

The first time I stepped into my supervisor's office, I came in with determination and curiosity about the new knowledge and challenges that awaited me. The journey of my PhD had taught me a great deal. It had taught me to be resilient whenever a problem arose. Although there was great satisfaction solving a problem, there was always another challenge around the corner to keep me on the ball. The many opportunities that I was given were pleasant and I thank all those that were keen to share their valuable time with me. I especially thank Tim, my supervisor, for his eternal patience, his continuing encouragement and for the stimulating discussions in our weekly meetings.

I also thank Daiqin Su, a former colleague in our group, for his patience and very humble personality. He was always ready to give up his time to teach me something new. I have encountered many people along the way and been given invaluable experiences. I thank everyone in my research group. This included Farid, Daiqin, Josephine, Estelle, Shuying, Marco, Neda and Spyros. My gratitude also goes to Joshua for helping to proofread my thesis. The environment in the office had always been welcoming and motivating. Also, I thank Austin for his charismatic leadership of the group meetings. He has been excellent associate advisor and had helped me guide my thesis in the right direction. I want to also thank Kaerin Gardner for taking care of the financial issues, and for also being a warm and kind person.

Last but not least, I would like to thank my parents and sister for their support. They have provided me with the opportunities to pursue this path.

Financial support

This research was supported in part by the Australian Research Council Centre of Excellence for Quantum Computation and Communication Technology (Project No. CE110001027) and financial support by an Australian Government Research Training Program Scholarship.

Keywords

quantum metrology, space-time curvature, space-time parameters, general relativity, Kerr metric, beyond Heisenberg limit, relativistic quantum information

Australian and New Zealand Standard Research Classifications (ANZSRC)

ANZSRC code: 020603, Quantum Information, Computation and Communication , 30%
ANZSRC code: 020604, Quantum Optics, 30%
ANZSRC code: 020105, General Relativity and Gravitational Waves, 40%

Fields of Research (FoR) Classification

FoR code: 0201, Astronomical and Space Sciences , 30%
FoR code: 0206, Quantum Physics , 70%

Contents

List of figures

List of abbreviations and symbols

Abbreviations	
GEO	Geosynchronous equatorial orbit
GR	General Relativity
HOM	Hong-Ou-Mandel
LEO	Low Earth orbit
QCR	Quantum-Cramer Rao (Bound)
QFI	Quantum Fisher Information
QFT	Quantum Field Theory
SNL	Standard noise limit
SQL	Standard quantum limit
TMSV	Two-mode squeezed vacuum

Symbols	
r_s	Schwarzschild radius
a	Kerr angular momentum
$f(\omega)$	Mode frequency profile
τ	Proper time
$\hat{a}$	Annihilation operator
α	Coherent amplitude
$\hat{\rho}$	Density operator
$\hat{x}$, $\hat{X}$	Position quadrature
$\hat{p}$, $\hat{P}$	Momentum quadrature
$\mathcal{H}(\theta)$	Quantum Fisher Information
$\mathcal{F}(\theta)$	Fidelity

The important thing in science is not so much to obtain new facts as to discover new ways of thinking about them.

-Sir William Bragg (in H. J. Eysenck, *Extracted from Genius: The Natural History of Creativity*, Cambridge: Cambridge University Press, 1995, p. 1)

Chapter 1

Introduction

The aim of this thesis is to provide the building blocks of unprecedented high precision measurements in the overlap of quantum physics and general relativity. Quantum technologies are becoming increasingly significant and relevant in the everyday world. The impact of these new technologies has already been realized by both public and private institutions. A new quantum revolution has begun to take place. In particular, quantum computers are on their way to outperform classical computers [1], quantum cryptography will ensure secure communication channels [2], quantum sensors will bring a new quantum age of sensitive devices that can measure minuscule forces [3] and quantum enhanced interferometers that measure extremely tiny changes in distances [4]. Furthermore, quantum clocks will provide highly sensitive tests of general relativity [5] as well as practical corrections to the global positioning system [6]. However, we have yet to fully unlock the advantages of using quantum mechanics to make precise measurements of relativistic phenomenon. The recent astonishing detection of gravitational waves by the LIGO detector is a significant step towards this direction [7]. Future enhancement of LIGO will be able to "hear" chirps of distant sources of gravitational waves with much better precision using quantum resources [8]. The advent of the new quantum technologies behind this improvement will lead the way to the emerging field of gravitational wave observational astronomy. This is paramount and comparable to the first time Galileo used optical telescopes for astronomical observations.

In this thesis, we will apply quantum metrology to the measurement of general relativistic effects. Quantum metrology is the study of measuring physical parameters near noise limits set by quantum mechanics. In particular, it entails enhancing the sensitivity of a measurement by exploiting quantum resources such as entanglement and squeezing. We will focus on developing tools for quantum enhanced metrology of the gravitational redshift, the Schwarzschild radius r_s, and the rotating Kerr rotating parameter a.

The thesis is organized as follows. In Chapter 2, we introduce quantum metrology in the non-relativistic setting. We show the concepts of quantum parameter estimation, and the merits of using Gaussian states for quantum metrology. Finally, we review the quantum limits of the phase noise in interferometry. Next, in Chapter 3 we review the foundations of general relativity and investigate solutions to the Einstein equation. We focus on tests of general relativity and estimating relativistic parameters in curved space-time.

In Chapter 4, we apply quantum metrology techniques to the estimation of the Schwarzschild radius r_s. We show the optimal energy resources and squeezing that are needed for light propagating in the Schwarzschild space-time of Earth including the inevitable losses due to atmospheric distortion. This would provide useful tools for Earth-to-satellite based quantum experiments. In Chapter 5, we propose a new quantum interferometer using higher order Kerr nonlinearities to improve the sensitivity of estimating r_s. In principle, we would be able to downsize interferometers by adding nonlinearities and probe gravity over a small scale potentially making it practical for measuring gravitational gradients. In Chapter 6, we then study the interesting features of the metric around a rotating massive body known as the Kerr metric. We make use of the anisotropy of light to measure the Kerr rotation parameter a. We determine the quantum limits of estimating this parameter. As a possible implementation, we consider a stationary Mach-Zehnder interferometer set at a dark port that measures a phase due to the anisotropy of light. In Chapter 7, we study the quantum effects of single photon systems in the Kerr metric and rotating reference frames. We considered the superposition of a co- and counter-propagating photon around the Kerr space-time of a rotating planet. We have proven that we can simulate this space-time using a rotating reference frame i.e. a rotating turntable. We proposed to use the Hong-Ou-Mandel (HOM) effect to measure the visibility loss of quantum interference due to the time difference between co- and counter- propagating photons on a rotating turntable. The importance of this is that a relativistic effect due to rotation has not yet been observed in a purely quantum mechanical setting. Finally, in Chapter 8, we conclude with a discussion of the impact of our work thus far, and consider unanswered questions for future research.

Bibliography

[1] *Quantum Computing in the NISQ era and beyond*, J. Preskill, Quantum **2**, 79 (2018).

[2] *Security of Quantum Key Distribution*, R. Renner, International Journal of Quantum Information Vol. **6**, No. 1 1127 (2008) .

[3] *Quantum lock-in force sensing using optical clock Doppler velocimetry*, R. Shaniv, R. Ozeri, Nature Communications volume **8**, Article number: 14157 (2017).

[4] *Squeezed states of light and their applications in laser interferometers*, R. Schnabel, Physics Reports **684**, 1-51 (2017).

[5] *Entanglement of quantum clocks through gravity*, E. C. Ruiz, F. Giacomini, C. Brukner, PNAS **114** (12) E2303-E2309 (2017).

[6] *Relativity in the Global Positioning System*, N. Ashby, Living Rev Relativ. **6**(1): 1 (2003).

[7] *Observation of Gravitational Waves from a Binary Black Hole Merger*, B. P. Abbott et al., Phys. Rev. Lett. **116**, 061102 (2016).

[8] *Enhanced sensitivity of the LIGO gravitational wave detector by using squeezed states of light*, J. Aasi, J. Abadie, et al. Nature Photonics **7**, 613-619 (2013).

Chapter 2

Quantum Metrology

Metrology is the study of the measurement of physical parameters with a particular focus on the ultimate precision of the measurement process. In the past, metrology focused on measuring physical parameters using the classical wave nature of light or systems of a mechanical nature [1, 2]. Classical noise sources place the limits on the precision of metrology for these types of systems. For actual physical systems, even after eliminating classical noise, intrinsic quantum mechanical noise becomes important. For example, in optics the vacuum fluctuations can limit precision of all parameter estimations. More recently, it has been shown that non-linear interactions of the vacuum state with a parametric down-converter generate non-classical quantum states of light called *squeezed states*, with quantum noise less than the vacuum for particular measurements [3]. If such states are used for metrology, exploiting the properties of quantum states will be essential for maximizing the advantages in measurement schemes of physical parameters.

2.1 Introduction

A typical metrological scheme for estimating a physical parameter is divided into three parts: the probe state preparation, the physical interaction which directly or indirectly depends on the physical parameter and finally, the measurement. This scheme is limited by sources of noise. The noise can be systematic due to lack of control of the probe or measurement device. Inevitably, there are also fundamental sources of noise set by Heisenberg uncertainty relations. In quantum optics, the semi-classical coherent probe state has quantum noise equivalent to the vacuum shot noise leading to the standard quantum limit (SQL). Going beyond this limit for phase estimation requires the use of non-classical states such as squeezing and entanglement which attain the *Heisenberg* limit. In quantum metrology, these limits have been studied extensively for the estimation of phases and other parameters.

In this chapter, we will review the quantum information techniques for obtaining the quantum error bound of a physical parameter. We present the quantum Fisher Information (QFI) as a way to characterize the maximum amount of information obtained by the optimal measurement, without necessarily knowing the measurement explicitly. We express the QFI in a useful way for the purpose of using continuous variable Gaussian states as the initial probe states. We review the properties of Gaussian states and the basic tools of quantum optics from a simple phase interaction to non-linear quadratic unitary evolutions. Next, we will review the standard quantum limit (SQL) which scales as $\frac{1}{\sqrt{N}}$ where N are the total resources (i.e. the total photon number). Furthermore, we can go beyond this scaling using non-classical squeezed states, and attain the so-called Heisenberg limit. We also mention that encoding physical parameters in non-linear Hamiltonians, in principle, could scale beyond this limit.

2.2 Quantum limits in interferometry

Interference of light is the pillar of the field of optics. Fundamentally, light interference is the observation of changes of intensity between two overlapping light waves with different phases. Numerous applications of interferometry range from measuring medium distortions, accelerations, and rotations to length changes due to passing gravitational waves [4–6]. In metrology, we are concerned with the sensitivity of the interference fringes to very small phase changes. Estimation of the phase difference using interferometry will give information about how a physical parameter x affected the path of the probe. In classical theory, there are no fundamental restrictions on the noise of a measurement device and thus the precision of the physical parameter x, in theory, can converge rapidly without restriction to an arbitrary small value for increasing number of measurements. Precision here is defined as the standard deviation of the mean. However, quantum mechanics places fundamental restrictions on the noise of a measurement device. This limits the rate at which the precision increases with the number of measurements.

In semi-classical theory, detectors are quantized and the measurement process is a statistical average of the photon number. A ubiquitous semi-classical state used in optics is the coherent state which exhibits Poissonian statistics with photon number variance $\Delta N^2 = \langle N \rangle$. Thus the relative uncertainty of the phase is $\Delta\phi \propto \Delta N / \langle N \rangle = 1/\sqrt{\langle N \rangle}$ known as the *shot noise* or *standard quantum limit* (SQL). In the simplest case, this is the limitation of the sensitivity of optical interferometers. For example, LIGO is currently limited by shot noise in the relevant frequency band for gravitational wave detection [5]. The shot noise limit is not regarded as a fundamental limit when non-classical quantum states of light are considered.

In quantum metrology, the non-classicality of quantum states is exploited to enhance parameter estimation beyond scaling achievable by the standard quantum limit. The use of squeezed states of light enhances phase estimation by reducing photon number fluctuations to sub-Poissonian statistics. A squeezed vacuum in one of the input ports of a Mach-Zehnder interferometer along with a coherent state beats the classical limit with $\propto 1/N^{2/3}$ [7]. Two-mode squeezed coherent states were first shown to have the phase sensitivity scale as $1/N$ [7–9]. This latter scaling is known as *Heisenberg scaling.* The NOON state was also claimed to saturate this limit which was formally proven by Bollinger *et al. in 1996* [10]. More generally, for estimation of phase parameters i.e. ϕ encoded in the unitaries of N single particle Hamiltonians $U_\phi^N = \exp\left(-i\hat{H}\phi\right)^{\otimes} N$, were shown to have similar bounds in both atomic and optical interferometry [11]. Heisenberg scaling is the maximally achievable precision of the phase in quantum interferometery [12–15].

It is not always clear what the optimal measurement scheme is that achieves the best possible precision. The estimation theory underpinning quantum parameter estimation is aimed to answer this question. Given a quantum state, the ultimate quantum limits of the phase precision can be quantified using the quantum Fisher Information (QFI) which already includes an optimization over all the possible measurements. This approach avoids the need for introducing the *quantum phase operator* representing the phase observable (in analogy to the momentum or position operator), which introduces mathematical difficulties [16, 17]. The popularity of using the QFI was exemplified by a seminal paper by Braunstein and Caves [18] that establishes the relation between statistical distances of quantum states and the QFI of the estimated parameter. More recently, this has become a very common approach in Gaussian quantum metrology [19,20]. When considering the effects of decoherence or loss, the fundamental bounds change and the optimal estimation strategies remain an open question. In lossy optical interferometry, in the limit of large photon number, the standard deviation of the phase approaches $\Delta\phi \geq \sqrt{(1-\eta)(\eta N)}$ where η is the transmission probability for photons through the interferometer [21]. The use of non-classical states such as a squeezed state vacuum input interfering with a coherent state was shown to operate near this lossy limit in the interferometric gravitational wave detector GEO600 [22].

The Heisenberg limit applies when the phase parameter ϕ is encoded in the unitary $\hat{U} = e^{i\phi\hat{H}}$ where $\hat{H} = \hat{a}^{\dagger}\hat{a}$ is a "linear Hamiltonian", defined as a quadratic dependence on the creation and annihilation operators. However, parameters encoded in non-linear Hamiltonians $\hat{H}_q = \chi^{(q)}(\hat{a}^{\dagger}\hat{a})^q$ were shown to exhibit scaling beyond the conventional Heisenberg limit [23]. These claims have generated some controversy [24–26]. Nonetheless, atomic spin-based experiments have demonstrated that the conventional Heisenberg scaling can be beaten [27].

2.3 Quantum Parameter Estimation

We now consider the estimation theory of parameters in quantum systems. Of particular importance is the estimation of a continuous parameter θ, (e.g. a phase shift) that governs the evolution of states ρ_θ of a quantum system S. The density operator ρ_θ describes the full quantum state that can be either pure or mixed.

We initially make a measurement on S to gain information about θ. These measurement operators form a general Positive Operator Valued Measure (POVM) [28]. A POVM is characterized by a set of positive operators $\{E_m \geq 0\}_{m=1}^{k}$ such that $\sum_m E_M = I$ (the identity). We make $\hat{\theta}(x)$ the estimator which is a function of x, the possible outcomes of the measurement. Thus, we have the expectation value

$$E_\theta[\hat{\theta}] = \sum_x p(x|\theta)\hat{\theta}(x), \tag{2.1}$$

where $p(x|\theta)$ is the conditional probability distribution for a given set E_x of POVMs conditioned on the parameter being θ. The estimator $\hat{\theta}$ is unbiased if this expectation value is $E_\theta[\hat{\theta}] = \theta$. The variance is

$$\mathrm{Var}_\theta[\hat{\theta}] = \Delta^2\theta[\hat{\theta}] = \sum_x p(x|\theta)(\hat{\theta}(x) - E_\theta[\hat{\theta}])^2. \tag{2.2}$$

For the quantum case, the conditional probability is given by $p(x|\theta) = tr[\rho(\theta)E_x]$. For the case of the unbiased estimator, the variance simplifies to

$$\Delta^2\theta[\hat{\theta}] = E[(\hat{\theta} - \theta)^2] = \mathrm{Var}[\hat{\theta}], \tag{2.3}$$

which is equivalent to the mean squared error MSE$[\hat{\theta}]$ [29]. The Cramér-Rao bound places a lower bound on the variance of unbiased estimators [30]. This is given by

$$\Delta^2\theta[\hat{\theta}] \geq \frac{1}{MF(\theta)}, \tag{2.4}$$

where $F(\theta)$ is known as the classical Fisher information and M is the number of independent measurements. The classical Fisher information is defined as the variance of the natural logarithm of the probability function i.e. the score

$$F(\theta) = E[(\frac{\partial \log p(x|\theta)}{\partial \theta})^2|\theta] = \sum_{x \epsilon X_+} p(x|\theta)[\frac{\partial \log p(x|\theta)}{\partial \theta}]^2, \tag{2.5}$$

where the sum is over the set of possible outcomes X_+ with non-zero probability $p(x|\theta) \neq 0$. The classical Cramér-Rao bound in Eq. (2.4) is further bounded by the Quantum Cramér-Rao bound [18, 31, 32]

$$\Delta^2\theta[\hat{\theta}] \geq \frac{1}{MF(\theta)} \geq \frac{1}{M\mathcal{H}(\theta)}, \tag{2.6}$$

where $\mathcal{H}(\theta)$ is the quantum Fisher Information. Note that this inequality is obtained by repeated independent measurements M in the asymptotic limit of a large number of measurements. One makes use of the central limit theorem to include M assuming the samples of the random variable are independent and identically distributed. The quantum Cramér-Rao bound is only meaningful when one can identify the variance from the measured data with that of the expected value of the variance. This requires that sufficiently many measurements are made such that the difference between the two quantities is suppressed and in the limit of infinitely many measurements this difference vanishes. In practice, the maximum likelihood estimator (MLE) will approach the quantum Cramér-Rao bound for many independent measurements. As in Ref. [29], the measurement process begins with an educated guess of the unbiased estimator of θ. We make initial measurements near this chosen value and update this knowledge by shifting the estimator. This requires some *a priori* information by knowledge of the prior probability distribution $\mathcal{P}(\theta)$ to determine the local precision [25]. The local precision is the quantity that is minimized [18, 25]

$$P_\theta(\hat{\theta}) := \left\langle (\frac{\hat{\theta}}{|\frac{d\langle\hat{\theta}\rangle}{d\theta}|} - \theta) \right\rangle_\theta^{1/2}, \tag{2.7}$$

where the average is with respect to the conditional probability $p(\hat{\theta}|\theta)$. In this thesis, we will also consider minimizing the local precision, and in particular propose non-linear schemes which exceed the Heisenberg scaling. In quantum interferometry, a controlled experiment would be designed to be in the local precision regime, for example, in an interferometer, by calibration to a dark port of zero intensity.

2.4 Quantum Fisher Information

The classical Fisher Information is defined for any given probability distribution. However, as a result of the Braunstein-Caves inequality there is an upper bound to the Fisher information which doesn't depend on the specific POVM performed on the system but on the properties of the evolved density operator [18]. This is known as the quantum Fisher Information $\mathcal{H}(\theta)$. Formally, it is defined as

$$\mathcal{H}(\theta) = tr[\rho(\theta)\lambda(\theta)^2], \tag{2.8}$$

where the symmetric logarithmic derivative (SLD) λ is Hermitian and satisfies the equation

$$\frac{\partial\rho(\theta)}{\partial\theta} = -i[G, \rho(\theta)] = \frac{1}{2}[\lambda(\theta)\rho(\theta) + \rho(\theta)\lambda(\theta)], \tag{2.9}$$

where G is the generator of the initial set of states $\rho(0)$. For example, we are usually interested in estimating a linear phase, in which case the generator is the number operator $G = a^\dagger a$ and the evolved *pure* state encodes the parameter θ in the following way

$$\rho(\theta) = e^{-i\theta G}\rho(0)e^{i\theta G}. \tag{2.10}$$

The SLD turns out to be $\lambda(\theta) = -2i[G, \rho(\theta)]$ for pure states. The quantum Cramér-Rao bound in Eq. (2.6) generalizes to include optimality over all possible quantum measurements. Unlike previous approaches, there is also no need to calculate eigenstates for the phase operator in estimating a phase, and only knowledge of the generator G is needed to calculate the QFI [29].

However, the quantum Fisher Information in Eq. (2.8) can be re-expressed in terms of the Uhlmann fidelity of the density operators $\rho(\theta + d\theta)$ and $\rho(\theta)$. The equivalence between the quantum Fisher Information matrix and the Bures distance between two density matrices has been extensively studied [18]. In this definition, the Bures distance represents the minimal distance between purifications of the density operators $\rho(\theta + d\theta)$ and $\rho(\theta)$

$$d_B(\rho(\theta + d\theta), \rho(\theta)) = [2(1 - \sqrt{\mathcal{F}(\rho(\theta + d\theta), \rho(\theta))}\,)]^{\frac{1}{2}}, \tag{2.11}$$

where $\mathcal{F}$ is the Uhlmann's fidelity defined as

$$\mathcal{F}(\rho, \sigma) = (Tr(\sqrt{\sqrt{\rho}\,\sigma\sqrt{\rho}}\,))^2. \tag{2.12}$$

The QFI is related to the Bures distance via [18]

$$\mathcal{H}(\theta) = \lim_{d\theta \to 0} \frac{8(1 - \sqrt{\mathcal{F}(\rho(\theta + d\theta), \rho(\theta))}\ )}{d\theta^2}. \tag{2.13}$$

The advantage of using this definition is that the fidelities of Gaussian states have a closed form [20, 33].

2.5 Basic Operations in Quantum Optics

Quantum states of the electromagnetic field can be described by orthogonal modes distinguished by their properties in space, time and polarization. Since photons are bosons, these modes can be occupied by any number of photons. A general quantum state of light with M modes can be described with the density operator [16]

$$\begin{aligned}\hat{\rho} = &\sum_{n_1,n_2,n_3,...,n_M,n'_1,n'_2,n'_3,...,n'_M} \rho_{n_1,n_2,n_3,...,n_M;n'_1,n'_2,n'_3,...,n'_M} |n_1, n_2, n_3, ..., n_M\rangle \langle n'_1, n'_2, n'_3, ..., n'_M|,\\ &Tr(\hat{\rho}) = 1, \rho_{n_1,n_2,n_3,...,n_M=n'_1,n'_2,n'_3,...,n'_M} \geq 0,\end{aligned} \tag{2.14}$$

where we have used the Fock basis $|n_1\rangle \times \ldots \times |n_M\rangle$ representing n_i photons occupying the $i-th$ mode. This is a mixed state with probability given by the diagonal matrix elements $\rho_{n_1,n_2,n_3,...,n_M=n'_1,n'_2,n'_3,...,n'_M}$ of being in the pure state $|n_i\rangle$. In terms of the annihilation and creation operators $\hat{a}_i$,$\hat{a}_i^\dagger$, with commutation relation $[\hat{a}_i, \hat{a}_j^\dagger] = \delta_{ij}$

$$|n_i\rangle = \frac{(\hat{a}_i^\dagger)^n}{\sqrt{n!}} |0\rangle, \hat{a}_i |n_i\rangle = \sqrt{n_i}\ |n_i - 1\rangle, \hat{a}_i^\dagger |n_i\rangle = \sqrt{n_i + 1}\ |n_i + 1\rangle, \tag{2.15}$$

where $|0\rangle$ describes the vacuum state. If we consider an interferometer, the photons propagate in two separate arms corresponding to two orthogonal modes. In addition, we can modify the state in one of the arms by adding beam-splitters, linear phase-delays or non-linear optical elements. Finally, we detect photons at the output of the interferometer to determine the phase difference θ of the two modes. The output states of the modes are sensitive to this phase difference of the interferometer and one may hence able to make an estimate of the phase θ from the detection events.

In this section, we review how the beamsplitter evolution transforms the quantum optical field modes. The beamsplitter is an essential element that works as an interferometric device, a quantum entangler and also for Bell measurements [15].

Additionally, we consider a basic Mach-Zehnder interferometer where the unitary operator,

$$\hat{U}_\theta = e^{-i\theta\hat{a}^\dagger\hat{a}}, \tag{2.16}$$

acts on one of the arms to add a phase and interferes on a beamsplitter.

2.5.1 Beamsplitter

A quantum beamsplitter transforms the input modes of the annihilation operators a_1 and b_1 [1] in the following way

$$\hat{a}_1 = t\hat{b}_2 + \sqrt{1-t^2}\,\hat{a}_2, \tag{2.17}$$

$$\hat{b}_1 = t\hat{b}_2 - \sqrt{1-t^2}\,\hat{a}_2. \tag{2.18}$$

Where t is the transmission coefficient of the beamsplitter. Also, a_2 and b_2 are the annihilation operators of the output modes of the beamsplitter. Let's consider the following input state

$$|\psi\rangle_{in} = |n\rangle\,|m\rangle = \frac{(a_1^\dagger)^n}{\sqrt{n!}}\frac{(b_1^\dagger)^m}{\sqrt{m!}}\,|0\rangle\,|0\rangle\,. \tag{2.19}$$

Then, we rewrite the output state using the transformation of the adjoint operators

$$|\psi\rangle_{out} = \frac{(t\hat{b}_2^\dagger + \sqrt{1-t^2}\,\hat{a}_2^\dagger)^n}{\sqrt{n!}}\frac{(t\hat{b}_2^\dagger - \sqrt{1-t^2}\,\hat{a}_2^\dagger)^m}{\sqrt{m!}}\,|0\rangle\,|0\rangle\,. \tag{2.20}$$

Example. If one photon is in the input of mode b, $|\psi\rangle_{in} = |0\rangle_1\,|1\rangle_1$ then the output state after passing through a 50/50 beamsplitter is

$$|\psi\rangle_{out} = \frac{|1\rangle\,|0\rangle - |0\rangle\,|1\rangle}{\sqrt{2}}, \tag{2.21}$$

representing a superposition of a photon being detected in the output mode a_2 or mode b_2. These two modes are entangled. In comparison to having a classical source of light as the input such as one coherent state and a vacuum state $|\alpha\rangle\,|0\rangle$ with amplitudes α, the amplitudes change and half the intensity is detected simultaneously in both modes but the output state is unentangled. A beamsplitter can also represent channel loss in the amplitude of a quantum state.

2.5.2 Mach-Zehnder interferometer

An important element in quantum interferometry is the phase-shifter unitary $\hat{U}_\theta = e^{i\hat{N}\Phi}$ where $\hat{N} = a^\dagger a$ is the number operator. A Mach-Zender interferometer

[1] We note that we drop the operator hat $\hat{a}$ from this point forward.

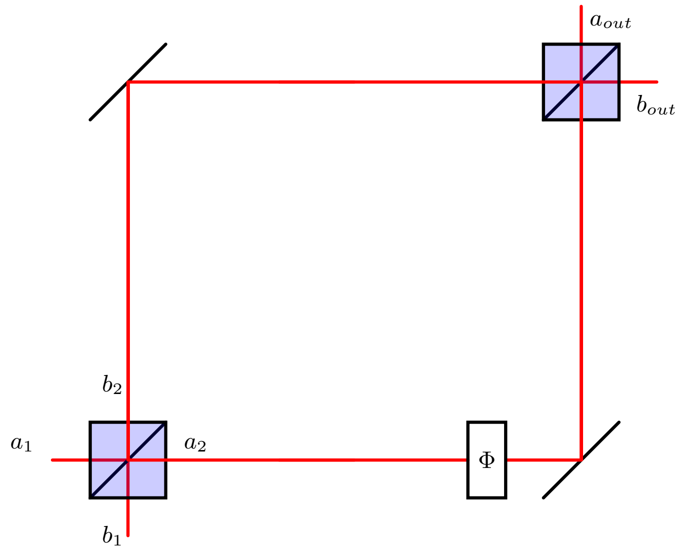

Figure 2.1: A Mach-Zehnder interferometer with input modes a_1, b_1 and output modes a_{out}, b_{out}. Φ is a phase shifter in the bottom arm.

has a beamsplitter and then two arm modes with one of the arms having a phase shifter Φ as seen in Fig. 2.1. The two modes interfere on a second beamsplitter and the output port photon intensity is measured. The output modes are given by the following

$$\begin{aligned} a_{out} &= \frac{1}{2}((1+e^{i\Phi})a_1 + (1-e^{i\Phi})b_1), \\ b_{out} &= \frac{1}{2}((1+e^{i\Phi})a_1 - (1-e^{i\Phi})b_1). \end{aligned} \tag{2.22}$$

These relations are important for calculating the evolution for all kinds of input probe states of the Mach-Zehnder interferometer, and in particular for determining precision bounds on the phase Φ in quantum metrology. For example, for a single coherent state input the probability of detection of the output modes is therefore

$$P_A = \frac{\langle \hat{N}_A \rangle}{N} = (1 - \cos\Phi), \tag{2.23}$$

where $\langle \hat{N}_A \rangle = \langle a_A^\dagger a_A \rangle$ is the number expectation value of output A and $N = N_A + N_B$. Similarly,

$$P_B = \frac{\langle \hat{N}_B \rangle}{N} = (1 + \cos\Phi), \tag{2.24}$$

where $\langle \hat{N}_B \rangle = \langle a_B^\dagger a_B \rangle$ is the number expectation value of output B.

2.6 Gaussian states

Gaussian states are defined as continuous variable (CV) states that are completely characterized by their first and second order quadrature moments in phase space. For a single mode Gaussian state, these moments are the expectation value of the position $\langle x\rangle$, momentum $\langle p\rangle$ and their variances $\langle \Delta x^2\rangle$, $\langle \Delta p^2\rangle$ where the position quadrature is $\hat{x}_i = \frac{1}{\sqrt{2}}(\hat{a}_i^\dagger + \hat{a}_i)$ and momentum quadrature is $\hat{p}_i = \frac{i}{\sqrt{2}}(\hat{a}_i^\dagger - \hat{a}_i)$. Additionally, there could be covariances of $\hat{x}$ and $\hat{p}$, but this can always be diagonalized with a suitable choice of quadratures. We note Gaussian states are quantum states that can be used for many applications in experimental quantum physics. In quantum optics, non-classical Gaussian states can be prepared using a classical pump field input to a non-linear optical medium which could potentially entangle the output. This output state can be used in quantum information protocols [34] and quantum cryptography. Squeezed states exhibit noise below shot noise that can be used for enhancing parameter estimation in quantum metrology. Additionally, the mathematical description of Gaussian states can be represented in phase space diagrams from the first moments and the symplectic eigenvalues of the covariance matrix that fully determine the state.

Gaussian states are characterized by the covariance matrix and the vector of first moments. The covariance matrix σ (of dimension $2M$) has components given by

$$\sigma_{i,j} = \frac{1}{2}\left\langle \hat{z}_i\hat{z}_j + \hat{z}_j\hat{z}_i\right\rangle - \left\langle \hat{z}_i\right\rangle\left\langle \hat{z}_j\right\rangle, \tag{2.25}$$

where z is a vector of the phase space variables $\{x_1, p_1, \ldots, x_M, p_M\}$ and $\langle\hat{z}\rangle$ is also a vector of the mean quadrature values with components $\langle\hat{z}_i\rangle = Tr(\hat{z}_i\rho)$. For example, a two-mode Gaussian state $M = 2$ is characterized by the 4×4 real symmetric covariance matrix

$$\sigma = \begin{pmatrix} [\sigma_{11}] & [\sigma_{12}] \\ [\sigma_{21}] & [\sigma_{22}] \end{pmatrix} \tag{2.26}$$

where σ_{ij} are 2×2 matrices representing the correlations by the off-diagonal terms and variances by the diagonal terms between the i-th and the j-th modes. The first moments are the components of the vector $\langle\hat{z}\rangle = \{\langle x_1\rangle, \langle p_1\rangle, \langle x_2\rangle, \langle p_2\rangle\}$. An important property of Gaussian states is that under a unitary evolution with Hamiltonians that are at most quadratic in annihilation and creation operators, they remain Gaussian [20]. Beam-splitters, phase-shifters and squeezing operations are examples of such operations. We now consider Gaussian states that are common in quantum interferometry.

2.6.1 Coherent states

A coherent state $|\alpha\rangle$ is defined as the eigenstate of the annihilation operator. That is,

$$\hat{a}\,|\alpha\rangle = \alpha\,|\alpha\rangle\,. \tag{2.27}$$

Equivalently, we can write this state in the Fock basis by applying the displacement operator $\mathcal{D}(\alpha) = e^{\alpha a^\dagger - \alpha^* a}$ on the vacuum state. This operator can be re-written using the Baker-Campbell-Hausdorff formula as $\mathcal{D}(\alpha) = e^{-\frac{1}{2}|\alpha|^2} e^{+\alpha a^\dagger} e^{-\alpha^* a}$.

$$|\alpha\rangle = \mathcal{D}(\alpha)\,|0\rangle = e^{-|\alpha|^2/2} e^{\alpha a^\dagger}\,|0\rangle = e^{-|\alpha|^2/2} \sum_{n=0}^{\infty} \frac{\alpha^n}{\sqrt{n!}}\,|n\rangle\,, \tag{2.28}$$

where we have used the Taylor expansion $e^{\alpha a^\dagger} = \sum_{n=0}^{\infty} \frac{(\alpha a^\dagger)^n}{n!}$ to write the coherent state in the Fock basis. If we measure the photon count n, the probability follows Poissonian statistics $P(n) = |\langle n|\alpha\rangle|^2 = e^{-|\alpha|^2} \frac{|\alpha|^{2n}}{n!}$ with average $\langle n\rangle = |\alpha|^2$ and number variance $\langle \Delta n^2\rangle = |\alpha|^2$. Thus the number uncertainty is $\frac{\Delta n}{n} = \frac{1}{\sqrt{n}}$ implying that the larger the intensity, the better the precision with which the beam power can be measured [16]. Coherent states are classified as minimum uncertainty states and it can be shown the momentum and position variance satisfy the uncertainty relation

$$\langle \Delta^2 \hat{x}\rangle \langle \Delta^2 \hat{p}\rangle \geq 1, \tag{2.29}$$

where $x = \frac{1}{\sqrt{2}}(a + a^\dagger)$ is the position operator and $p = -\frac{i}{\sqrt{2}}(a - a^\dagger)$ is the momentum operator which obey the commutation relation $[\hat{x}, \hat{p}] = i$. For a coherent state $\langle \Delta^2 \hat{x}\rangle = \langle \Delta^2 \hat{p}\rangle = 1$ implying vacuum noise. Thus coherent states can therefore be represented in a phase space diagram as unit error circles (representing the quadrature variances) displaced from the origin (the vacuum state) by the real and imaginary parts of the complex amplitude α.

2.6.2 Single-mode squeezed state

In this section, we review a subset of Gaussian states with uncertainty in one quadrature less than that of a coherent state [3]. A single-mode squeezed state is generated by applying the squeezing operator on the vacuum followed by the displacement operator

$$|\alpha, \xi\rangle = \mathcal{D}(\alpha)\mathcal{S}(\xi)\,|0\rangle\,, \tag{2.30}$$

where $\mathcal{S}(\xi) = \exp(\frac{1}{2}\xi^* a^2 - \frac{1}{2}\xi (a^\dagger)^2)$ is the squeezing operator, $\xi = re^{i\theta}$ is the complex squeezing parameter and $\mathcal{D}(\alpha) = e^{\alpha a^\dagger - \alpha^* a}$. Compared to generating coherent states, squeezed states require quadratic terms in annihilation and creation operators. The variances of the quadratures for the state $|\alpha, \xi\rangle$ turn out to be

$$\langle \Delta X_\theta^2 \rangle = e^{-2r}, \tag{2.31}$$

Implying a reduction in noise below vacuum noise. And

$$\langle \Delta P_\theta^2 \rangle = e^{2r} \tag{2.32}$$

Accompanying noise is added in the other quadrature. Note that the variances don't depend on the amplitude of the coherent state. The noise of one quadrature can be below the shot noise even for fields with high intensities [3]. The average number of photons for the squeezed coherent state is

$$\langle n \rangle = |\alpha|^2 + \sinh^2 r. \tag{2.33}$$

When $\alpha = 0$ then we have a squeezed vacuum with an average number of $\langle n \rangle = \sinh^2 r$ photons. In the Fock basis, we can write the squeezed vacuum state as

$$|SMSV\rangle = \frac{1}{\sqrt{\cosh r}} \sum_{n=0}^{\infty} (-\tanh r)^n \frac{\sqrt{(2n)!}}{2^n n!} |2n\rangle. \tag{2.34}$$

Therefore, the squeezed vacuum state is a superposition of only even photon numbers.

2.6.3 Two-mode squeezed state

It is possible to generate a two-mode Gaussian state that exhibits quantum entanglement. This can be done by applying a two-mode squeezing operation on the vacuum

$$|TMSV\rangle = \hat{S}_2(\xi) |0, 0\rangle, \tag{2.35}$$

where $\hat{S}_2(\xi) = exp(\xi^* \hat{a}\hat{b} - \xi \hat{a}^\dagger \hat{b}^\dagger)$ where $\xi = |\xi| e^{i\theta}$. In the Fock basis

$$|TMSV\rangle = \frac{1}{\cosh \xi} \sum_{n=0}^{\infty} (-1)^n e^{i\theta} \tanh^n \xi \, |n, n\rangle \tag{2.36}$$

Note that this is not a product of two single mode squeezed states. The photons in both modes are correlated. If we trace out one of the modes

$$\rho_1 = Tr_2[|TMSV\rangle \langle TMSV|] = \frac{1}{\cosh^2(r)} \sum_{n=0}^{\infty} \tanh^{2n}(r) |n\rangle \langle n|, \tag{2.37}$$

which is a thermal state with average number of photons $\langle n \rangle = \sinh^2(r)$. The thermal state is a mixed state defined as $\rho^2 \neq \rho$ and $Tr(\rho^2) < 1$. Since this traced out state is mixed and formed from a global pure state, then the state $|TMSV\rangle$ cannot be written as a product state, implying that it is entangled [35].

2.6.4 Non-linear unitary

Squeezed states offer non-classical advantages to parameter estimation. The so-called Heisenberg limit can be attained with squeezed photons as the resource. However, it has been recently observed that strong non-linear interactions can enhance parameter estimation beyond the conventional Heisenberg limit [26, 36, 37]. These claims have generated some controversy [25, 38]. Nonetheless, a spin-based experimental system has demonstrated beyond Heisenberg scaling [27]. In the optical domain an example is that of probe transmission through a Kerr medium where it has been shown that estimation of the non-linear parameter, χ, can be achieved with a $\langle \Delta\chi \rangle \propto 1/N^{3/2}$ scaling [23].

For $\chi^{(3)}$ Kerr media [2], the unitary evolution is $\hat{U} = e^{i\chi\tau(a^\dagger)^2 a^2 + ia^\dagger ak\phi(\tau)}$ with $\hat{n}$ the number operator, and k the wave number of the optical mode, ϕ is the linear phase and τ is the interaction time with the Kerr medium. Hence we find that the evolution of a coherent probe state is

$$|\alpha_{NL}(\tau)\rangle = e^{-|\alpha|^2/2} \sum_{n=0}^{\infty} \frac{(\alpha e^{i\chi\tau(n+1)+ik\phi(\tau)})^n}{\sqrt{n!}} |n\rangle \, . \tag{2.38}$$

For large enough $\chi\tau$, this state is non-Gaussian, and higher order statistical moments must be taken into account. However, as in Chapter 5, we will show that an interferometer with a non-linear element can remain Gaussian for small enough $\chi\tau$, and exhibit beyond conventional Heisenberg scaling.

2.7 Balanced homodyne detection

A quantum metrology scheme also entails a final measurement that contains information about the estimated parameter. To detect squeezing of a Gaussian state, we require multiple measurements of the quadrature $\hat{X}_\theta = \hat{X}\cos\theta + \hat{P}\sin\theta = e^{-i\theta}\hat{a} + e^{i\theta}\hat{a}^\dagger$. We note that this may not be the optimal measurement to saturate the quantum Cramér-Rao bound. A typical scheme for detecting the quadrature

[2]Note that the classical Kerr effect is named after John Kerr (1875) [41] and is by no means related to the Kerr metric which was discovered by Roy Kerr (1963) [42].

is by homodyne detection initially proposed by Yuen and Chan [39]. Homodyne detection involves interference of the *signal* mode $\hat{a}_s$ with a *local oscillator* mode $\hat{a}_{LO}$. The quadrature of the signal mode is $\hat{X}(t) \propto \hat{a}(t)e^{-i\Omega t} + \hat{a}^\dagger(t)e^{i\Omega t}$ where Ω is the frequency. The local oscillator is a strong coherent laser with matching frequency Ω and quadrature $\hat{X}_{LO}(t) \propto \hat{a}_{LO}(t)e^{-i\Omega t+i\theta} + \hat{a}^\dagger(t)e^{i\Omega t-i\theta}$ where θ is a controlled phase [40]. This signal mode is interfered with the local oscillator on a symmetric 50/50 (balanced) beamsplitter. From the beamsplitter transformations in Eq. (2.18), the output modes of the beamsplitter are given by

$$a_{1,2}(t) = \frac{1}{\sqrt{2}}(a_{LO}e^{i\theta} \pm a(t)). \tag{2.39}$$

The output fields are detected by two photodiodes which subtract the photocurrents. The intensity difference is given by

$$\begin{aligned}\Delta I(t) &\propto a_1^\dagger(t)a_1(t) - a_2^\dagger(t)a_2(t) \\ &= a(t)a_{LO}^\dagger(t)e^{-i\theta} + a^\dagger(t)a_{LO}(t)e^{i\theta} \\ &\approx |\alpha|(a(t)e^{-i\theta} + a^\dagger(t)e^{i\theta}) = \alpha X_\theta,\end{aligned} \tag{2.40}$$

where we have assumed that the local oscillator is classical $a_{LO} \approx |\alpha|$ for high amplitude. Therefore, we need only control the phase θ to obtain a full description of the quadratures. Additionally, we can obtain the second statistical moments ΔX^2 and ΔP^2 from the statistics of the multiple homodyne detections.

Bibliography

[1] *Experiments to Determine the Density of the Earth*, H. Cavendish (1798).

[2] *Über einen Interferenzrefraktor*, M. Ludwig, Zeitschrift für Instrumentenkunde. **12**: 8993 (1892).

[3] *Squeezed states of light*, D.F. Walls, Nature **306**, 141 (1983).

[4] *Gravitational Wave Detection by interferometry* M. Pitkin, S. Reid, S. Rowan, and J. Hough, Living Reviews in Relativity **14** (5) (2011).

[5] *A gravitational wave observatory operating beyond the quantum shot-noise limit*, The LIGO Scientific Collaboration, Nature Physics **7** 962965 (2011).

[6] *Observation of Gravitational Waves from a Binary Black Hole Merger*, B. P. Abbott et al., Phys. Rev. Lett. **116**, 061102 (2016).

[7] *Quantum-mechanical noise in an interferometer*, C. M. Caves, Phys. Rev. D **23** (8), 1693 (1981).

[8] *SU(2) and SU(1,1) interferometers*, B. Yurke, S. L. McCall, J. R. Klauder, Phys. Rev. A **33**, 4033 (1986).

[9] *Squeezed states in phase-sensing interferometers*, R. S. Bondurant, and J. H. Shapiro, Phys. Rev. D **30**, 2548 (1984).

[10] *Optimal frequency measurements with maximally correlated states*, J. J . Bollinger, Wayne M. Itano, D. J. Wineland, and D. J. Heinzen, Phys. Rev. A **54**, R4649(R) (1996).

[11] *Squeezed-light-enhanced atom interferometry below the standard quantum limit*, S. S. Szigeti, B. Tonekaboni, W. Y. S. Lau, S. N. Hood, and S. A. Haine, Phys. Rev. A **90**, 063630 (2014).

[12] *Relativistic Quantum Teleportation with Superconducting Circuits*, N. Friis, A. R. Lee, K. Truong, C. Sabín, E. Solano, G. Johansson, and I. Fuentes, Phys. Rev. Lett. **110**, 113602 (2013).

[13] *Quantum-Enhanced Measurements: Beating the Standard Quantum Limit*, V. Giovannetti, S. Lloyd, and L. Maccone, Science **306**, 1330 (2004).

[14] *Quantum Metrology*, V. Giovannetti, S. Lloyd, and L. Maccone, Phys. Rev. Lett. **96**, 010401 (2006).

[15] *Advances in quantum metrology*, V. Giovanetti, S. Lloyd, and L. Maccone, Nature Photon. **5**, 222 (2011).

[16] *Quantum limits in optical interferometry*, R. Demkowicz-Dobrzański, M. Jarzyna, and J. Kołodyński, Progress in Optics **60**, 345 (2015).

[17] *Limiting Procedures for the Optical Phase Operator*, S.M. Barnett & D.T. Pegg, Journal of Modern Optics **39** (10), 2121 (1992).

[18] *Statistical distance and the geometry of quantum states*, S. L. Braunstein, C. M. Caves, Phys. Rev. Lett. **72**, 3439 (1994).

[19] *Quantum parameter estimation using multi-mode Gaussian states* D. Šafránek, A. R. Lee, and I. Fuentes, New J. Phys. **17**, 073016 (2015).

[20] *Quantum parameter estimation using multi-mode Gaussian states*, D. Šafránek, A. R. Lee, I. Fuentes, New J. Phys. **17** (2015).

[21] *Scaling laws for precision in quantum interferometry and the bifurcation landscape of the optimal state*, S. Knysh, V. N. Smelyanskiy, and G. A. Durkin, Phys. Rev. A **83**, 021804 (2011).

[22] *Quantum metrology for gravitational wave astronomy.*, Schnabel, R., Mavalvala, N., McClelland, D. E. & Lam, P. K., Nat. Commun. **1**, 121 (2010).

[23] *Quantum metrology for non-linear phase shifts with entangled coherent states*, J. J. K. Park, H. Jeong, W. J. Munro, K. Nemoto, T. P. Spiller, Phys. Rev. A **86**, 043828 (2012).

[24] *Nonlinear Michelson interferometer for improved quantum metrology*, A. Luis, A. Rivas, Phys. Rev. A **92**, 022104 (2015).

[25] *Does Nonlinear Metrology Offer Improved Resolution? Answers from Quantum Information Theory*, M. J. W. Hall and H. M. Wiseman, Phys. Rev. X **2**, 041006 (2012).

[26] *Nonlinear atom interferometer surpasses classical precision limit*, C. Gross, T. Zibold, E. Nicklas, J. Estve, M. K. Oberthaler, Nature **464**, 1165-1169 (2010).

[27] *Interaction-based quantum metrology showing scaling beyond the Heisenberg limit*, M. Napolitano, et al., Nature **471**, 486 (2011).

[28] *Quantum metrology from a quantum information science perspective*, G. Tóth, I. Apellaniz, J. Phys. A: Math. Theor. 47, 424006 (2014).

[29] *Optimal phase measurements with pure Gaussian states*, A. Monras, Phys. Rev. A **73**, 033821 (2006).

[30] *Mathematical Methods of Statistic*, H. Cramér, Princeton University Press, 1946.

[31] *Quantum detection and estimation theory*, C. W. Helstrom, Academic press (1976).

[32] *Probabilistic and Statistical Aspects of Quantum Theory*, A. S. Holevo, North Holland, Amsterdam (1982).

[33] *Quantum and classical fidelities for Gaussian states*, H. Jeong, T.C. Ralph, W.P. Bowen, J. Opt. Soc. Am. B **24**, 355-362 (2007).

[34] *Quantum Information with Continuous Variables*, S. L. Braunstein and A. K. Pati eds., Kluwer Academic, Dordrecht, (2003).

[35] *Quantum optics in the phase space*, S. Olivares, Eur. Phys. J. Spec. Top. **203**: 3 (2012).

[36] *Breaking the Heisenberg limit with inefficient detectors*, J. Beltrán and A. Luis, Phys. Rev. A **72**, 045801 (2005).

[37] *Generalised limits for single-parameter quantum estimation*, S. Boixo, S. T. Flammia, C. M. Caves, Phys. Rev. Lett., **98**, 090401 (2007).

[38] *General optimality of the Heisenberg limit for quantum metrology*, M. Zwierz, C. A. Perez-Delgado, P. Kok, Phys. Rev. Lett. **105**, 180402 (2010).

[39] *Noise in homodyne and heterodyne detection*, H. P. Yuen and V. W. S. Chan, Opt. Lett. **8**, 177179 (1983).

[40] *Squeezed light*, A. I. Lvovsky, arXiv preprint arXiv:1401.4118 (2016).

[41] *A new relation between electricity and light: Dielectrified media birefringent*, J. Kerr, Philosophical Magazine. 4. **50** (332): 337348 (1875).

[42] *Gravitational Field of a Spinning Mass as an Example of Algebraically Special Metrics*, R. P. Kerr, Phys. Rev. Lett. **11**, 237 (1963).

Chapter 3

General relativity and Quantum Field Theory

General relativity describes the curvature of space-time around mass and energy. It provides a description of physics that has been observed on large scales, from lengths of cosmic scales to lengths as small as 10 m and below [1–6]. Conversely, quantum theory very adequately describes physics on small scales. Independent experimental confirmation of either theory has been repeatedly successful, but fundamentally, both theories are not compatible with each other. A consistent fully quantized theory of gravity is famously elusive and even more so, relevant parameter regimes are far out of reach in today's experiments [7].

There are two important physical regimes where effects of curvature appear in quantum phenomena. One could conceive quantum experiments in highly curved space-time such as near black hole horizons. Although quantum field theory in curved space-time can adequately describe the physics in this regime, experiments would be useful to determine bounds on models of space-time micro-structures in attempts to quantize gravity. Additionally, observers with finite size detectors near a black hole could detect relativistic quantum effects of the Hawking radiation explaining the information flow of black holes, with quantum correlations playing an important role [1]. In contrast, we can consider fundamental tests of general relativity over larger scales where effects of curvature are large enough that precise quantum devices can detect them. This regime is a test bed for the overlap of quantum physics and general relativity. In the near future, quantum communication technologies such as quantum key distribution between Earth and satellites will need to consider the effects of space-time curvature as additional noise to the communication channel [8].

In the previous chapter, we focused on quantum metrology in a non-relativistic setting. The acquired phase difference in an interferometer is caused by interaction with optical elements, from dielectric material to non-linear interactions. We have assumed that these interactions occur with reference to a global clock ticking with time t. However, in special relativity and general relativity, the idea of absolute time is abandoned for (3+1) dimensional space-time. Thus, for a given quantum state of a particle we have to consider the particle's world-line in the curved space-time to compute its state evolution. In the context of metrology, this is necessary for obtaining the fundamental precision of a space-time parameter given a quantum probe.

The theoretical framework for evolving quantum states on a *flat space-time* background begins with Quantum Field Theory (QFT). Fundamentally, QFT treats particles as excited states of their quantized fields. It is expected that any potential effects of quantum gravity are negligible when the curvature is sufficiently small. Therefore, the classical description of curved space-time is sufficient. We are thus working in a *semi-classical* approximation. In particular, we can treat quantum states of light as propagating in a classical curved space-time background. Frameworks for estimating parameters of bosonic quantum fields that undergo a generic transformation were done by M. Ahmadi et al. [9], and T. G. Downes et al. [10]. Also, a more general approach to this probem where the transformations considered are also Gaussian unitaries but the probe states are not restricted to Gaussian states was done by N. Friis et al. [11].

In this chapter, we review special relativity and the constancy of the speed of light in a local reference frame. Next, we derive the fundamentals of general relativity from first principles, and introduce the essentials of general relativity in the mathematical language of metrics and tensors. We give examples of the static and rotating massive body solutions of the Einstein equations in the vacuum. Finally, we review the gravitational redshift and the propagation of wavepackets in curved space-time. The evolution of quantum states in curved space-time is vital for obtaining quantum limits on the precision of estimating space-time parameters.

3.1 Special Relativity

An inertial reference frame is a reference frame where a particle upon which no force acts is at rest or moves with a constant velocity. *The laws of physics are the* *same in every inertial reference frame.* This is the fundamental principle of relativity. Special relativity assumes the constancy of the speed of light in all inertial frames. The space-time interval in the Minkowksi spacetime is given by:

$$ds^2 = -c^2dt^2 + dx^2 + dy^2 + dz^2, \tag{3.1}$$

where we have used the metric signature $(-,+,+,+)$. The space-time of special relativity is non-Euclidean [2,3]. Inertial observers can transform between reference frames of different inertial observers via the Lorentz transformations. Boosts in the x-direction are an example of a Lorentz transformation:

$$\begin{aligned} ct' &= \gamma(ct - \beta x), \\ x' &= \gamma(x - \beta ct), \\ y' &= y, \\ z' &= z. \end{aligned} \tag{3.2}$$

where $\beta = v/c$, v is the relative velocity of the boost and $\gamma = (1-\beta^2)^{-1/2}$ is the Lorentz factor. An event A in the inertial reference frame S is defined by the coordinates (t, x, y, z). The effect of this transformation is that observers can disagree on the time order of events. For example, if two events occur simultaneously with respect to the inertial reference frame S, then they will not occur simultaneously in the initial reference frame S. With respect to the frame S, A occurs before B or B occurs before A. We note that the Minkowski metric in Eq. (3.1) is invariant under the linear transformations in Eq. (3.2). An observer is described by their world line defined by a trajectory in space and time. In flat Minkowski space-time, the distance between two points in the space-time is given by the space-time interval:

$$\Delta s^2 = -c^2\Delta t^2 + \Delta x^2 + \Delta y^2 + \Delta z^2. \tag{3.3}$$

When $\Delta s^2 = 0$, the distance between two events is referred to as *null* or light-like. All massless particles, including photons travel along null geodesics. A geodesic describes the shortest distance between two points on a surface. In flat space-time, null geodesics have the trivial solution of straight lines $\Delta x = \pm\Delta t$. When $\Delta s^2 > 0$ this implies that there is more spatial distance than time between events. Two events lie for which $\Delta s^2 > 0$ lie outside of each others light-cones and are called *space-like* separated. Conversely, when $\Delta s^2 < 0$ then events happen within the light cone and are *time-like* separated. Similarly, we can also define geodesics in a curved space-time for null geodesics $ds^2 = 0$, spacelike geodesics $ds^2 = d\rho^2$ where $d\rho$ is the proper distance and timelike geodesics $ds^2 = -d\tau^2$ where $d\tau$ is the proper time.

3.2 General Relativity

3.2.1 Equivalence principle

A particle's resistance to a force is quantified by the amount of inertial mass. It is a remarkable coincidence that the *inertial mass* is equivalent to the *gravitational mass* [2–6]. This is illustrated in Einstein's classic 'elevator' *gedanken* experiment. A ball thrown across an elevator that is free falling in a gravitational field is seen by an observer in the elevator to move at a constant velocity. The elevator and the ball have the same acceleration because of this equivalence between inertial and gravitational mass. In fact, for a sufficiently small enough region of space and time that we can neglect tidal forces, the reference frame resembles an *inertial frame of reference*, and therefore follows *special relativity.* We can clearly state the equivalence principle as:

> *The equivalence principle: An observer occupying a small region of space-time that is free-falling obeys the laws of physics of an inertial reference frame.*

The most important consequence of this is that a relativistic description of gravity must incorporate this principle. Subsequently, the main idea of general relativity is that massive objects cause the space-time to curve. In the local neighbourhood of an event P, the line element must have the geometry of Minkowski space-time. The space-time is then constructed on a pseudo-Riemannian [1] manifold for which the line element has the general form

$$ds^2 = g_{\mu\nu} dx^\mu dx^\nu, \tag{3.4}$$

where $g_{\mu\nu}$ is a metric tensor with Einstein sum indices μ, $\nu = 0, 1, 2, 3$. The Einstein notation is a convention used to imply summation over all the values of the index where the index variable appears twice and is not defined. The inherent problem with considering the space-time element to determine curvature of space-time is that a coordinate transformation is needed to reduce Eq. (3.4) to the Minkowski space-time. Therefore, we need to define the curvature of a manifold independent of the coordinate system used [2]. The curvature tensor is derived from the second covariant differentiation of the arbitrary vector field v_a defined on a manifold which

[1]Manifolds are objects which resemble the flat space for sufficiently small regions. A Riemannian manifold is locally Euclidean.

[2]More detailed definitions and mathematical background can be found in Taylor and Wheeler [2] and Hobson, Efstathiou & Lasenby [3].

is coordinate-independent. The Riemann rank-4 curvature tensor $R^{\rho}_{\sigma\mu\nu}$ is coordinate independent and has components

$$R^{\rho}_{\sigma\mu\nu} \equiv \partial_\mu \Gamma^{\rho}_{\nu\sigma} - \partial_\nu \Gamma^{\rho}_{\mu\sigma} + \Gamma^{\rho}_{\mu\lambda}\Gamma^{\lambda}_{\nu\sigma} - \Gamma^{\rho}_{\nu\lambda}\Gamma^{\lambda}_{\mu\sigma}, \tag{3.5}$$

where

$$\Gamma^{\alpha}_{\beta\mu} = \frac{1}{2} g^{\alpha\nu}(\partial_\beta g_{\nu\mu} + \partial_\mu g_{\beta\nu} - \partial_\nu g_{\beta\mu}), \tag{3.6}$$

are the *Christoffel* symbols which are not coordinate independent.

3.2.2 Einstein Equation

Einstein was motivated to define a coordinate independent equation which connects mass and energy as the source of space-time curvature. The gravitational field equations can be derived from the following results:

1. The field equation of Newtonian gravity is

$$\nabla^2 \Phi = 4\pi G \rho, \tag{3.7}$$

   where Φ is the gravitational potential, G is the gravitational constant and ρ is the matter density.

2. In the weak gravitational field limit, the 00- component of the metric must be $g_{00} = (1 + \frac{2\Phi}{c^2})$ (to recover Newtonian gravity).

3. A result from special relativity is that the energy-momentum tensor component is $T_{00} = \rho c^2$ in an inertial reference frame [3].

One can deduce that since

$$\nabla^2 g_{00} = \frac{8\pi G}{c^4} T_{00}, \tag{3.8}$$

it suggests that the gravitational field equations must be of the form

$$K_{\mu\nu} = \kappa T_{\mu\nu}, \tag{3.9}$$

where $K_{\mu\nu}$ is a rank-2 tensor describing the curvature of space-time, $\kappa = \frac{8\pi G}{c^4}$ and $T_{\mu\nu}$ is the energy-momentum tensor. Due to the Newtonian limit, $K_{\mu\nu}$ must have the properties that it should at most contain *linear* terms in the *second derivatives* of the metric tensor (see Eq. (3.8)). Secondly, since the energy-momentum tensor is symmetric, then $K_{\mu\nu}$ must also be symmetric. The curvature tensor $R_{\mu\nu\sigma\rho}$ is already linear in the second order derivatives of the metric [3]. Thus $K_{\mu\nu}$ must be of the form

$$K_{\mu\nu} = aR_{\mu\nu} + bRg_{\mu\nu} + \lambda g_{\mu\nu}, \tag{3.10}$$

where a, b, λ are constants. And $R_{\mu\nu}$ is the Ricci tensor and R is the scalar curvature. The Ricci tensor is obtained by contracting the Riemann rank-4 curvature tensor

$$R_{\mu\nu} = R^{\rho}_{\mu\rho\nu}, \tag{3.11}$$

and the scalar curvature for a given metric tensor is

$$R = g^{ab}R_{ab}. \tag{3.12}$$

We note that $\lambda = 0$ because $K_{\mu\nu}$ is linear in the second order derivatives of $g_{\mu\nu}$. However, we will see that relaxing this condition leads to including a *cosmological constant* for the expansion of the universe.

It follows from $\nabla_\mu T^{\mu\nu} = 0$, and from the results $\nabla_\mu(R^{\mu\nu} - \frac{1}{2}g^{\mu\nu}R)$ and $\nabla_\mu g^{\mu\nu} = 0$ that

$$\nabla_\mu K^{\mu\nu} = (\frac{1}{2}a + b)g^{\mu\nu}\nabla_\mu R = 0. \tag{3.13}$$

Thus $b = \frac{-a}{2}$. It follows from careful considerations of the weak-field limit of Newtonian gravity that $a = -1$ [3], and thus Einstein's gravitational field equations are

$$R_{\mu\nu} - \frac{1}{2}g_{\mu\nu}R = -\kappa T_{\mu\nu}, \tag{3.14}$$

or in terms of the contracted energy-momentum tensor

$$R_{\mu\nu} = -\kappa(T_{\mu\nu} - \frac{1}{2}Tg_{\mu\nu}). \tag{3.15}$$

Unlike Newtonian gravity, Einstein's field equations have the same number of equations as there are components in the metric tensor $g_{\mu\nu}$ of four-dimensional space-time. Therefore, general relativity is a complicated theory of gravity and generally difficult to solve.

3.3 Schwarzschild metric

An illustrative case is when the energy-momentum tensor $T_{\mu\nu} = 0$ which yields the vacuum Einstein solutions. In empty space, the Einstein equations have solutions that are non-trivial due to the non-linearity in $g_{\mu\nu}$. In Eq. (3.15), we have the gravitational field equation

$$R_{\mu\nu} - \frac{1}{2}Rg_{\mu\nu} = 0, \tag{3.16}$$

which can have non-zero components and implies that non-vanishing curvature is due to the presence of a gravitational field. The first exact solution of Einstein's equations was found by Karl Schwarzschild [12]. The Schwarzschild metric represents the metric outside of a static spherically symmetric massive object of mass M. It is given by [3]

$$ds^2 = -(1 - \frac{2M}{r})dt^2 + (1 - \frac{2M}{r})^{-1}dr^2 + r^2 d\theta^2 + r^2 \sin^2\theta d\phi^2, \tag{3.17}$$

where θ and ϕ are the azimuth and polar angles, respectively. From this point forward in this thesis, we will be using the natural units $G = 1$ and $c = 1$. We define the Schwarzschild radius $r_s = 2M$ which also represents the radius of the event horizon of a black hole of mass M. Eq. (3.17) describes the metric of a black hole with a coordinate singularity at $r = r_s$, and a physical singularity at $r = 0$ which characterizes the black hole. The coordinate singularity is removed by adopting Eddington-Finkelstein coordinates [3, 6]. However, for a spherically symmetric, massive object whose mass is distributed uniformly, the Schwarzschild metric is valid for its exterior where $r > r_s$.

3.3.1 Eddington-Finkelstein coordinates

For radially ingoing and outgoing light, it is convenient to use a set of coordinates that extend the region of Schwarzschild space-time beyond the event horizon. We obtain these coordinates by considering the solution for the null geodesic in the Schwarzschild metric

$$0 = -(1 - \frac{2M}{r})dt^2 + (1 - \frac{2M}{r})^{-1}dr^2. \tag{3.18}$$

Thus we have two solutions for ingoing and outgoing null geodesics

$$t = \pm \int dr(1 - \frac{2M}{r})^{-1} = \pm(r + 2M \log|\frac{r}{r_s} - 1|) + constant. \tag{3.19}$$

The quantities $v = t + (r + 2M \log|\frac{r}{r_s} - 1|)$ and $u = t - (r + 2M \log|\frac{r}{r_s} - 1|)$ are constant and null coordinates representing ingoing and outgoing photons, respectively. These coordinates are known as *tortoise* coordinates. It is common practice to define a *timelike* coordinate t' [3]. For the ingoing photons, this is the advanced Eddington-Finkelstein coordinate

$$t'_a = v - r, \tag{3.20}$$

and for the outgoing photons, this is the retarded Eddington-Finkelstein coordinate

$$t'_r = u + r. \tag{3.21}$$

Correspondingly, the Schwarzschild metric in these coordinates is obtained by replacing dt with $dv = dt + \frac{r}{r-2M}dr$ and $du = dt - \frac{r}{r-2M}dr$. Thus the metric in ingoing Eddington-Finkelstein coordinates is

$$ds^2 = -(1 - \frac{r_s}{r})dv^2 + 2dvdr + r^2(d\theta^2 + \sin^2\theta d\phi^2), \tag{3.22}$$

and the outgoing

$$ds^2 = -(1 - \frac{r_s}{r})du^2 + 2dudr - r^2(d\theta^2 + \sin^2\theta d\phi^2). \tag{3.23}$$

In both of these metrics, we can see that at the event horizon $r = r_s = 2M$ the metrics are non-singular. Unlike in the Schwarzschild metric, there are no diverging terms and the determinant of the metric is non-vanishing.

3.3.2 Local and far-away observers

As in special relativity, a time-like geodesic is measured by the local clock of an observer. In the Schwarzschild metric, for a local stationary observer ($d\theta$, $d\phi = 0$, $dr = 0$) we set $ds^2 = -d\tau^2$ and thus the proper time denoted by τ is

$$d\tau = \sqrt{(1 - \frac{2M}{r})}\, dt. \tag{3.24}$$

On the other hand, we define a *far-away observer* as an infinitely distant observer $r \to \infty$ who measures the coordinate time dt. By definition, this observer resides in a flat metric.

3.3.3 Gravitational redshift

An important consequence of the space-time curvature is that observers have clocks that tick at different rates. This is famously demonstrated by the gravitational redshift [3]. Let's consider an emitter at fixed position (r_E, θ_E, ϕ_E) sending a beam of light to a receiver at spatial position (r_R, θ_R, ϕ_R) (see Figure. 3.1). At time t_E as measured by a distant observer in coordinate time, the beam of light is emitted and at time t_R it is received. At time $t_E + \Delta t_E$, another beam of light is emitted and received at time $t_R + \Delta t_R$. Let's consider the null geodesic between t_R and t_E by setting $ds^2 = 0$ in Eq. (3.17)

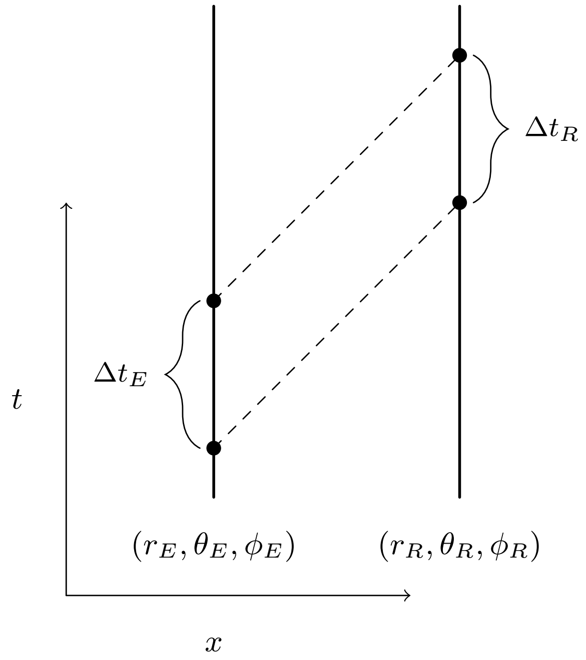

Figure 3.1: A space-time diagram of the gravitational redshift. An emitter located at (r_R, θ_R, ϕ_R) sends light (dashed line) to the receiver at (r_E, θ_E, ϕ_E). The emitter at time $t_E + \Delta t_E$ sends light again which is received at $t_R + \Delta t_R$.

$$\frac{dt}{d\sigma} = (1 - \frac{r_s}{r})^{-1/2}[-g_{ij}\frac{dx^i}{d\sigma}\frac{dx^j}{d\sigma}]^{1/2}, \tag{3.25}$$

where σ is an affine parameter for the null geodesic, and i, j are indices for spatial dimensions. For the Schwarzschild metric, the time difference between events $t_R - t_E$ along the null geodesic is the integral of Eq. (3.25). This only depends on the path through the space coordinates and thus the far-away observer would conclude that $\Delta t_E = \Delta t_R$ [3].

For the emitter, the local time on his clock between events t_E and $t_E + \Delta t_E$ is given by the proper time for this stationary observer which will be denoted τ. For a time-like event, $ds^2 = -c^2 d\tau^2$ and thus since the spatial position is fixed $dr = 0$, $d\phi = 0$ and $d\theta = 0$ then the proper time is

$$d\tau^2 = (1 - \frac{r_s}{r})dt^2. \tag{3.26}$$

The coordinate r is constant along the worldline, we integrate w.r.t. t

$$\Delta\tau_E = (1 - \frac{r_s}{r_E})^{1/2}\Delta t_E. \tag{3.27}$$

Similarly, the receiver measures the proper time

$$\Delta\tau_R = (1 - \frac{r_s}{r_R})^{1/2}\Delta t_R. \tag{3.28}$$

Since $\Delta t_R = \Delta t_E$, the ratio between proper times is

$$\frac{\Delta\tau_R}{\Delta\tau_E} = \frac{(1 - \frac{r_s}{r_R})^{1/2}}{(1 - \frac{r_s}{r_E})^{1/2}}. \tag{3.29}$$

This is known as the Schwarzschild time dilation. Furthermore, if we consider the frequency of the light ν, then their ratio is

$$\frac{\nu_R}{\nu_E} = \frac{(1 - \frac{r_s}{r_E})^{1/2}}{(1 - \frac{r_s}{r_R})^{1/2}}. \tag{3.30}$$

If the receiver is positioned above the emitter $r_R = r_E + h$ and $h << r_E$ then

$$\frac{\nu_R}{\nu_E} \approx 1 - \frac{r_s}{2r_E} + \frac{r_s}{2(r_E + h)} = 1 - \frac{r_s h}{2r_E(r_E + h)}, \tag{3.31}$$

implying that the frequency of the receiver is redshifted by the gravitational field. Therefore, the phenomenon called gravitational redshift is directly related to time dilation.

3.4 Far-away velocity light

Alternatively, we can observe the effect of the Schwarzschild time dilation by considering tangential null geodesics of light for observers in the gravitational potential. For example, at radial position $r = r_A$, light propagating horizontally has the null geodesic ($ds = d\phi = dr = 0$)

$$ds^2 = 0 = -(1 - \frac{2M}{r})dt^2 + r^2 d\theta^2 \tag{3.32}$$

If the distance travelled dx is much smaller than r then we can make the arclength $dx \approx r d\theta$. Thus the velocity of light as seen by a far-away observer is

$$c_A = \frac{dx}{dt} = \sqrt{1 - \frac{2M}{r_A}}\,. \tag{3.33}$$

We can assume that the distance the light travels as observed locally is L. Thus the time for light to travel as seen by a far-away observer is

$$t_A = \frac{L}{c_A} = \frac{L}{\sqrt{1 - \frac{2M}{r_A}}} \approx L(1 + \frac{M}{r_A}), \tag{3.34}$$

and similarly, for the same distance at radial position $r = r_B = r_A + h$ where h is the height, the time is

$$t_B = \frac{L}{c_B} = \frac{L}{\sqrt{1 - \frac{2M}{r_B}}} \approx L(1 + \frac{M}{r_B}). \tag{3.35}$$

Thus the time difference is

$$\Delta t = t_B - t_A = \frac{M}{r_B} - \frac{M}{r_A} \approx -\frac{r_s h}{2 r_A r_B}. \tag{3.36}$$

That is, the clock of the observer deeper in the gravitational well is slower than the one higher in the gravitational well as inferred by the far-away observer. We can set up a Mach-Zehnder interferometer to indirectly measure this time difference by measurement of the phase difference.

3.5 Kerr metric

It took almost 48 years after the formulation of the Einstein field equations to determine the metric around a rotating massive body [15]. Although the principles are similar, the lack of spherical symmetry due to the angular momentum made algebraic calculations difficult.

In general, the exterior metric that describes an axisymmetric rotating *massive star* or *planet* is given by the Hartle-Thorne metric, which includes the mass quadrupole moment q that depends on the structure of the massive body [16–19]. A massive planet or neutron star has the mass quadrupole moment $q = kj^2$ where k is a constant. The metric that describes the space-time around a rotating black hole is the Kerr metric [15]. The *Kerr metric* can be obtained from the Hartle-Thorne metric provided that one sets $q = -j^2$ where j is the mass normalized angular momentum of the massive object.

Compared to the original form of the Kerr metric as derived by Roy Kerr [15], the Kerr metric in the Boyer-Lindquist coordinates minimizes the number of off-diagonal components [20]. The Kerr metric in these coordinates describes the space-time around a rotating black hole. To first order in the mass normalized angular momentum $a = \frac{J}{M}$ (note that we will use a to denote the Kerr angular momentum in the rest of the thesis instead of j), the Hartle-Thorne metric and Kerr metric are equivalent. The Kerr line-element is

$$\begin{aligned} ds^2 = &-(1-\frac{2Mr}{r^2+a^2\cos^2\theta})dt^2 - \frac{4Mra\sin^2\theta}{r^2+a^2\cos^2\theta}dtd\phi \\ &+(\frac{r^2+a^2\cos^2\theta}{r^2-2Mr+a^2})dr^2 + (r^2+a^2\cos^2\theta)d\theta^2 \\ &+(r^2+a^2+\frac{2Mra^2\sin^2\theta}{r^2+a^2\cos^2\theta})\sin^2\theta d\phi^2, \end{aligned} \tag{3.37}$$

where $a = \frac{J}{M}$ is the Kerr parameter where J is the angular momentum of the massive black hole of mass M. For $M \to 0$, the line element reduces to the flat metric in oblate spheroidal coordinates [20]. These coordinates are given by $x = \sqrt{r^2+a^2}\ \sin\theta\cos\phi$, $y = \sqrt{r^2+a^2}\ \sin\theta\sin\phi$ and $z = r\cos\theta$.

We can similarly consider the null geodesic solution as we had done for the Schwarzschild metric in Section 3.4. The presence of the cross term $dtd\phi$ will lead to an anisotropy of the null geodesic. We will more closely consider the effect of this anisotropy in Chapter 6. Furthermore, an observer in the Kerr metric that is moving at zero angular momentum will see an isotropic speed of light $c = 1$ and in their coordinates, their metric will eliminate the cross term $dtd\phi$. In the next section, we will review the conserved quantities that will assist in determining the coordinates of these observers.

3.6 Killing vector

A conserved quantity implies that there is a symmetry along the geodesic [6]. Similarly, if the Lagrangian is not dependent on a coordinate x^i then the Lagrange equation implies a conserved quantity along a geodesic

$$\xi \cdot \vec{u} = g_{\mu\nu}\xi^\mu u^\nu = const, \tag{3.38}$$

where ξ is the *Killing vector* associated with the symmetry. u is the 4-velocity defined by

$$\vec{u} = (\frac{dx_0}{d\tau}, \frac{dx_1}{d\tau}, \frac{dx_2}{d\tau}, \frac{dx_3}{d\tau}). \tag{3.39}$$

A Killing vector implies that the metric is unchanged under a coordinate transformation. For example, the Killing vector components for the time translation $t + dt$ of the Schwarzschild metric are $\xi_t = 1$, $\xi_r = 0$, $\xi_\phi = 0$. Implying that there is a conserved quantity given by Eq. (3.38). The conserved quantity is the energy E

$$(1-\frac{2GM}{r})\frac{dt}{d\tau} = E. \tag{3.40}$$

Knowledge of the conserved quantity is essential for solving the orbital dynamics of a photon or a massive object. It is also useful for obtaining coordinate transformations into the frame of an inertial observer.

3.7 Quantum Field Theory (QFT) in curved space-time

The tremendous success of quantum theory prompts the question on whether it can be merged with special and general relativity. Klein and Gordon [21] had the initial idea of quantizing the classical field by replacing the classical quantitites of energy and momenta with their respective quantum operators in the energy-momentum relation. This led to the Klein-Gordon equation which describes the scalar field of spinless particles [22]. In quantum field theory, particles are interpreted as quanta of the quantum field. Thus far, quantum field theory had only been applied to quantum fields in flat space-time. An extension of QFT was further generalized to curved space-time [23]. In this case, QFT in curved space-time attempts to include the effect of strong gravity and large accelerations. In contrast to QFT in flat space-time, this theory predicted the non-uniqueness of the vacuum state [23]. In the Schwarzschild metric, this leads to particle creation by black holes known as Hawking radiation [24]. Similarly, the Unruh effect describes the observation of thermal particles by an accelerating observer [25]. The dynamical Casimir effect illustrates that particles are produced by a single moving mirror [26]. Besides the latter, these predictions of QFT in curved space-time have yet to be confirmed. However, Hawking radiation was recently observed in an optical analogue system [27]. The main limitation of QFT in curved space-time is that it does not quantize the gravitational field. Instead, quantum fields propagate on the classical curved space-time background and in this sense it is classified as a semi-classical theory of gravity. Nonetheless, there are ongoing efforts to fully quantize gravity ranging from string theory [28], loop quantum gravity [29], stochastic gravity [30] to spectral geometry [31]. Observational effects predicted by these theories would occur in the limit of highly curved space-time, or at extremely small scales (i.e. Planck scales).

With concern to the measurement of classical space-time parameters, QFT in curved space-time is expected to accurately describe the evolution of quantum states. In the rest of the thesis, we will be using this semi-classical framework. In the following section, we will consider the radial propagation of a photon wavepacket in the Schwarzcshild metric. This is essential for the evolution of quantum states in curved space-time and for obtaining quantum limits on the precision of r_s in gravitational red-shift measurements.

3.7.1 Wavepacket propagation in curved space-time

For realistic devices operating on optical inputs, we cannot treat light as a single mode in frequency. In quantum optics, we treat light as pulses modelled by wavepackets of multiple modes. In quantum field theory, we quantize the scalar field such that it obeys the Klein-Gordon equation

$$\Box\phi + m^2\phi = 0, \tag{3.41}$$

where $\Box$ is the d'Alambertian defined in curved space-time as $\Box = \frac{1}{\sqrt{-g}}\partial_\mu\sqrt{-g}\,\partial^\mu$ and where $g = det(g_{\mu\nu})$. m is the mass of the scalar field. The full quantization procedure can be found in N. D. Birrell and P. C . W. Davies [14]. Light in (1+1) space-time can be treated as a scalar massless ($m = 0$) scalar field $\Phi(x, t)$, the field obeys the massless Klein-Gordon equation

$$\Box\Phi = 0. \tag{3.42}$$

We consider the Schwarzschild metric in Eq. (3.17) and use the tortoise coordinates to make the Klein-Gordon equation look locally flat everywhere. Since we are concerned only with radial light propagation, we can assume a $1 + 1$ dimensional space-time that is flat and the quantum field satisfies the Klein-Gordon equation [13, 14]. Thus Eq. (3.42) takes the form

$$\partial_\mu\partial_\nu\Phi(u, v) = 0, \tag{3.43}$$

where $u = t - (r + r_s \log|\frac{r_s}{r} - 1|)$ and $v = t + (r + r_s \log|\frac{r_s}{r} - 1|)$ are the Eddington-Finkelstein advanced and retarded coordinates. Thus, we respectively have the solutions for the outgoing and ingoing waves

$$\begin{aligned}\phi^u_\omega(u) &= \frac{e^{i\omega u}}{2\sqrt{\pi\omega}},\\ \phi^v_\omega(v) &= \frac{e^{i\omega v}}{2\sqrt{\pi\omega}}.\end{aligned} \tag{3.44}$$

The solutions for the plane waves ϕ_ω^u and ϕ_ω^v are constant along null geodesics. We note that ω is the frequency as observed by an observer at infinity. The mode solutions are normalized to the inner product over the entire frequency space

$$(\phi_\omega^u(u), \phi_{\omega'}^u(u)) = (\phi_\omega^v(v), \phi_{\omega'}^v(v)) = \delta(\omega - \omega'). \tag{3.45}$$

If the space-time admits asymptotically a time-like Killing vector field then the field can be quantized. Thus the solution of the Klein-Gordon equation (Eq. (3.42)) is a set of linearly independent modes. The full solution of the quantum field is expanded in the two modes (and their negative frequency Hermitian conjugate)

$$\Phi = \int_0^{+\infty} d\omega[\phi_\omega^u a_\omega + \phi_\omega^v b_\omega + h.c.], \tag{3.46}$$

where a_ω and b_ω are the annihilation operators of the outgoing/ ingoing modes respectively which satisfy the usual commutation relation

$$[a_\omega, a_{\omega'}^\dagger] = [b_\omega, b_{\omega'}^\dagger] = \delta(\omega - \omega'). \tag{3.47}$$

A pulse around the central frequency $\Omega_{K,0}$ is described by a wavepacket with distribution $F(\Omega_K)$. The localized annihilation operator is therefore given by

$$a_{\Omega_0}(\tau_K) = \int_0^{+\infty} d\Omega_K e^{-i\Omega_K u_K} F_{\Omega_{K,0}}(\Omega_K) a_{\Omega_K}, \tag{3.48}$$

where u_K is the locally measured outgoing tortoise coordinate $u_K = \tau_K - (r_K + r_s \log|\frac{r_s}{r_K} - 1|)$ for the radial positions $K = A, B$. Thus we can transform Ω_A to Ω_B using the gravitational red-shift relation and measure how the frequency distribution $F_{\Omega_{A,0}}(\Omega_A)$ is distorted at radial position B. Optimal measurement of this distortion using continuous variable Gaussian states will be discussed in Chapter 4.

Bibliography

[1] *Fundamental quantum optics experiments conceivable with satellites reaching relativistic distances and velocities*, D. Rideout et al., Classical Quantum Gravity **29**, 224011 (2012).

[2] *Exploring Black Holes: Introduction to General Relativity*, E. F. Taylor, J. A Wheeler, Addison Wesley Longman (2000).

[3] *General Relativity: An Introduction for Physicists*, M. P. Hobson, G. Efstathiou, A. N. Lasenby, Cambridge University Press (2006).

[4] *Gravitation*, C. W. Misner, K. S. Thorne, and J. A. Wheeler, W. H. Freeman (1973).

[5] *General Relativity*, R. M. Wald, University of Chicago Press (1984).

[6] *Gravity: An Introduction to Einstein's General Relativity*, J. B. Hartle, Addison Wesley (2003).

[7] *Quantum Gravity*, C Rovelli, Cambridge University Press, Cambridge (2004).

[8] *Spacetime effects on satellite-based quantum communications*, D. E. Bruschi, T. C. Ralph, I. Fuentes, T. Jennewein, M. Razavi, Phys. Rev. D **90**, 045041 (2014).

[9] *Quantum metrology for relativistic quantum fields*, M. Ahmadi, D. E. Bruschi, and I. Fuentes, Phys. Rev. D **89**, 065028 (2014).

[10] *Quantum Estimation of Parameters of Classical Spacetimes*, T. G. Downes, J. R. van Meter, E. Knill, G. J. Milburn, C. M. Caves, Phys. Rev. D. **96** 105004 (2016).

[11] *Heisenberg scaling in Gaussian quantum metrology*, N. Friis, M. Skotiniotis, I. Fuentes, and W. Dr, Phys. Rev. A **92**, 022106 (2015).

[12] Schwarzschild, K. (1916). *:Uber das Gravitationsfeld eines Massenpunktes nach der Einsteinschen Theorie.*

[13] *Quantum Field Theory*, M. Srednicki, Cambridge University Press (2007).

[14] *Quantum Fields in Curved Space*, N. D. Birrell and P. C . W. Davies, Cambridge Monographs on Mathematical Physics, Cambridge University Press (1982).

[15] *Gravitational Field of a Spinning Mass as an Example of Algebraically Special Metrics*, R. P. Kerr, Phys. Rev. Lett. **11**, 237 (1963).

[16] *Approximate Metric for a Rotating Deformed Mass*, F. Frutos-Alfaro, P. Montero-Camacho, M. Araya-Arguedas, J. Bonatti-Gonzalez, International Journal of Astronomy and Astrophysics, **5**(1):1-10, 2015.

[17] *Approximate Kerr-like Metric with Quadrupole*, F. Frutos- Alfaro, International Journal of Astronomy and Astrophysics **6**, 334-345 (2016).

[18] *Circular geodesics in the Hartle-Thorne metric*, M.A. Abramowicz, G.J.E. Almergren, W. Kluzniak, A.V. Thampan, arXiv:gr-qc/0312070 (2003).

[19] *Equatorial Circular Geodesics in the Hartle-Thorne Spacetime*, D. Bini, K. Boshkayev, R. Ruffini, I. Siutsou, Il Nuovo Cimento vol. **36** C, N. 1 Suppl. 1, 2013.

[20] *The Kerr spacetime: a brief introduction*, D.L. Wiltshire, M. Visser and S.M. Scott eds., Cambridge University Press, Cambridge, U.K. (2009).

[21] *Quantentheorie und funfdimensionale relativitatstheorie*, O. Klein, Zeitschrift fur Physik, **37** (12):895906, (1926).

[22] *Gaussian quantum metrology and space-time probes*, D. Safranek, PhD Thesis, arXiv preprint: arXiv:1610.03538 (2016).

[23] *Quantum Field Theory in Curved Spacetime*, L. H. Ford, arXiv:gr-qc/9707062 (1997).

[24] *Black hole explosions?* , S. W. Hawking. Nature, **248**: 3031 (1974).

[25] *Notes on black-hole evaporation*, W. G. Unruh. Phys. Rev. D, **14**:870892 (1976).

[26] *Observation of the dynamical Casimir effect in a superconducting circuit.*, C. M. Wilson, G. Johansson, A. Pourkabirian, M. Simoen, J. R. Johansson, T. Duty, F. Nori, and P. Delsing, Nature, **479**(7373):376379 (2011).

[27] *Observation of Stimulated Hawking Radiation in an Optical Analogue*, J. Drori, Y. Rosenberg, D. Bermudez, Y. Silberberg, U. Leonhardt, Phys. Rev. Lett. **122**, 010404 (2019).

[28] *String theory and gravity*, T. Damour, A.M. Polyakov, Gen.Rel.Grav. **26** 1171-1176 (1994) .

[29] *Loop Quantum Gravity*, D. Chiou, Int. J. Mod. Phys. D, Vol. **24**, No. 1, 1530005 (2015).

[30] *Stochastic Gravity: Theory and Applications*, B.L. Hu, E. Verdaguer, Living Rev. Relativity, **11** (2008).

[31] *On Information Theory, Spectral Geometry and Quantum Gravity*, A. Kempf, R. Martin, Phys.Rev.Lett.**100**:021304 (2008).

The following publication has been incorporated and modified as Chapter 4.

[1] **S. P. Kish**, T. C. Ralph, *Estimating space-time parameters with a quantum probe in a lossy environment*, Phys. Rev. D 93, 105013 (2016).

S. P. Kish has a 75% weighting and T. C. Ralph a 25% weighting of contribution to the paper *Estimating space-time parameters with a quantum probe in a lossy environment*. We equally did the results analysis and interpretation. I did most of the theoretical derivations and numerical calculations. I have done the majority of writing and preparation of figures. My supervisor Timothy C. Ralph had the initial idea, guided the project in the right direction, wrote half the introduction and contributed to the proofreading.

Chapter 4

Estimating space-time parameters with a quantum probe in a lossy environment

The aim in this thesis is to provide fundamental limits of unprecedented high precision measurements in the overlap of quantum physics and general relativity. In the following chapter, we consider wavepackets propagating through the space-time of Earth, and answer questions regarding the practicality of such an experiment. We provide practical tools for Earth to satellite based quantum experiments using Gaussian states.

We study the problem of estimating the Schwarzschild radius of a massive body using Gaussian quantum probe states. Previous calculations assumed that the probe state remained pure after propagating a large distance. In a realistic scenario, there would be inevitable losses. Here we introduce a practical approach to calculate the quantum Fisher Informations (QFIs) for a quantum probe that has passed through a lossy channel. Whilst for many situations loss means coherent states are optimal, we identify certain situations for which squeezed states have an advantage. We also study the effect of the frequency profile of the wavepacket propagating from Alice to Bob. There exists an optimal operating point for a chosen mode profile. In particular, employing a smooth rectangular frequency profile significantly improves the error bound on the Schwarzschild radius compared to a Gaussian frequency profile.

4.1 Introduction

The precision with which physical parameters can be estimated is limited by the level of fluctuations or noise in the measurement device. Irreducible levels of noise are fundamentally set by quantum mechanics onto measurement results, and hence quantum mechanics places limits on the ultimate precision of parameter estimation. The study of these limits and the development of protocols for reaching them is called quantum metrology [2]. In optics, the use of semi-classical probe states such as coherent states, where the quantum noise can be interpreted as photon shot-noise, leads to the standard quantum limit (SQL). Surpassing this limit can be done by using non-classical states displaying squeezing or entanglement [3].

Most work in quantum metrology assumes non-relativistic quantum mechanics. However, many applications of quantum metrology relate to relativistic phenomena such as gravitational waves [4] and the estimation of gravitational fields and accelerations [5]. More rigorous approaches to such problems, that will become important as precision grows, use relativistic quantum field theory to describe the quantum interactions in spacetime [6]. A number of authors have begun exploring such approaches [7–9].

Recently Bruschi et al. [10] showed that techniques for optimally estimating the transmission parameter of a quantum channel [11] can be adapted to the relativistic problem of estimating the Schwarzschild radius of a massive body. Their protocol involves coherently comparing a quantum optical probe state prepared at one height in the metric with a second, locally identical probe state, prepared at a different height. They investigated the use of optical probes prepared in coherent states and squeezed states and found that using squeezed vacuum states was optimal. However, the calculations of Ref. [10] assumed that losses could be neglected, even though the probe states potentially needed to be propagated over large distances in the protocol. In addition, only Gaussian temporal wave-packets were considered and a limited region of the parameter space was explored.

In this chapter we analyse a more realistic version of the Bruschi et al. protocol that includes the inevitable losses that would occur in such a scheme in practice and optimises the parameters with respect to height, bandwidth, mode-shape and operating point. We find that squeezing is not always optimal but can enhance precision under certain conditions. In our analysis we introduce a different approach to obtaining the Fisher information for this protocol which turns out to be much easier to generalize to more realistic scenarios.

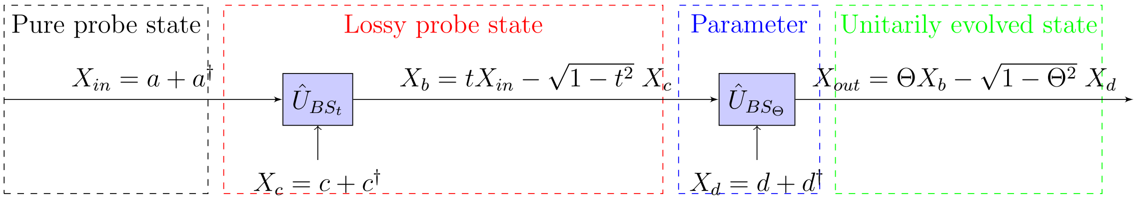

Figure 4.1: Representation of a quantum channel. A pure Gaussian probe state passes through a lossy channel of transmission t. It is equivalent to the probe state evolving under the unitary beamsplitter operator U_{BS_t}. The subsequent 'lossy probe state' will be used to measure the beamsplitter parameter Θ of the unitary operator U_{BS_Θ}.

The chapter is structured in the following way. In the next section we review the basic principles of estimating the transmission parameters of a quantum channel using a quantum probe, describing our approach to obtaining the relevant quantum Fisher informations and calculating results for mixed probe states. We use the framework of quantum metrology from Chapter 2. In Sec. 4.2 we review how this approach can be adapted to estimating parameters associated with space-time curvature, in particular the Schwarzschild radius, r_s, of a massive body. In Sec. 4.3 we apply our formalism to this problem and derive expressions for the relative errors in estimating r_s in a number of idealised scenarios. We make more realistic assumptions in Sec. 4.6, for example incorporating loss as a function of transmission distance and considering bright coherent beams with added squeezing. We conclude and discuss in Sec. 4.7.

4.2 Transmission of a quantum channel

The goal of any quantum estimation is to determine a probe state and probability operator-value measure (POVM) containing information about the estimator $\hat{\Theta}$ and to determine the value of Θ from the set of N measured outcomes [11]. We consider an unbiased estimator such that for $N \to \infty$, the expectation value $E[\hat{\Theta}]$ returns Θ and all errors disappear. The bound for the variance of an unbiased estimator is set by the Cramér-Rao inequality [16].

$$\langle \Delta\hat{\Theta}^2 \rangle \geq \frac{1}{F(\Theta)} \tag{4.1}$$

Where $F(\Theta)$ is the Fisher information of a measurement. The Fisher information coincides with the second moment of the classical logarithmic derivative of the likelihood function. For N measurements of identically prepared quantum states, the total Fisher information is the sum of all individual Fisher informations. This is a result of the central limit theorem, which applies to the variance of the mean value of N independent and identically distributed samples. Therefore, this implies that the variance of the mean of a parameter scales as $\frac{1}{NF(\Theta)}$. The Fisher information $F(\Theta)$ is further bounded by the *quantum Fisher information* $H(\Theta)$ which signifies the most precise measurement allowed by quantum mechanics. Similarly, the QFI is additive and for N measurements we have the bound

$$\langle \Delta\hat{\Theta}^2 \rangle \geq \frac{1}{NF(\Theta)} \geq \frac{1}{NH(\Theta)}. \tag{4.2}$$

The general problem we wish to address in this section is to determine the Cramér-Rao bound for the beamsplitter parameter Θ if the probe states initially evolve under a lossy quantum channel given by a known transmission coefficient t. We represent the situation diagrammatically in Fig. 4.1. It is always possible to decompose the lossy channels into orthogonal modes. We begin by introducing an auxiliary mode and treating the loss and parameter estimator as two beamsplitters with transmissions t and Θ.

We consider the beamsplitter transformations,

$$\hat{b}^\dagger = t\hat{a}_{in}^\dagger - \sqrt{1-t^2}\,\hat{c}^\dagger, \tag{4.3}$$
$$\hat{a}_{out}^\dagger = \Theta\hat{b}^\dagger - \sqrt{1-\Theta^2}\,\hat{d}^\dagger. \tag{4.4}$$

Where $\hat{a}_{in}$ is the annihilation operator corresponding to Alice's input mode and $\hat{b}$ is annihilation operator corresponding to the mode Bob receives. The auxiliary modes are $\hat{c}_{out}$ and $\hat{d}_{out}$. Our goal is to determine an appropriate *probe state* for $\hat{a}_{in}$ that maximises the QFI under the evolution of the *lossy quantum channel*. The QFI can be written in terms of the symmetric logarithmic derivative (SLD) $\hat{\Lambda}(\Theta)$ defined as a Hermitian operator that has the form [11]

$$\frac{d\hat{\rho}_\Theta}{d\Theta} = \frac{1}{2}[\hat{\rho}_\Theta\hat{\Lambda}(\Theta) + \hat{\Lambda}(\Theta)\hat{\rho}_\Theta], \tag{4.5}$$

where $\hat{\Lambda}(\Theta)$ is an optimal system observable with an expectation value $Tr[\hat{\Lambda}(\Theta)\hat{\rho}_\Theta] = 0$, and ρ_Θ is the density operator describing the output state of the probe. In order to determine the QFI, we can evaluate the operator $\Lambda(\Theta)$ and thus $H(\Theta) = Tr[\hat{\Lambda}^2(\Theta)\hat{\rho}_\Theta]$ as done in Ref [11].

However, we consider a more practical and succinct approach to determine the QFI that is useful if the additional known loss parameter t is introduced and the probe state is Gaussian. We assume that t is completely characterised beforehand. The representation of this lossy quantum channel in Fig. 4.1 consists of a two beamsplitter setup with t and Θ corresponding to the transmissions. A *pure Gaussian probe state* passes through a lossy channel of transmission t represented by the probe state evolving under the unitary beamsplitter operator U_{BS_t}. The subsequent 'lossy probe state' will be used to measure the beamsplitter parameter Θ of the unitary operator U_{BS_Θ}. To determine the QFI, we begin from the properties of two density matrices. The Bures distance is the minimal distance between purifications of two density matrices ρ and σ [12]

$$d_B(\rho,\sigma) = [2(1-\sqrt{\mathcal{F}(\rho,\sigma)}\,]^{\frac{1}{2}}, \tag{4.6}$$

where $\mathcal{F}(\rho,\sigma)$ is the quantum fidelity

$$\mathcal{F} = (Tr(\sqrt{\sqrt{\rho}\,\sigma\sqrt{\rho}}\,))^2. \tag{4.7}$$

The quantum fidelity or Uhlmann's transition probability is a well known quantification [13] for the similarity of quantum states. The Bures distance can be related to the quantum Fisher information via

$$H(\Theta) = \lim_{d\Theta\to 0} \frac{8(1-\sqrt{\mathcal{F}(\rho_\Theta,\rho_{\Theta+d\Theta})}\,)}{d\Theta^2}. \tag{4.8}$$

For pure states, the fidelity reduces to the transimission probability between the initial probe state and the final evolved state $\mathcal{F} = |\langle\psi|\psi'\rangle|^2$. For a general Gaussian state of any mixedness, the fidelity can be expressed in terms of the quadrature variances $V^+ = \langle\Delta X(\phi)^2\rangle$ and $V^- = \langle\Delta P(\phi)^2\rangle$, where $X = a + a^\dagger$ and $P = -i(a - a^\dagger)$. The variances $V^\pm$ are directly measurable values. We wish to determine the final quadrature variances of the evolved state $V_1^\pm$ for a parameter value Θ, and the variance $V_2^\pm$ for an infinitesimal change $\Theta + d\Theta$. The fidelity can be expressed in the form [13–15]

$$\mathcal{F} = \mathcal{F}(\phi_s)\mathcal{D}(x), \tag{4.9}$$

where ϕ_s is the angle between the two states and x is the complex coherent amplitude. We assume that for the rest of this chapter that this is unchanged $\phi_s = 0$. $\mathcal{F}$ at $\phi_s = 0$ can be expressed in terms of the quadrature variances V_1 and V_2

$$\mathcal{F}(\phi_s=0) = 2\{\sqrt{(V_1^+V_2^- + 1)(V_1^-V_2^+ + 1)} - \sqrt{(V_1^+V_1^- - 1)(V_2^+V_2^- - 1)}\,\}^{-1}. \tag{4.10}$$

In addition, if the two states are separated by $x_r + ix_i$ in phase space, a factor $\mathcal{D}(x)$ is introduced

$$\mathcal{D}(x) = \exp[-\frac{2x_r^2}{V_1^+ + V_2^+} - \frac{2x_i^2}{V_1^- + V_2^-}], \tag{4.11}$$

where x_r and x_i are the real and imaginary parts of the coherent amplitude, respectively.

4.2.1 Coherent probe state with thermal noise

We can use these expressions to determine the QFI for a *coherent probe state* with a *mixed thermal state* in the auxiliary mode $\hat{c}$. The variances of the quadratures are obtained from the Heisenberg picture. The variances add as follows $\langle(\Delta X_{out})^2\rangle = t^2\langle(\Delta X_{in})^2\rangle + (1-t^2)\langle(\Delta X_c)^2\rangle$ and $\langle(\Delta X_b)^2\rangle = \Theta^2\langle(\Delta X_{out})^2\rangle + (1-\Theta^2)\langle(\Delta X_d)^2\rangle$. A thermal state has variance $\langle(\Delta X_c)^2\rangle = 2\tilde{n}_{\mathrm{Th}} + 1$ and $\langle(\Delta X_d)^2\rangle = 1$ is the vacuum state. Hence

$$V_1^+ = 2\tilde{n}_{\mathrm{Th}}\Theta^2(1-t^2) + 1, \tag{4.12}$$

where $\tilde{n}_{\mathrm{Th}} = \frac{1}{e^{\frac{\hbar\omega}{k_B T}}-1}$ is the average number of photons in a single mode of frequency ω and temperature T. Thus for a slight variation in the parameter $\Theta + d\Theta$, the variance is

$$V_2^+ = V_1^+ + 4\tilde{n}_{\mathrm{Th}}\Theta d\Theta(1-t^2) + 2\tilde{n}_{\mathrm{Th}}d\Theta^2(1-t^2). \tag{4.13}$$

It can be shown that $V_1^- = V_1^+ = V_1$ and $V_2^- = V_2^+ = V_2$. Thus the equation for the fidelity 4.9 is reduced to

$$\mathcal{F}(\phi_s = 0) = 2\{(V_1V_2 + 1) - \sqrt{(V_1^2-1)(V_2^2-1)}\,\}^{-1}. \tag{4.14}$$

Thus the total fidelity to second order in $d\Theta$ is

$$\begin{aligned}\mathcal{F} &= 1 - \frac{d\Theta^2|t\alpha|^2}{V_1} - 4\frac{d\Theta^2\tilde{n}_{\mathrm{Th}}^2\Theta^2(1-t^2)^2}{(V_1^2-1)} \\ &= 1 - \frac{d\Theta^2|t\alpha|^2}{2\tilde{n}_{\mathrm{Th}}\Theta^2(1-t^2)+1} - \frac{d\Theta^2\tilde{n}_{\mathrm{Th}}(1-t^2)}{\tilde{n}_{\mathrm{Th}}\Theta^2(1-t^2)+1}.\end{aligned} \tag{4.15}$$

We make use of the definition in Eq. (4.8) and the binomial expansion for $x << 1$, $\sqrt{1-x} \approx 1 - x/2$. Finally, the QFI is given by

$$\begin{aligned} H(\Theta) &= \frac{4|t\alpha|^2}{V_1} + \frac{16\tilde{n}_{\mathrm{Th}}^2\Theta^2(1-t^2)^2}{(V_1^2-1)} \\ &= \frac{4|t\alpha|^2}{2\tilde{n}_{\mathrm{Th}}\Theta^2(1-t^2)+1} + \frac{4\tilde{n}_{\mathrm{Th}}(1-t^2)}{\tilde{n}_{\mathrm{Th}}\Theta^2(1-t^2)+1}. \end{aligned} \tag{4.16}$$

We note that for room temperature $T = 300$ K and signal frequency $\omega = 700$ THz ($\lambda = 430$ nm), the thermal number occupation $\tilde{n}_{Th}$ is negligible. Thus, the QFI can be approximated to that of an attenuated coherent state

$$H(\Theta) = 4|t\alpha|^2. \tag{4.17}$$

Therefore, for this signal frequency at room temperature, the effect is negligible. However, for lower frequencies $\omega < \frac{k_B T}{\hbar}$ the average number of photons increases and thus the channel loss is much greater.

4.2.2 Squeezed Coherent probe state

We now consider a *squeezed coherent probe state.* We assume the auxiliary vacuum states in either beamsplitters have variance $\Delta X_c = \Delta X_d = 1$. A squeezed coherent state can have a quadrature variance that is better than the shot noise $\langle(\Delta X_{in})^2\rangle = e^{-2r}$ and $\langle(\Delta P_{in})^2\rangle = e^{2r}$. The level of squeezing is determined by the parameter r where we have assumed the maximum squeezing without loss of generality is in the X quadrature. We note that the squeezing parameter r, the magnitude $|\alpha|$ and the angle θ of the coherent state are the only relevant parameters Thus, the variances of the evolved state are $V_1^+ = \Theta^2 t^2(e^{-2r}-1)+1$ and $V_1^- = \Theta^2 t^2(e^{2r}-1)+1$. Since we are estimating how well a change in Θ can be detected, the second state is the same state with an infinitesimal shift in the parameter $\Theta + d\Theta$. In phase space, the separation is given by $x_r + ix_i = d\Theta t(\cos(\theta) + i\sin(\theta))|\alpha|$. We approximate the fidelity expression to second order in $d\Theta$ and disregarded any higher orders.

The fidelity for the squeezed coherent state is

$$\begin{aligned} \mathcal{F} =& 1 - \frac{t^2(2(\Theta t)^4 - 2(\Theta t)^2 + 1)}{(1-t^2\Theta^2)(2\Theta^2 t^2(1-t^2\Theta^2) + (\sinh^{-2}(r)))} d\Theta^2 \\ &- |\alpha_0 t|^2 (\frac{\cos^2(\theta)}{V_1^+} + \frac{\sin^2(\theta)}{V_1^-}) d\Theta^2. \end{aligned} \tag{4.18}$$

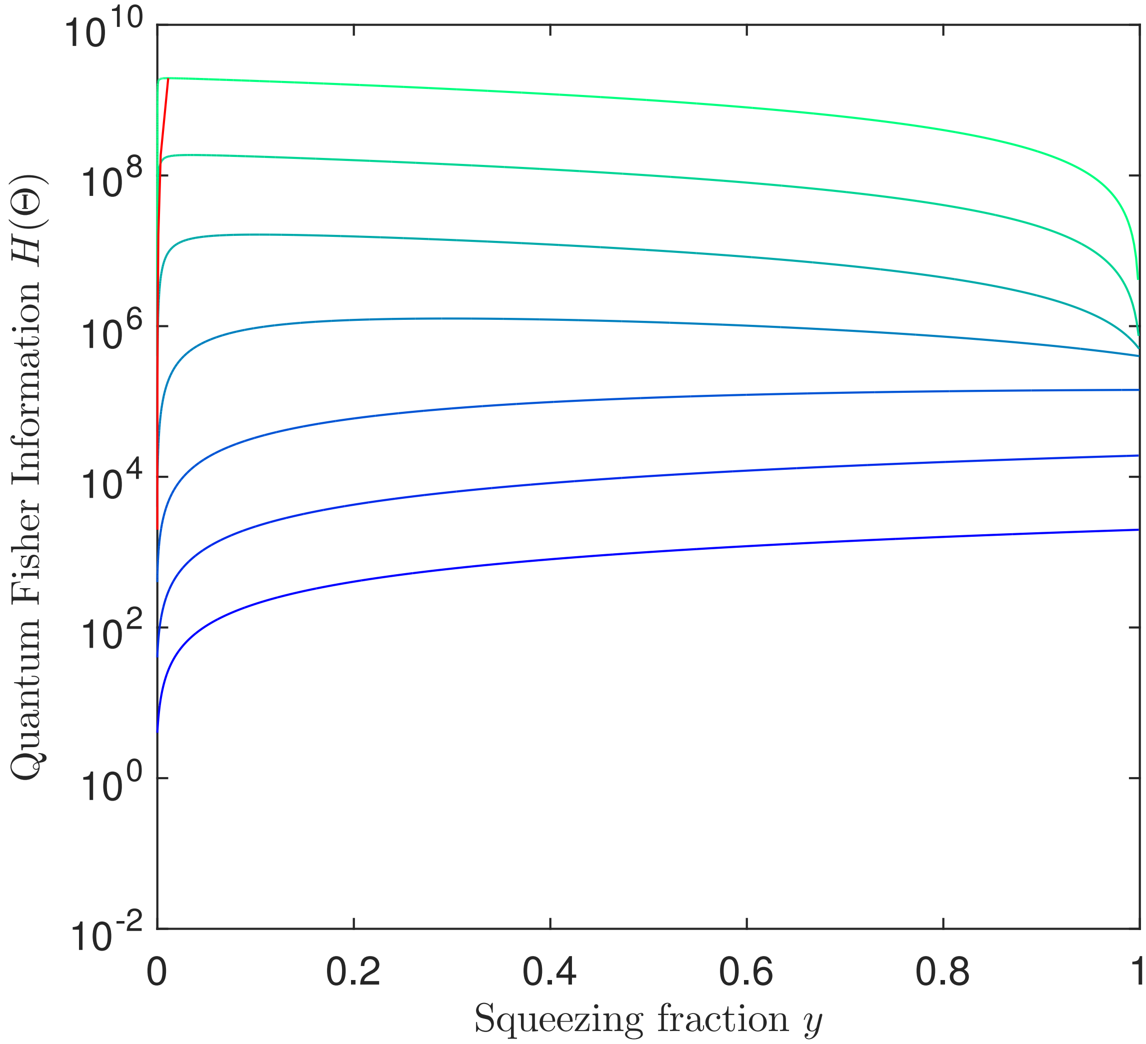

Figure 4.2: The QFI for perfect transmission $t = 1$ for various probe energies $\tilde{n} = 10, 10^2, 10^3, 10^4, 10^5, 10^6, 10^7$ (blue to green). For $\tilde{n} \geq 10^4$, it is no longer advantageous to use a large fraction of squeezed photons. The parameter to be measured is chosen to be $\Theta = 1 - 1.0 \times 10^{-3}$. The red line is the maximum QFI for each probe energy.

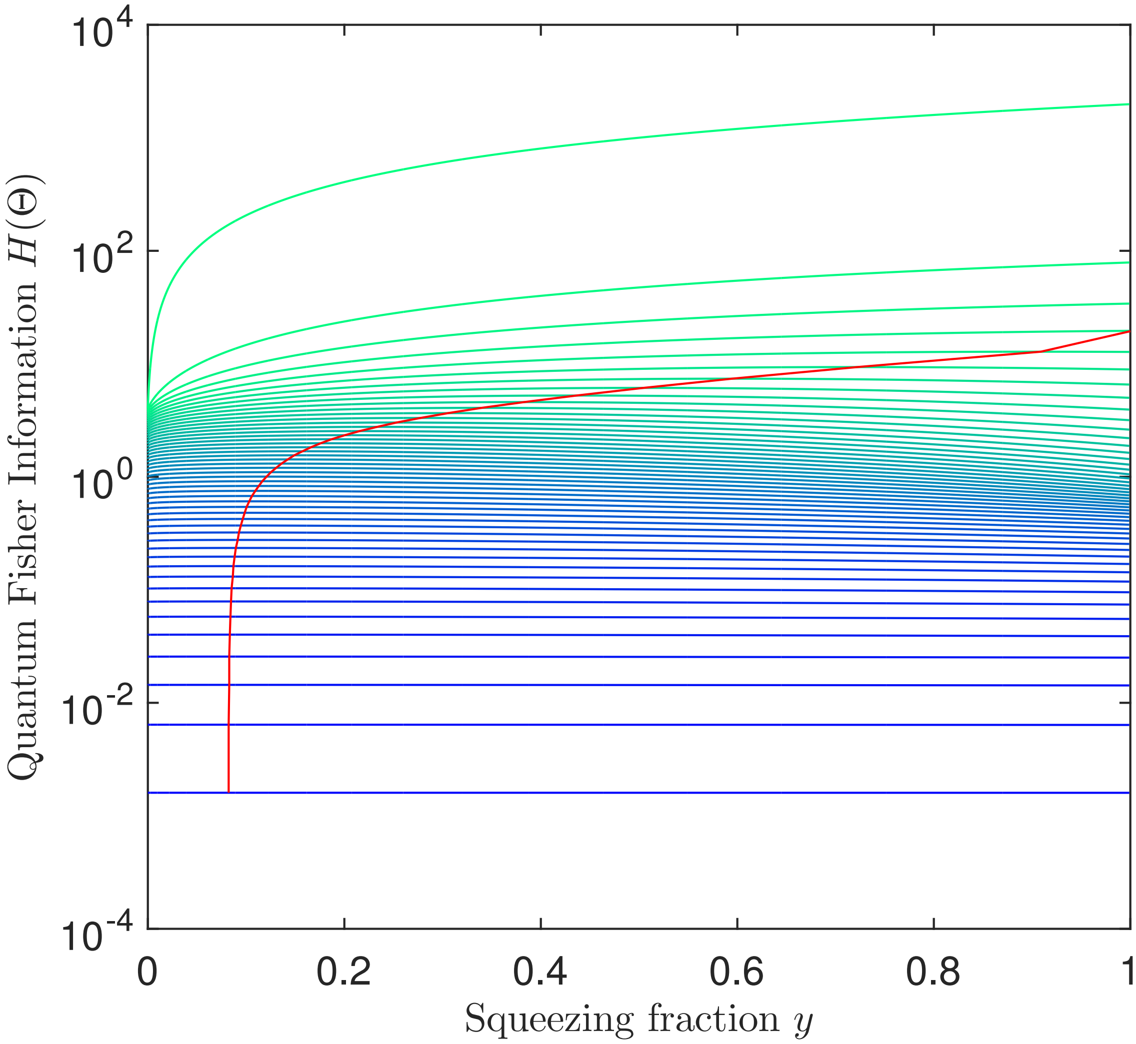

Figure 4.3: The quantum Fisher Information for a squeezed coherent state with probe state energy $\tilde{n} = 1$. The channel transmission t varies from $t = 0$ (blue) to $t = 1.00$ (green) in 0.02 intervals. The red curve represents the maximum QFI for each t. The parameter is $\Theta = 1 - x \approx 1 - 1.0 \times 10^{-3}$. The red line is the maximum QFI.

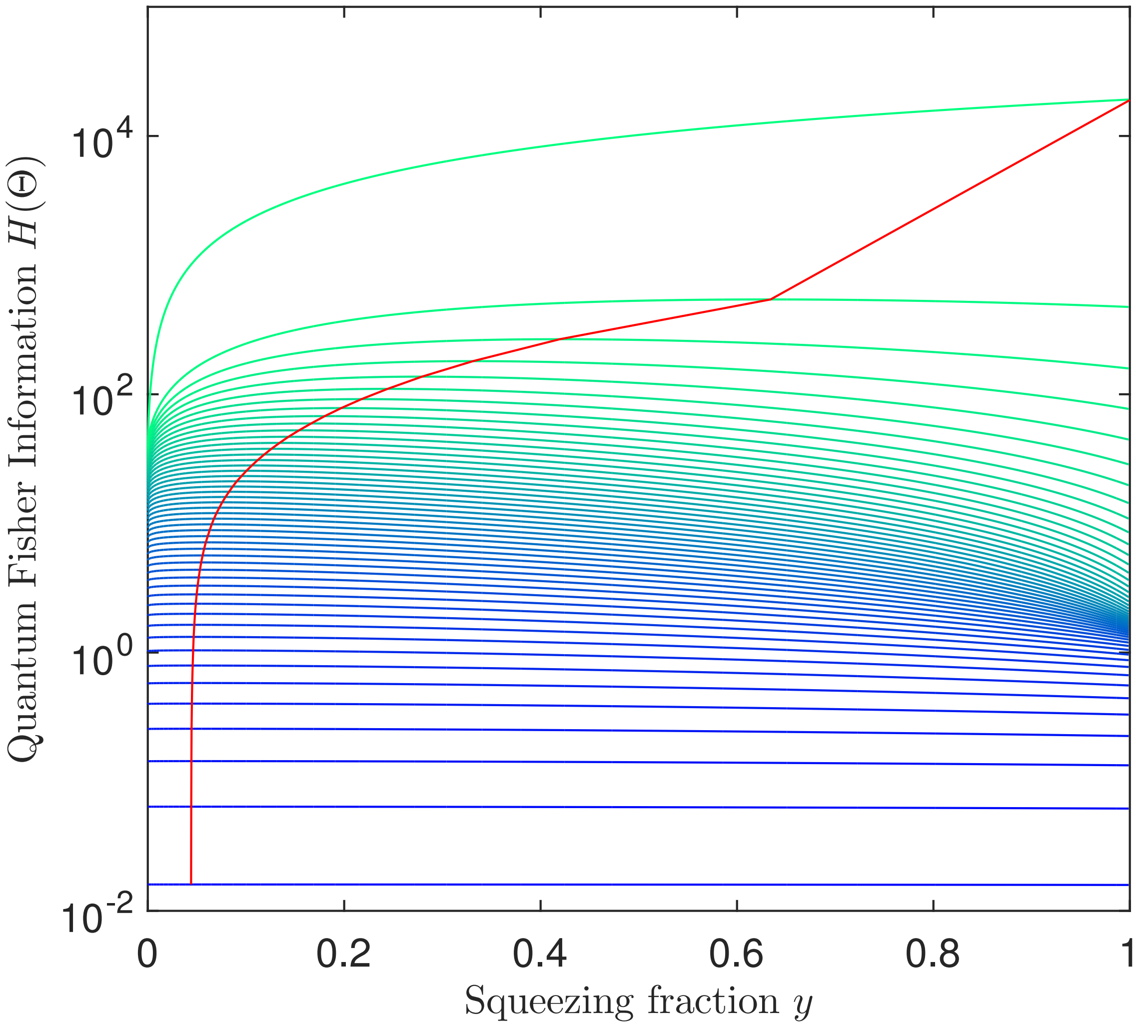

Figure 4.4: The QFI for a squeezed coherent state with probe state energy $\tilde{n} = 10$. The channel transmission t varies from $t = 0$ (blue) to $t = 1.00$ (green) in 0.02 intervals. Same Θ as in Fig. 4.3.

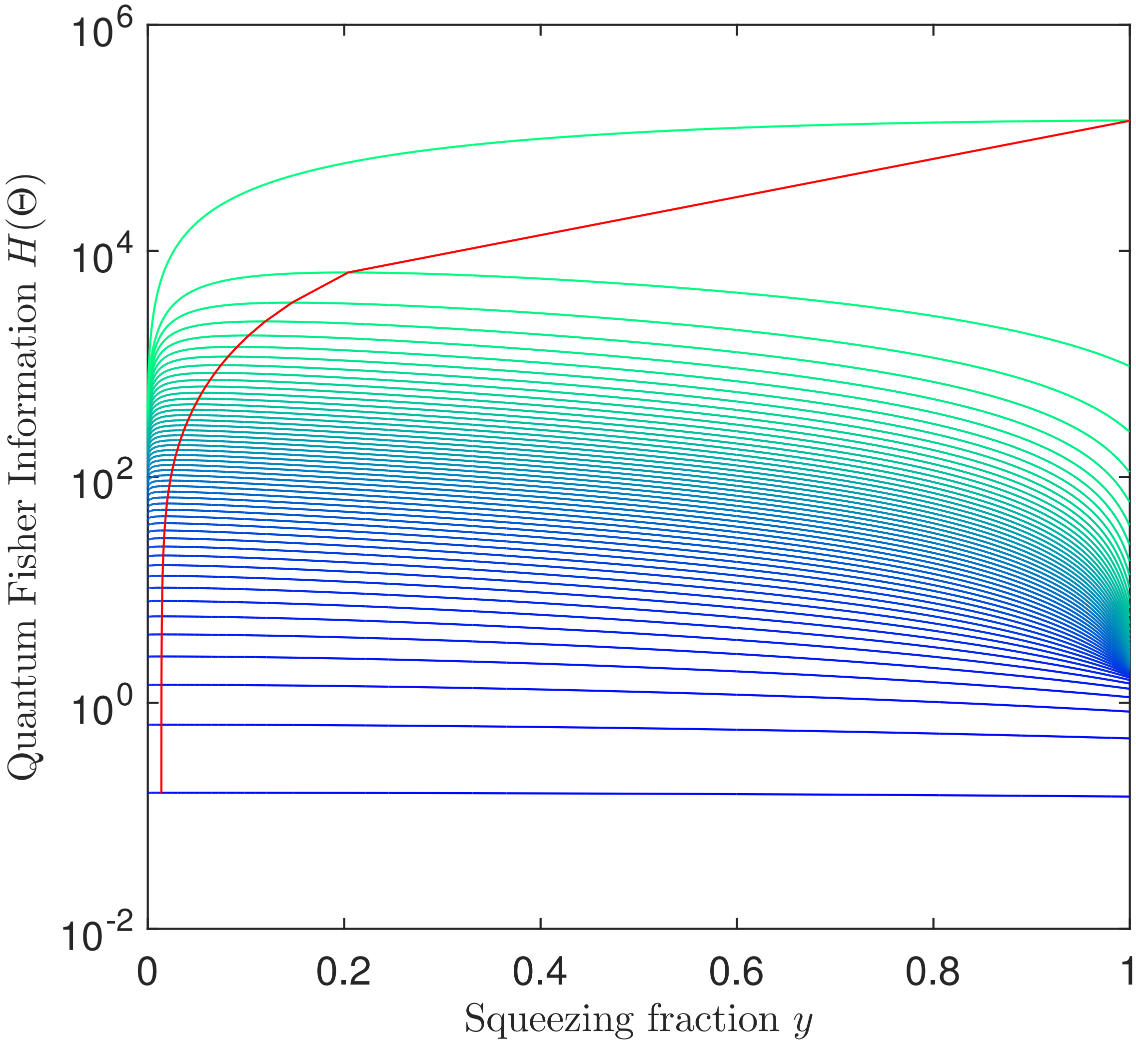

Figure 4.5: The QFI for a squeezed coherent state with probe state energy $\tilde{n} = 100$. The channel transmission t varies from $t = 0$ (blue) to $t = 1.00$ (green) in 0.02 intervals. Same Θ as in Fig. 4.4. The red line is the maximum QFI.

One can show that, the optimal angle is $\arg(\alpha) = \theta = 0$ [17]. The quantum Fisher information is simply

$$H(\Theta) = \frac{4t^2(2(\Theta t)^4 - 2(\Theta t)^2 + 1)}{(1 - t^2\Theta^2)(2\Theta^2 t^2(1 - t^2\Theta^2) + (\sinh^{-2}(r)))} + \frac{4|\alpha_0 t|^2}{\Theta^2 t^2(e^{-2r} - 1) + 1}. \quad (4.19)$$

We restrict the pure Gaussian probe state to finite energy with mean photon number $\tilde{n} = \sinh^2 r + |\alpha|^2$ and we optimize $H(\Theta)$ over the squeezed fraction $y = \sinh^2 r/\tilde{n}$. We note that the squeezing parameter r and the amplitude α are the only relevant parameters.

An estimate for Θ is needed because $H(\Theta)$ explicitly depends on the parameter we are estimating. We will graphically report the fraction of squeezed photons for maximum information if Θ is near unity. For the ideal case where $t = 1$, the quantum Fisher Information improves with more squeezing for a low number of photons as seen in figure 4.2. For $\tilde{n} \geq 100$, a large fraction of squeezed photons becomes less advantageous and it would be inefficient to squeeze all photons.

For less than ideal transmission, there is a tendency for the maximum QFI to occur for small fractions of squeezing. In figures 4.3, 4.4 and 4.5, the quantum Fisher Information is shown for three mean photon numbers $\tilde{n} = 1$, 10 and 100 and transmission coefficient t ranging from $t = 0$ to $t = 1.00$. For a small number of photons $\tilde{n} = 1$ to $\tilde{n} = 10$ and low transmission, the squeezing does not affect the information. For high transmission, the maximum information occurs for a large fraction of squeezed photons. However, for increasing number of photons $\tilde{n} \geq 100$ (see Fig. 4.5), this maximum is attained for a smaller fraction of squeezing until squeezing becomes irrelevant and fully coherent photons are the most advantageous for all levels of loss. Furthermore, for very lossy transmission, we observed that the maximum QFI occurs for a finite fraction of squeezed photons. Nonetheless, fully coherent probe states differ negligibly from the maximum QFI of these lossy channels.

Now that we have fully characterized the QFI of a lossy quantum channel, we can apply the results to the measurement of space-time parameters.

4.3 Estimating space-time parameters

Quantum metrology has been successfully applied to the design of experiments that beat the quantum shot noise limit by using quantum resources [19]. However, the physical parameters in question are non-relativistic. The effect of relativity is becoming increasingly important in quantum communications in space-based networks. Since the quantum communication protocols extend over large distances, gravitational phenomenon is of fundamental, as well as practical importance. Namely, there have been proposals for entanglement based experiments in space such as SPACEQUEST [20] and Quantum Key Distribution (QKD) protocols [9]. There have also been proposals for optical clocks in space ("The Space Optical Clocks Project") [21]. Also, effects from curved space-time on teleportation protocols were shown to affect the final fidelity [10].

In Chapter 3.3, we have seen that the space-time parameter r_s is encoded in the frequency shift of the propagating light. We can thus apply the framework of quantum metrology to design protocols with optimal quantum resources for the measurement of the gravitational redshift and therefore r_s. D. Bruschi et. al. [10] considered the fidelity of the red-shifted wavepacket received by Bob interfering with the original wavepacket sent by Alice. Therefore, we require the quantum field theory solution of the wavepacket propagating through the curved space-time as outlined in Chapter 3.7.1.

In this section, we will use the previously outlined model to estimate the space-time curvature using a lossy quantum channel. The probe state sent by Alice from Earth's surface will experience attenuation both due to scattering by the atmosphere but also from diffraction of the beam as it propagates to Bob. We will begin by presenting an approximate model for wave packets propagating in Earth's space-time as derived in Ref [10].

Earth's space-time can be approximated to be a non-rotating spherical body in the (1 + 1)- dimensional Schwarzschild metric if we assume Bob is geostationary. Therefore, the angular momentum is negligible because Alice and Bob are radially aligned. Disregarding the angular coordinates, the reduced Schwarzschild line element is $ds^2 = g_{\mu\nu}dx^\mu dx^\nu = -f(r)dt^2 + \frac{1}{f(r)}dr^2$ where $f(r) = 1 - r_s/r$ and $r_s = \frac{2GM}{c^2}$ is Earth's Schwarzschild radius [23, 24]. An observer at radius $r = r_0$ in this metric will measure the proper time $\tau = \int ds = \sqrt{f(r_0)}\ t$ where t is the proper time as measured by an observer at infinite distance $r = \infty$.

As in Chapter 3.7.1, the electromagnetic field of a photon can be described by a bosonic massless scalar field and Klein-Gordon equation $\Box\Phi = 0$ where the d'Alambertian is given by $\frac{1}{\sqrt{-g}}\partial_\mu\sqrt{-g}\ \partial^\mu$ [28]. Using the Eddington-Finkelstein coordinates as done in Ref [10], the solutions of this equation are given by outgoing $u = ct - (r + r_s \log|\frac{r}{r_s} - 1|)$ and $v = ct + (r + r_s \log|\frac{r}{r_s} - 1|)$ ingoing waves that follow geodesics [23, 24]. It it straightforward to show that the field operator Φ is expressed as the combination of bosonic annihilation and creation operators of these outgoing and ingoing waves

$$\int_0^{+\infty} d\omega[\phi_\omega^{(u)} a_\omega + \phi_\omega^{(v)} b_\omega + H.c.], \tag{4.20}$$

where u and v are the geodesic coordinates of the outgoing and incoming waves (see Chapter 3.3.1). The annihilation/creation operators obey the relations $[a_\omega, a_{\omega'}^\dagger] = [b_\omega, b_{\omega'}^\dagger] = \delta(\omega - \omega')$. We define localized annihilation and creation operators in terms of the frequency distribution $F(\omega_A)$ of the mode $\tilde{a}_{\omega_A}^\dagger = \int_0^{+\infty} d\omega_A F(\omega_A) e^{-i\omega_A \frac{u_A}{c}} a_{\omega_A}^\dagger$.

In the Schwarzschild background, the mode Bob will receive is transformed to $\tilde{a}_{\omega_B}^\dagger = \int_0^{+\infty} d\omega_B F(\omega_B) e^{-i\omega_B \frac{u_B}{c}} a_{\omega_B}^\dagger$ and if Bob tunes his detector to receive Alice's frequency distribution $F(\omega_A)$, then the field can be divided into a part which matches Bob's detector and a part which does not [26]. This is formally equivalent to a beamsplitter with transmission parameter Θ. To implement this scheme, Bob would have to employ a mode selective beamsplitter transformation that extracts the desired mode [29]. In Appendix A, we outline a method for a mode splitter using linear optics such that the commutation relation $[a, a'^\dagger] = \Theta$ holds, and Bob effectively implements a beamsplitter with transmission Θ.

The frequency $\omega_B = \sqrt{\frac{f(r_A)}{f(r_B)}}\,\omega_A$ that Bob measures is said to be gravitationally redshifted, a famous result of general relativity [24]. For any arbitrary frequency distribution, the relation between Alice's and Bob's modes can be used to find the relation in the different reference frames [22],

$$F_{\omega_{B,0}}^{(B)}(\omega_B) = \left(\frac{f(r_B)}{f(r_A)}\right)^{1/4} F_{\omega_{A,0}}^{(A)}\left(\sqrt{\frac{f(r_B)}{f(r_A)}}\,\omega_B\right). \tag{4.21}$$

Thus the effective beamsplitter ratio is characterised by the overlap of the frequency distributions sent by Alice and received by Bob. Or equivalently, the commutation relation of the annihilation and creation operators is no longer normalized.

$$[\tilde{a}_{\omega_A}, \tilde{a}_{\omega_B}^\dagger] = \int_{-\infty}^{+\infty} d\omega_B F_{\omega_{B,0}}^{*B}(\omega_B) F_{\omega_{A,0}}^{A}(\omega_B) e^{i\omega_B \frac{u_B - u_A}{c}} = \Theta, \tag{4.22}$$

where $u_B - u_A = c\tau - (r_B - r_A) - r_s \log|\frac{r_B - r_s}{r_A - r_s}|$ and τ is the proper time interval between Alice and Bob as measured by Bob at height r_B. We assume Alice and Bob directly measure their separation. Thus, Bob can tune τ such that $u_B - u_A = 0$.

Since the source is not monochromatic, we need a frequency distribution for the mode, we first assume it takes the form of a normalized Gaussian wavepacket $F(\omega) = \frac{e^{-\frac{(\omega-\omega_0)^2}{4\sigma^2}}}{(2\pi\sigma^2)^{1/4}}$ centred around the frequency ω_0 and with a spread of σ [30]. We derive a general expression for the overlap between Alice's transformed wavepacket and Bob's arbitrary choice of the Gaussian shape. For the latter, we denote Bob's detector centre frequency as $b\omega_0$ and the frequency spread $c\sigma_0$. By using equations 4.21 and 4.22, the overlap Θ for this case is given by

$$\Theta = \sqrt{\frac{2c(1-\delta)}{c^2+(1-\delta)^2}}\; e^{-\frac{(1-\delta-b)^2\omega_{B,0}^2}{4(c^2+(1-\delta)^2)\sigma^2}}, \tag{4.23}$$

where

$$\delta = 1-\sqrt{\frac{f(r_A)}{f(r_B)}} \approx \frac{r_s}{2}\frac{L+r_s\log|\frac{r_B}{r_A}|}{r_A(r_A+L+r_s\log|\frac{r_B}{r_A}|)}, \tag{4.24}$$

where $L+r_s\log|\frac{r_B}{r_A}|$ is the measured distance between Alice and Bob, and $L=r_B-r_A$. This approximation holds because r_s of Earth is very small compared to r_B and r_A. We can make a further approximation and disregard the height corrections due to the geodesic in Schwarzschild space-time since these are of the order of r_s. Therefore we are left with

$$\delta \approx \frac{r_s}{2}\frac{L}{r_A(r_A+L)}. \tag{4.25}$$

However, Bob can adjust the overlap artificially by changing the shape of his detector. We assume that Bob can adjust his detector parameters to be very closely matched with a deviation of ϵ such that $b=c=1-\epsilon$. Setting $u_B-u_A=0$ in Eq. (4.22), the overlap becomes

$$\Theta \approx e^{-\frac{(\delta-\epsilon)^2\omega_0^2}{8\sigma^2}}. \tag{4.26}$$

We denote the exponent as $x=\frac{(\delta-\epsilon)^2\omega_0^2}{8\sigma^2}$.

Since Θ is equivalent to the beamsplitter transmission parameter, we can use the quantum Fisher Information found in Eq. (4.19) to determine the Cramér-Rao bound and in particular we can incorporate the loss of the probe beam. However, to estimate the Schwarzschild parameter r_s, we must determine the corresponding quantum Fisher informations. From the definition of fidelity, this only requires the application of the chain rule such that $H(r_s)=(\frac{d\Theta}{dr_s})^2H(\Theta)$.

4.4 Relativistic Quantum Cramér-Rao Bound

The ultimate quantum limit for a space-time parameter is given by the Quantum Cramér-Rao bound. Therefore for any space-time parameter r_s that is encoded in the beamsplitter parameter $\Theta(r_s)$ or the phase $\phi(r_s)$ in an interferometer, the Quantum Cramér Rao bound is given by

$$\frac{\Delta r_s}{r_s} = \frac{1}{r_s M H(r_s)}, \tag{4.27}$$

where the quantum Fisher Information for the encoded space-time parameter is

$$H(r_s) = \left(\frac{d\Theta(r_s)}{dr_s}\right)^2 H(\Theta). \tag{4.28}$$

This simply comes from the definition of $H(\Theta)$ in terms of the second order derivative of the fidelity as in Eq. (4.8).

4.5 Estimating the Schwarzschild radius with a lossy quantum probe

In this section we will optimize our choice for the parameter Θ, and consequently the probe state energy, to provide the most precise bound on the relative error $\Delta r_s/r_s$.

In transforming $H(\Theta)$ to $H(r_s)$, the chain rule $d\Theta = \frac{d\Theta}{dr_s}dr_s = -(\frac{(\delta-\epsilon)\omega_0^2\delta}{4\sigma^2 r_s})e^{-x}dr_s = -(\frac{2x\delta}{r_s(\delta-\epsilon)})e^{-x}dr_s$ was used.

Therefore, $H(r_s) = \frac{4x^2\delta^2}{r_s^2(\delta-\epsilon)^2}H(\Theta)$ for the Gaussian frequency profile. The bound for the relative error in the Schwarzschild radius is

$$\frac{\Delta r_s}{r_s} \geq \frac{1}{r_s\frac{d\Theta}{dr_s}\sqrt{NH(\Theta)}} = \frac{4\sigma^2}{(\delta-\epsilon)\omega_0^2\delta e^{-x}\sqrt{NH(\Theta)}}. \tag{4.29}$$

Let us explore some properties of this equation. From Eq. (4.29) and the quantum Fisher information of a coherent state $H(\Theta) = |t\alpha|^2$, we can see that as $t \to 1$ and $\Theta \to 1$ which corresponds to $\epsilon \to \delta + \frac{\Delta^2}{4\delta\Omega_0^2}$, the variance diverges and it is impossible to measure the Schwarzschild radius r_s with coherent states around the point $\Theta = 1$. However, if the probe energy is completely squeezed, then the denominator reduces to

$$\begin{aligned} &\lim_{\epsilon\to\delta, t\to 1}(\delta-\epsilon)\omega_0^2\delta e^{-x}\sqrt{NH(\Theta)} \\ &= (\delta-\epsilon)\omega_0^2\delta e^{-x}\sqrt{\frac{4N\sinh^2 r}{1-\Theta^2}}. \end{aligned} \tag{4.30}$$

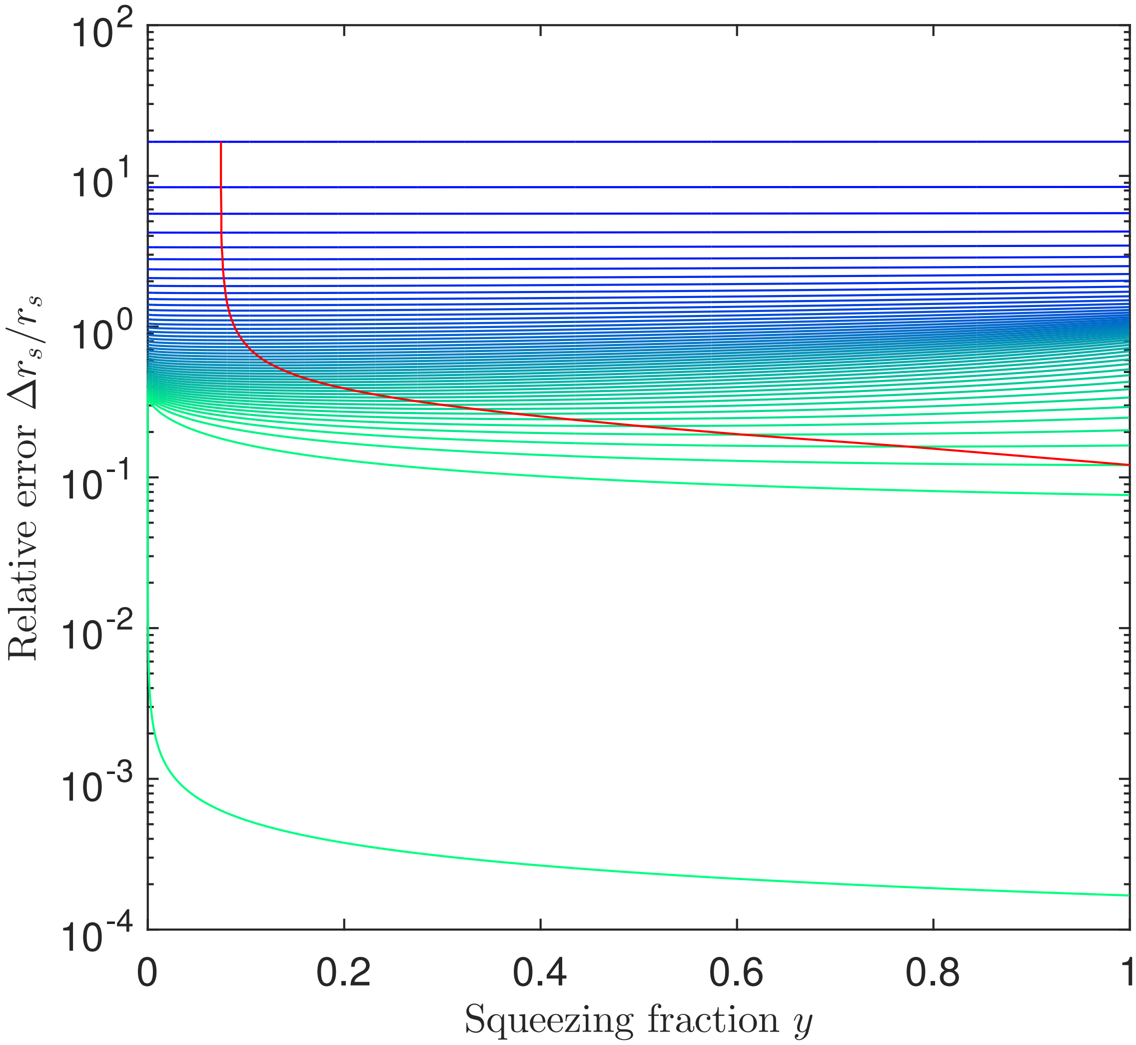

Figure 4.6: Relative error in the Schwarzschild radius versus squeezing fraction at the operating point $(\delta - \epsilon)\omega = 1$ Hz ($x = 3 \times 10^{-10}$) with $\tilde{n} = 2$ from $t = 0.02$ (blue) to $t = 1.00$ (green) in 0.02 intervals. The number of measurements in a second are $N = \sigma/10 = 2 \times 10^2$. We take $r_A = 6.37 \times 10^6$m, $r_B = 42.0 \times 10^6$ m, $\sigma = 2000\ Hz$, $\omega_0 = 700$ THz and hence $\delta = 6.0 \times 10^{-10}$. The red line is the minimum precision for each transmission.

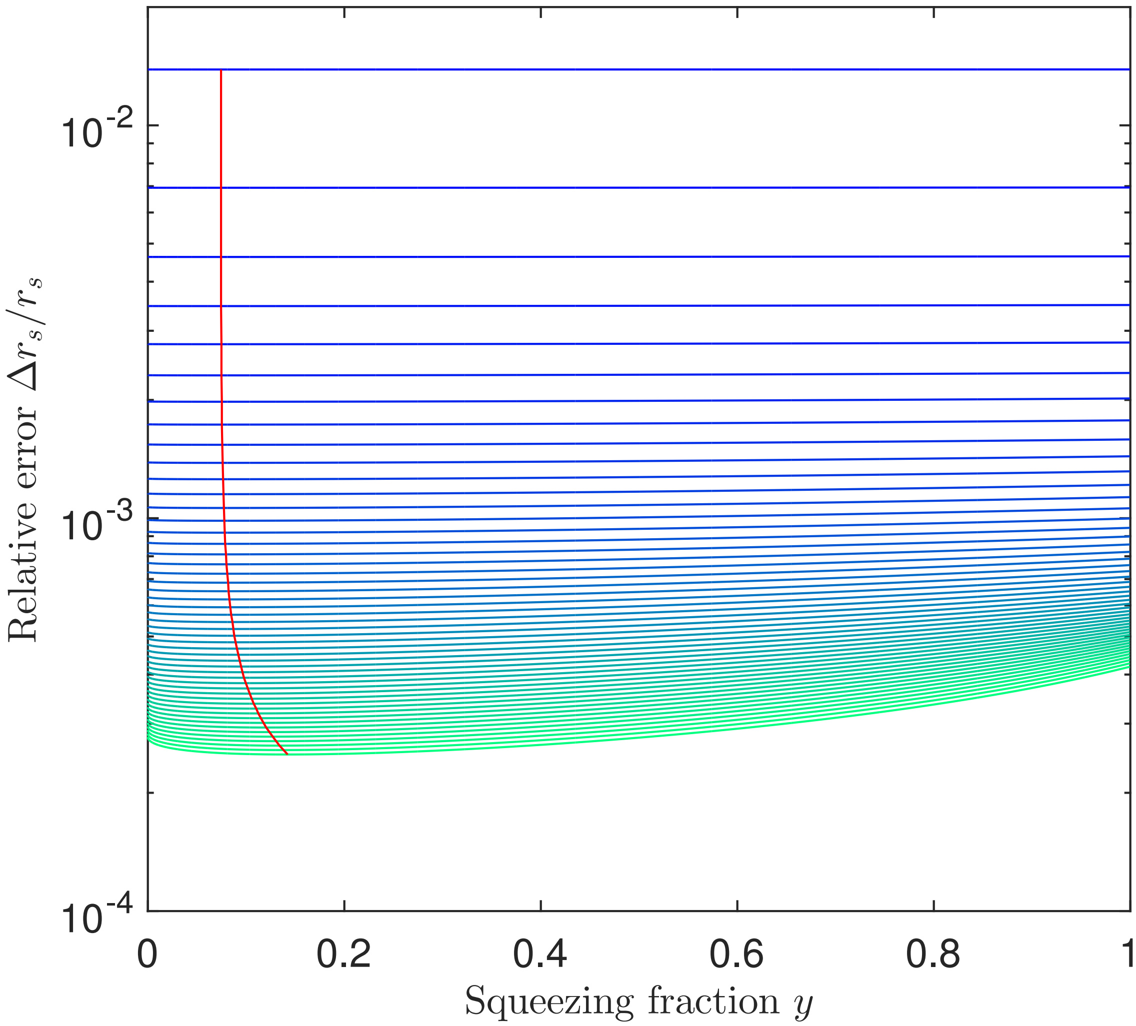

Figure 4.7: $(\delta - \epsilon_{opt})\omega = 2\sigma$ Hz ($x_{opt} = 1/2$) with $\tilde{n} = 2$ from $t = 0.02$ (blue) to $t = 1.00$ (green) in 0.02 intervals. This is the optimal operating point for coherent states. The parameters are the same as in Fig. 4.6. The red line is the minimum precision for each transmission.

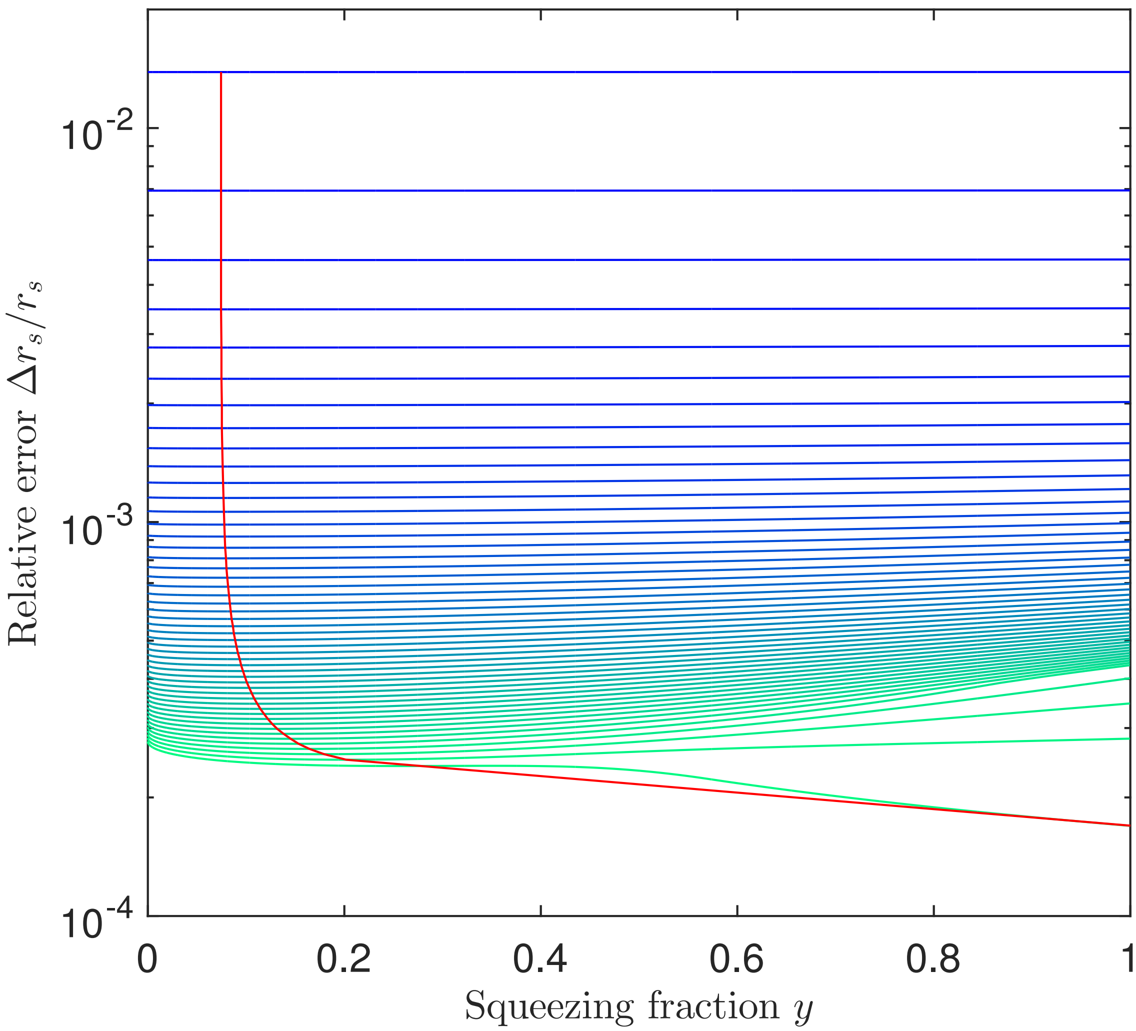

Figure 4.8: For each squeezing fraction and transmission from $t = 0.02$ (blue) to $t = 1.00$ (green) in 0.02 intervals, we have optimized for the best ϵ. Every other parameter is the same as in Fig. 4.6. The red line is the minimum precision for each transmission.

We can make further approximations about $\Theta^2 \approx 1 - 2x$. Thus, since $\frac{1}{\sqrt{2x}} \propto \frac{1}{\delta - \epsilon}$ this cancels out, and the limit is well behaved. The relative error bound of $\frac{\Delta r_s}{r_s}$ approaches

$$\frac{\Delta r_s}{r_s} \geq \frac{\sigma}{\omega_0 \delta \sqrt{N \sinh^2 r}}. \tag{4.31}$$

It is evident that coherent states do not contribute to the error bound if $\Theta = 1$ and Bob matches up his wavepacket with the one he receives $\delta = \epsilon$. Squeezing is absolutely necessary to detect the small deviation from $\Theta = 1$. As seen in Fig. 4.6, if the overlap is $\Theta = 1 - 3 \times 10^{-10}$, the error of r_s is far too large for lossy channels. The only exception is when $t = 1$ which depends strongly on the amount of squeezing.

However, if Bob's detector is using Alice's original wavepacket $\epsilon = 0$ then the error bound for coherent states is sensible

$$nc\frac{\Delta r_s}{r_s} \geq \frac{2\sigma^2}{\omega_0^2 \delta^2 e^{-x} \sqrt{N|\alpha|^2}}, \tag{4.32}$$

and no squeezing is necessary. Furthermore, we determine the optimal ϵ for which the coherent state is most advantageous. We simply minimize 4.29 with respect to ϵ to obtain $\epsilon_{opt} = \delta - \frac{2\sigma}{\omega_0}$ and $x_{opt} = \frac{1}{2}$. The r_s lower error bound for $t = 1$ is thus

$$\frac{\Delta r_s}{r_s} \geq \frac{3.3\sigma}{\omega_0 \delta \sqrt{N|\alpha|^2}}. \tag{4.33}$$

As seen in Fig. 4.7, the lossy channels now have reasonable error bounds. Finally, we can determine the optimal ϵ for a given squeezing fraction and transmission as seen in Fig. 4.8. In figure 4.8, $\frac{\Delta r_s}{r_s}$ is plotted against the fraction of squeezed photons for $\tilde{n} = 2$ average photons of the initial probe state. For low transmission t, the minimum error occurs for a small fraction of squeezing that is less than 10%. Therefore, it is more advantageous to use coherent photons for heavily attenuated signals. However, for almost perfect transmission, it is considerably more advantageous to squeeze 100% of the photons.

In figures 4.6 to 4.15 we adopt parameters similar to Ref. [10]. We assume that Alice is on the surface of Earth $r_A = 6.37 \times 10^6$m and Bob is in geostationary orbit $r_B = 42.0 \times 10^6$ m. With these parameters, we obtain $\delta = 6.0 \times 10^{-10}$. In contrast to Ref. [10], we relate the number of measurements N per second to the frequency width $\sigma = 2$ kHz. We assume that the length of the pulse is $\Delta t = 1/\sigma = 0.5\ ms$ and thus within one second, we can have up to 10^3 measurements. For minimal correlation between pulses, we assume that one pulse has 50 milliseconds of space, and as a rule of thumb $N = \sigma/10 = 2 \times 10^2$ measurements in a second. Counterintuitively, by making the width of σ smaller and thus the number of measurements smaller, we find r_s is more precise.

4.5.1 Rectangular frequency profile

It is apparent that the overlap between Alice's and Bob's Gaussian wavepackets is very near unity. However, it is known that Gaussian wave-packets are the best at maintaining their overlap given a displacement [31]. This means they are least optimal for our purposes. We require a frequency profile that is more sensitive. Hence, we consider a rectangular frequency profile. In the time-domain, this would correspond to a sinc(kt) function.

For a normalised rectangular function of width σ_0 and height $1/\sqrt{\sigma_0}$ at frequency ω_0, we wish to calculate the overlap with the transformed rectangular function in Bob's reference frame. From Eq. (4.21), Bob measures the width $\sqrt{\frac{f(r_A)}{f(r_B)}}\,\sigma_0$ and height $\frac{1}{\sqrt{\sigma_1}} = \frac{1}{\sqrt{\sqrt{\frac{f(r_A)}{f(r_B)}}\,\sigma_0}}$ centred at frequency $\omega_1 = \sqrt{\frac{f(r_A)}{f(r_B)}}\,\omega_0$. The rectangular function profile must be normalised $\int_{-\infty}^{+\infty} d\omega_B |F_B(\omega_B)|^2 = 1$. Since $\sqrt{\frac{f(r_A)}{f(r_B)}} < 1$, the transformed rectangular function will have lower frequency and smaller overall width but larger height. Thus, making use of Eq. (4.22), the overlap is

$$\Theta = \begin{cases} [\omega_B + \frac{\sigma_B}{2} - (\omega_A - \frac{\sigma_A}{2})]\frac{1}{\sqrt{\sigma_B\sigma_A}}, & \omega_B + \frac{\sigma_B}{2} > \omega_A - \frac{\sigma_A}{2} \\ 0, & \omega_B + \frac{\sigma_B}{2} < \omega_A - \frac{\sigma_A}{2} \end{cases} \tag{4.34}$$

Bob can adjust his detector by varying the central frequency ω_0 by an arbitrary factor b and also the frequency spread σ_0 by a factor of c. Therefore,

$$\begin{aligned} \Theta &= \frac{[(\sqrt{\frac{f(r_A)}{f(r_B)}}\,\omega_0 + \frac{\sqrt{\frac{f(r_A)}{f(r_B)}}\,\sigma_0}{2}) - (b\omega_0 - \frac{c\sigma_0}{2})]}{(\frac{f(r_A)}{f(r_B)})^{1/4}\sqrt{c}\,\sigma_0} \\ &= \frac{\omega_0}{\sigma_0}\left(\frac{1}{\sqrt{c}}\left(\frac{f(r_A)}{f(r_B)}\right)^{1/4} - \frac{b}{\sqrt{c}}\left(\frac{f(r_A)}{f(r_B)}\right)^{-1/4}\right) \\ &+ \frac{1}{2}\left(\frac{1}{\sqrt{c}}\left(\frac{f(r_A)}{f(r_B)}\right)^{1/4} + \sqrt{c}\left(\frac{f(r_A)}{f(r_B)}\right)^{-1/4}\right). \end{aligned} \tag{4.35}$$

We note the useful approximation $\left(\frac{f(r_A)}{f(r_B)}\right)^{1/4} \approx 1 - \frac{r_s L}{4r_A r_B} = 1 - \frac{\delta}{2}$ and $\left(\frac{f(r_A)}{f(r_B)}\right)^{-1/4} \approx 1 + \frac{r_s L}{4r_A r_B} = 1 + \frac{\delta}{2}$. This approximation holds if r_s is extremely small as is the case for Earth. We can further set the factors $b = c = 1 - \epsilon$. We make the necessary approximations and keep terms to first order

$$\begin{aligned}\Theta = \frac{\omega_0}{\sigma_0}\left((1+\frac{\epsilon}{2})(1-\frac{\delta}{2}) - (1-\frac{\epsilon}{2})(1+\frac{\delta}{2})\right) \\ + \frac{1}{2}\left((1+\frac{\epsilon}{2})(1-\frac{\delta}{2}) + (1-\frac{\epsilon}{2})(1+\frac{\delta}{2})\right) \\ = 1 - \frac{\omega_0|\delta-\epsilon|}{\sigma_0}.\end{aligned} \tag{4.36}$$

In the last step, we have generalised to the case when Bob adjusts his detector to overestimate the frequency spread and central frequency. Thus $\epsilon > \delta$ but the overlap will remain smaller than unity, as expected. The expression above is only valid if $\omega_0 > \frac{\sigma_0}{2}$ because we are disregarding the negative frequencies. For sufficiently large $\frac{\omega_0}{\sigma_0}$, the rectangular frequency profiles will no longer overlap because of the gravitational redshift $\Theta = 0$. The modes remain completely orthogonal for $\frac{\omega_0}{\sigma_0} \geq \frac{1}{|\delta-\epsilon|}$. The error lower bound for r_s is

$$\frac{\Delta r_s}{r_s} \geq \frac{\sigma_0}{\omega_0\delta\sqrt{NH(\Theta)}}. \tag{4.37}$$

We note that there is a discontinuity at $\delta = \epsilon$ and the derivative w.r.t. r_s of the absolute value is undefined at this point. However, in reality we adopt a continuous frequency distribution and thus Θ will have a well defined derivative. We note that for a coherent state, in the limit that $t \to 1$ and $\epsilon \to \delta$, the error lower bound for r_s is

$$\frac{\Delta r_s}{r_s} \geq \frac{\sigma}{2\omega_0\delta\sqrt{N|\alpha|^2}}. \tag{4.38}$$

This behaviour is evident in Fig. 4.9, where the overlap is $\Theta = 1/2$, there is small dependence on the squeezing fraction. In comparison, the optimal point of the Gaussian is up to a factor of 5 worse than for the same overlap using the rectangular frequency profile. Conversely, for a fully squeezed probe state, we can express the error bound as

$$\frac{\Delta r_s}{r_s} \geq \frac{\sqrt{\sigma_0(\delta-\epsilon)}}{\sqrt{2\omega_0}\,\delta\sqrt{N\sinh^2 r}}. \tag{4.39}$$

This indicates that the bound can approach 0 up to an error in matching up the exact frequency distribution. For example, if Bob's detector guesses the correct distribution within $(\delta - \epsilon)\omega = 1$ Hz then a perfect channel would have 10^{-6} precision.

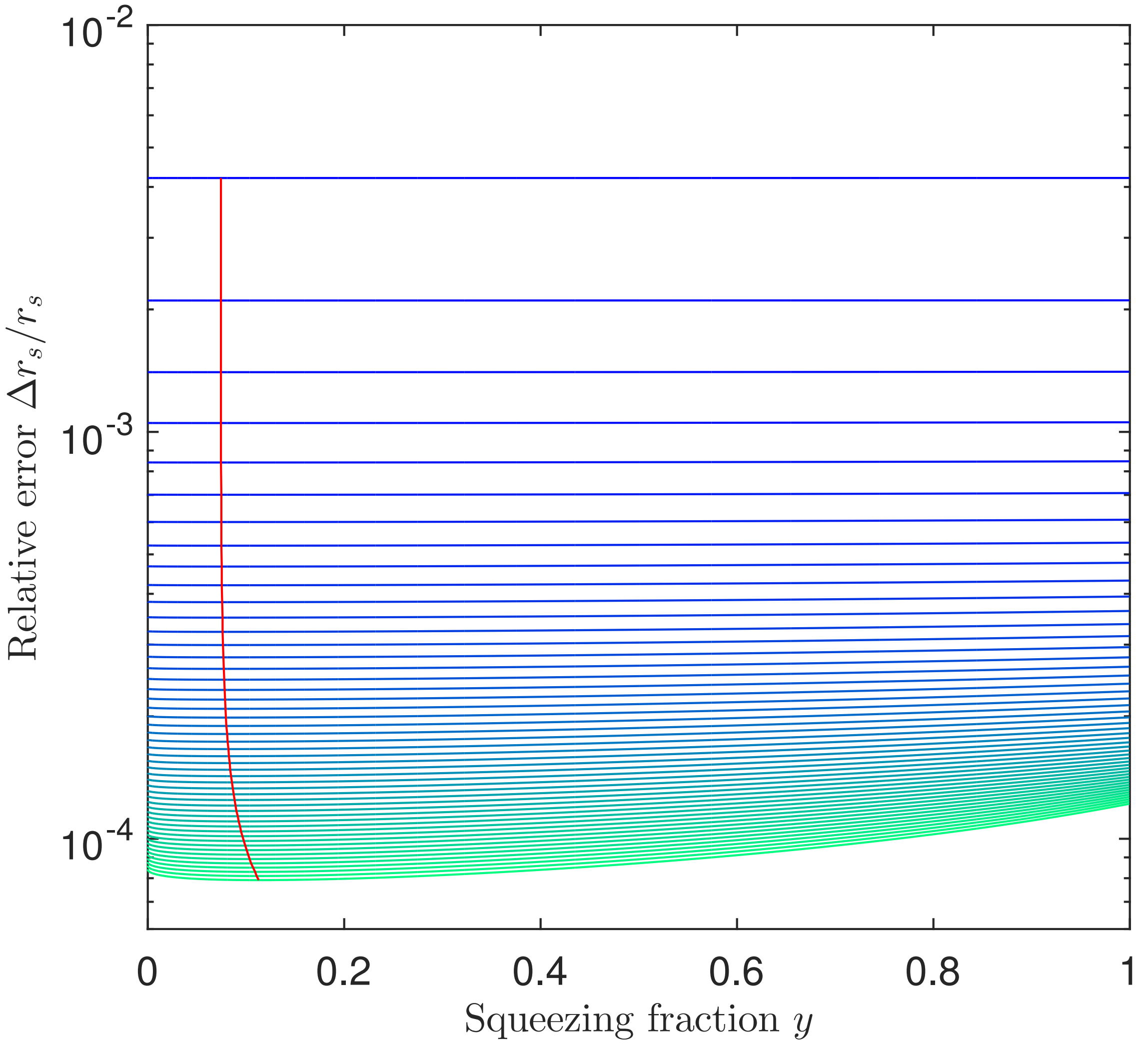

Figure 4.9: Relative error in the Schwarzschild radius with total probe state energy $\tilde{n} = 2$ for rectangular frequency profile. Squeezing is not effective. The number of measurements are $N = 2 \times 10^2$ in a second. The transmission coefficient varies $t = 0.02$ (blue) to $t = 1.00$ (green) in 0.02 intervals. (Parameters: $(\delta - \epsilon)\omega = \sigma/2$ Hz ($x = 1/2$) with $\tilde{n} = 2$ and $N = 2 \times 10^2$ measurements). The red line is the minimum precision for each transmission.

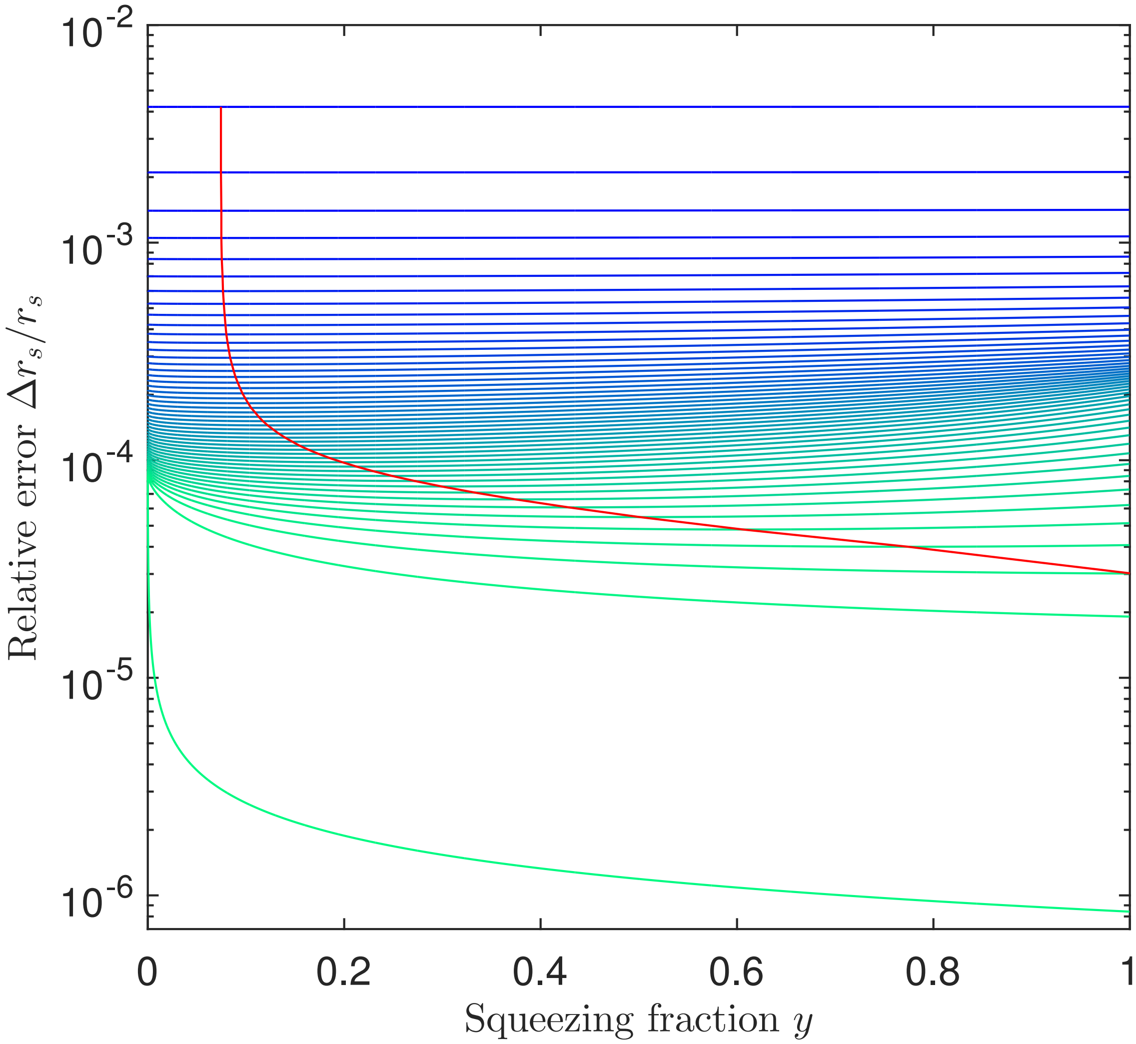

Figure 4.10: Same parameters as in Fig. 4.9 with the exception $(\delta - \epsilon)\omega = 1$ Hz ($x = 5 \times 10^{-5}$) with $\tilde{n} = 2$. In this regime, the rectangular frequency profile is 100 times more precise than the optimal Gaussian point if the initial probe state is fully squeezed. The red line is the minimum precision for each transmission.

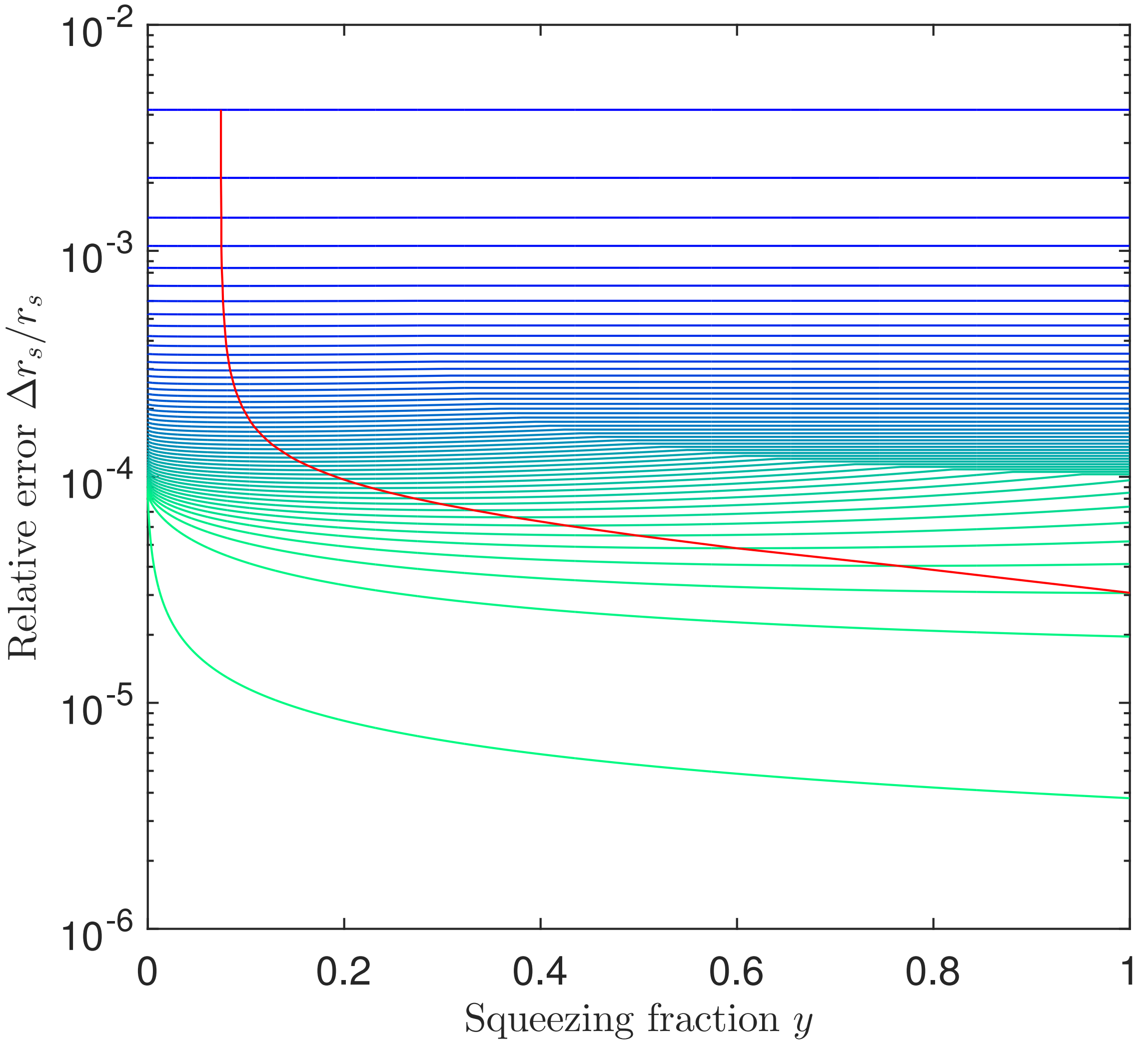

Figure 4.11: For each squeezing fraction and transmission, we have optimized for the best ϵ (not including $t = 1$ which is optimal at $\delta = \epsilon$ and approaches 0). The red line is the minimum precision for each transmission.

As seen in Fig. 4.10 and Fig. 4.8, squeezing is clearly advantageous. In comparison to the best Gaussian precision, the rectangular frequency profile does 2 orders of magnitude better.

4.6 More Realistic Scenarios

4.6.1 Non-ideal rectangular frequency profile

The shape of the rectangular frequency profile we have used is an ideal representation with infinitely sharp edges which is unphysical. We can smooth the edges using a $\tanh \omega$ function as follows

$$F(\omega_B) = \frac{\tanh \frac{\sigma+2(\omega_B-\omega_0)}{\Delta\sigma} + \tanh \frac{\sigma-2(\omega_B-\omega_0)}{\Delta\sigma}}{2\sqrt{\Delta\sigma(-\frac{1}{2}+\frac{1}{\Delta}\coth\frac{2}{\Delta})}}. \tag{4.40}$$

As the parameter $\Delta \to 0$, the frequency profile approaches a rectangular function. In the time domain, the Fourier transform of 4.40 is proportional to $\frac{\sin \sigma t}{\sinh \Delta\pi\sigma t/2}$. The function falls off exponentially depending on Δ. We use the transformation in Eq. (4.21) and we similarly give Bob the freedom to choose the frequency spread $b\sigma_0$ and central frequency $b\omega_0$ of his detector. The overlap is thus (after normalization of Eq. (4.40))

$$\Theta = \int_{-\infty}^{+\infty} d\omega \frac{(\tanh[\frac{\sigma+\frac{\omega}{a}-\omega_0}{\Delta\sigma}] + \tanh[\frac{\sigma-\frac{\omega}{a}+\omega_0}{\Delta\sigma}])}{4\sqrt{a\Delta\sigma(-1+\frac{2\coth[\frac{2}{\Delta}]}{\Delta})}} \times \frac{(\tanh[\frac{\sigma+\frac{\omega}{b}-\omega_0}{\Delta\sigma}] + \tanh[\frac{\sigma-\frac{\omega}{b}+\omega_0}{\Delta\sigma}])}{\sqrt{b\Delta\sigma(-1+\frac{2\coth[\frac{2}{\Delta}]}{\Delta})}}. \tag{4.41}$$

We can further simplify this equation and group the constants $\Theta = K\theta(\omega)$, where the proportionality constant is

$$K = \frac{\tanh[\frac{2}{\Delta}]^2}{\Delta\sigma\sqrt{ab}\,(-1+\frac{2\coth[\frac{2}{\Delta}]}{\Delta})}, \tag{4.42}$$

and

$$\theta(\omega) = \int_{-\infty}^{+\infty} \frac{d\omega}{(1+\cosh[\frac{4(-a\omega_0+\omega)}{\Delta a\sigma}]/\cosh[\frac{2}{\Delta}])} \times \frac{1}{(1+\cosh[\frac{4(-b\omega_0+\omega)}{\Delta b\omega_0}]/\cosh[\frac{2}{\Delta}])}. \tag{4.43}$$

There is no closed form of this integral. However, we can make some approximations since $a = 1-\delta$ and $b = 1-\epsilon$ where δ and ϵ are very small. We also can suppose that the bounds of the integral are very close to the central frequency ω_0 with the bounds extending over a region of width σ across the central frequency. For the choice of $\Delta = 0.1$ and $\Delta = 0.01$, the overlap of the latter is approximately rectangular as seen in Fig. 4.12. Furthermore, the overlap as a function of δ is continuous at the point $\delta = \epsilon$ and the derivative with respect to r_s exists in contrast to the ideal rectangular frequency profile. Approaching δ^- from below has the same minimum as approaching from above (as seen in Fig. 4.14) since the frequency profile is symmetric. For the larger $\Delta = 0.1$, the same behaviour occurs but the relative error of r_s is larger than for the case of $\Delta = 0.01$.

In Fig. 4.15, we present the Schwarzschild radius lower error bound optimized for each squeezing fraction y and transmission parameter t. Using the Θ in Fig. 4.13 we determined $r_s \frac{d\Theta}{dr_s} = r_s \frac{d\delta}{dr_s}\frac{d\Theta}{d\delta}$ and thus the optimal Θ that minimizes $\Delta r_s / r_s$. The behaviour is very similar to the rectangular frequency profile. We note that $t = 1$ is bounded because $\frac{d\Theta}{dr_s} \to 0$ as $\delta^{\pm} \to \epsilon$ (when Alice matches exactly the frequency profile that Bob receives) and the relative error of r_s approaches a limit.

4.6.2 Large coherent pulses with additional squeezing

For large scale interferometers such as GEO and the Laser Interferometer Gravitational-Wave Observatory (LIGO), it has been shown that coherent sources of light with large amplitude and additional squeezing can significantly improve the detector sensitivity [34].

For the Gaussian frequency profile, operating at the optimal point $x_{opt} = 1/2$ requires coherent states with large amplitude rather than squeezed states. As seen in Fig. 4.16, the addition of squeezing does not significantly improve the precision.

Conversely, for the rectangular frequency distribution, squeezing significantly improves the precision. As seen in Fig. 4.17, for good transmission coefficients, squeezing increases the precision up to a factor of $\frac{1}{2}$ for 17.4 dB of squeezing. Current state-of-art technologies have been able to achieve squeezing of up to 15 dB [35]. In both cases, the error improves with additional coherent photons.

4.6.3 Optimal position of Bob

Up to this point we have assumed that Bob is located in a geo-stationary orbit and that different levels of loss can be achieved. We consider a more realistic scenario in which the loss is a function of Bob's position relative to the ground is and investigate the position of Bob for which the relative Schwarzschild radius error is minimal. We

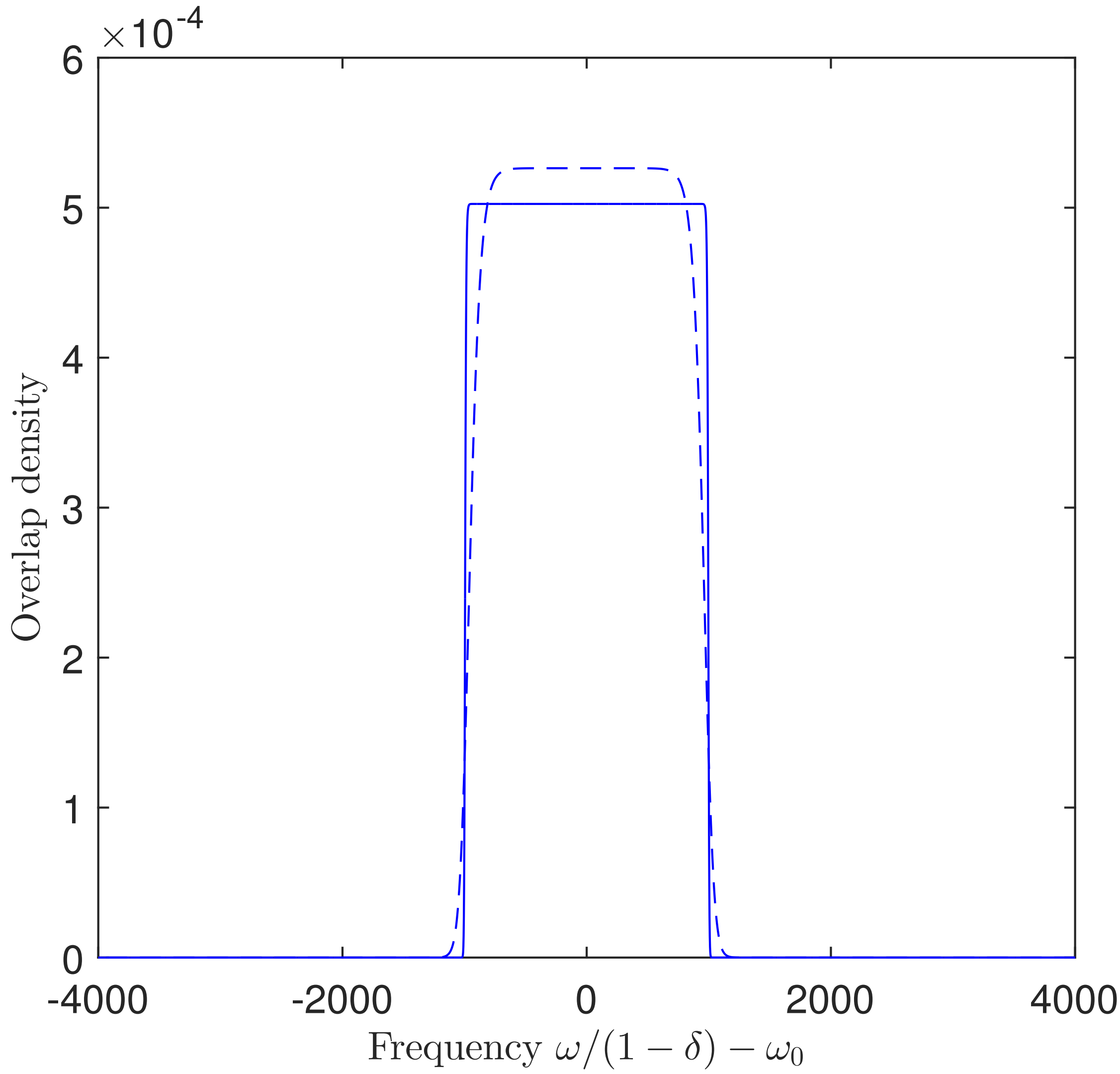

Figure 4.12: The frequency profile squared for $\Delta = 0.01$ (solid line) and $\Delta = 0.1$ (dashed line) plotted against the shifted and rescaled frequency $\frac{\omega}{1-\delta_0} - \omega_0$. We take $r_A = 6.37 \times 10^6$m, $r_B = 42.0 \times 10^6$ m, $\sigma = 2000$, $\omega_0 = 700$ THz and hence $\delta = 6.0 \times 10^{-10}$ (the same as in Section 4.5).

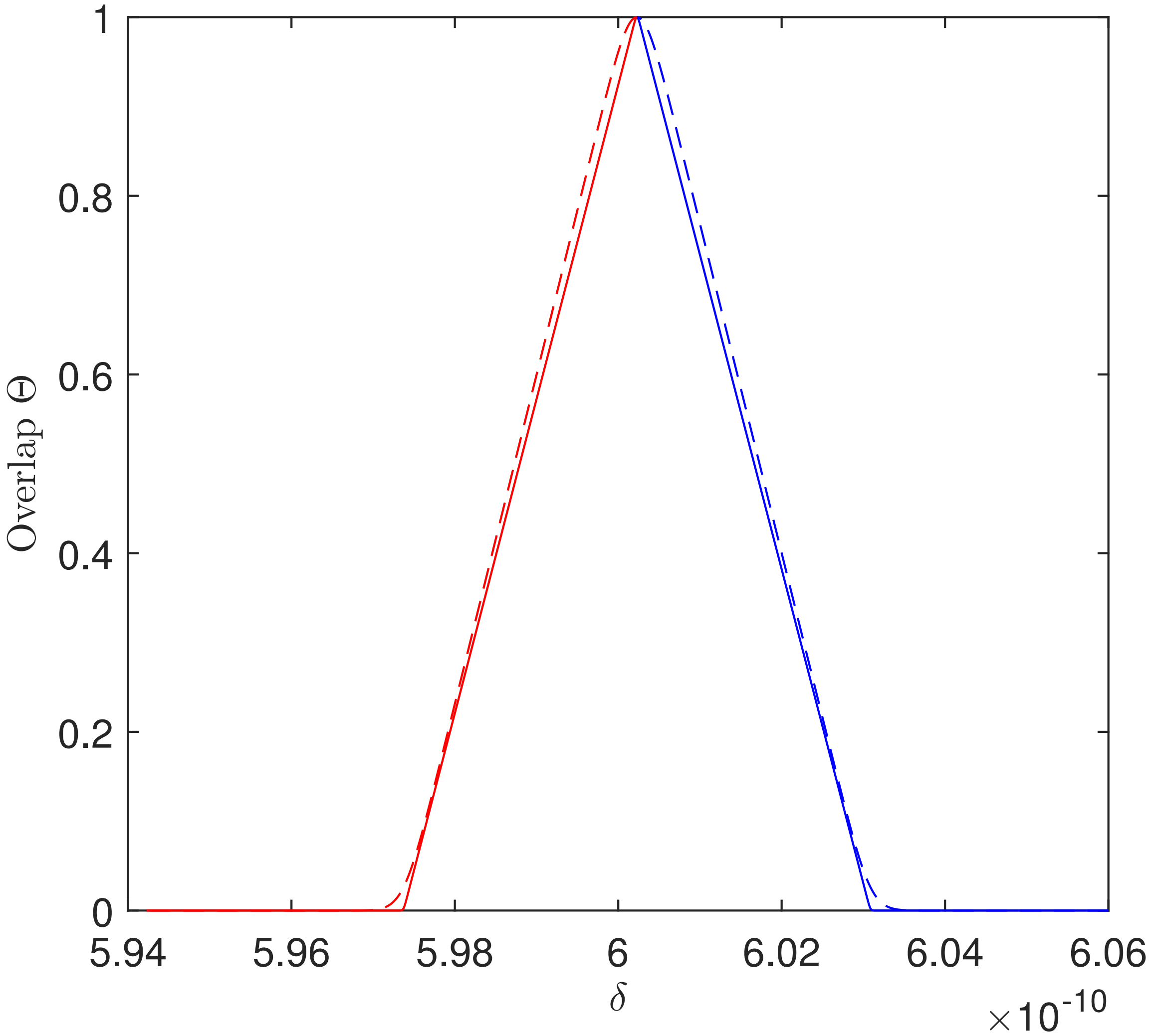

Figure 4.13: We vary δ around the fixed point $\epsilon = \delta_0$ and plot the overlap Θ. Here we see a sharp turn at this point for $\Delta = 0.01$ (solid line) but for $\Delta = 0.1$ (dashed line), the Θ dependence on δ is smoother. The parameters are the same as in Fig. 4.12.

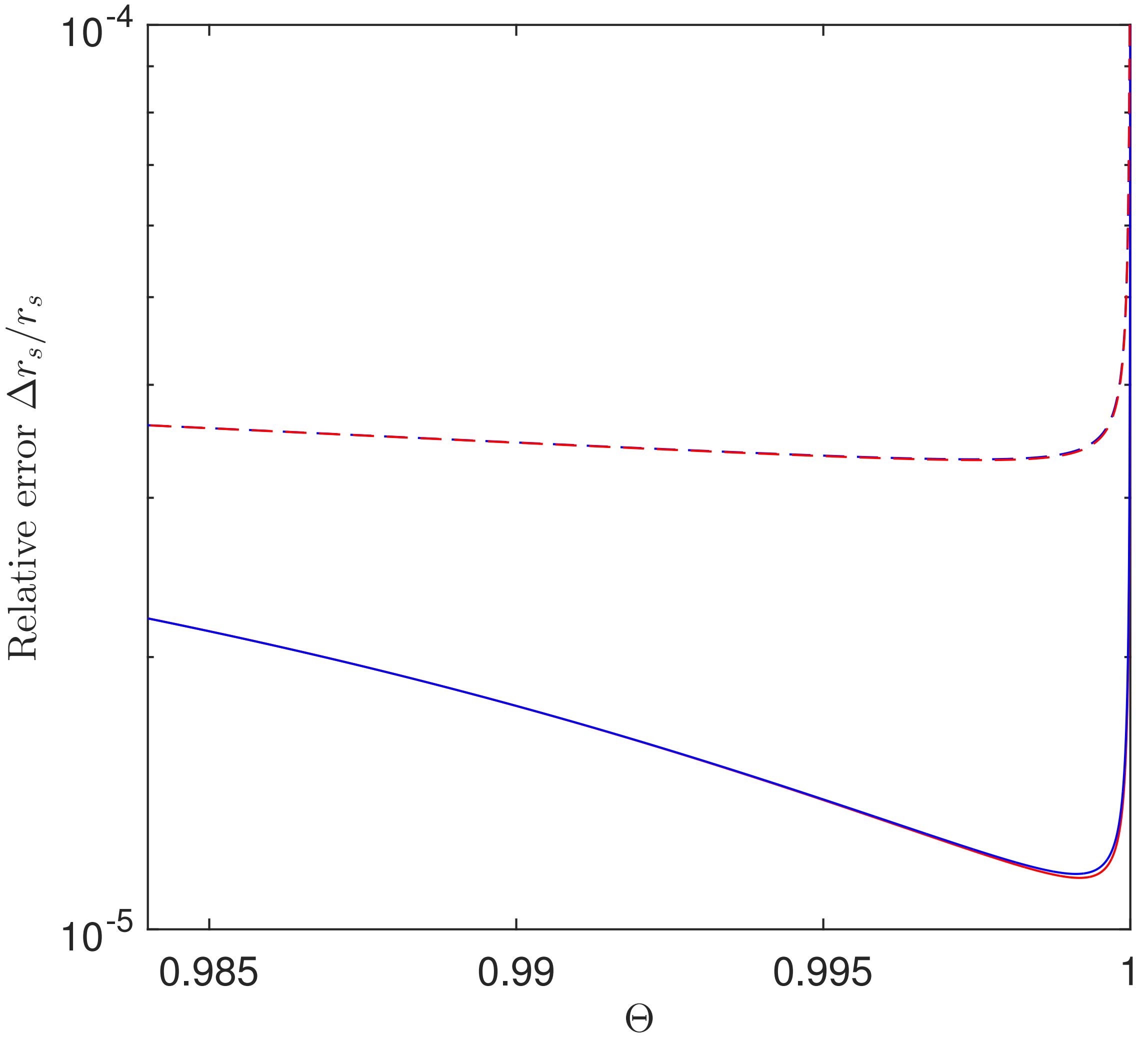

Figure 4.14: At $t = 1$ for a fully squeezed probe state of $\tilde{n} = 2$, we plot the limit as $\Theta \to 1$. We note that the optimal point is before this limit. The reason for this is the competing effect of $\frac{d\Theta}{dr_s}$. In this case, the derivative $\frac{d\Theta}{dr_s} = 0$ at $\Theta = 1$ and we are not impeded by the discontinuity that arose in the rectangular frequency profile. The red line is δ^- from below and the blue line from above δ^+. These two lines are essentially equivalent. Note: the solid line corresponds to $\Delta = 0.01$ and the dashed line to $\Delta = 0.1$.

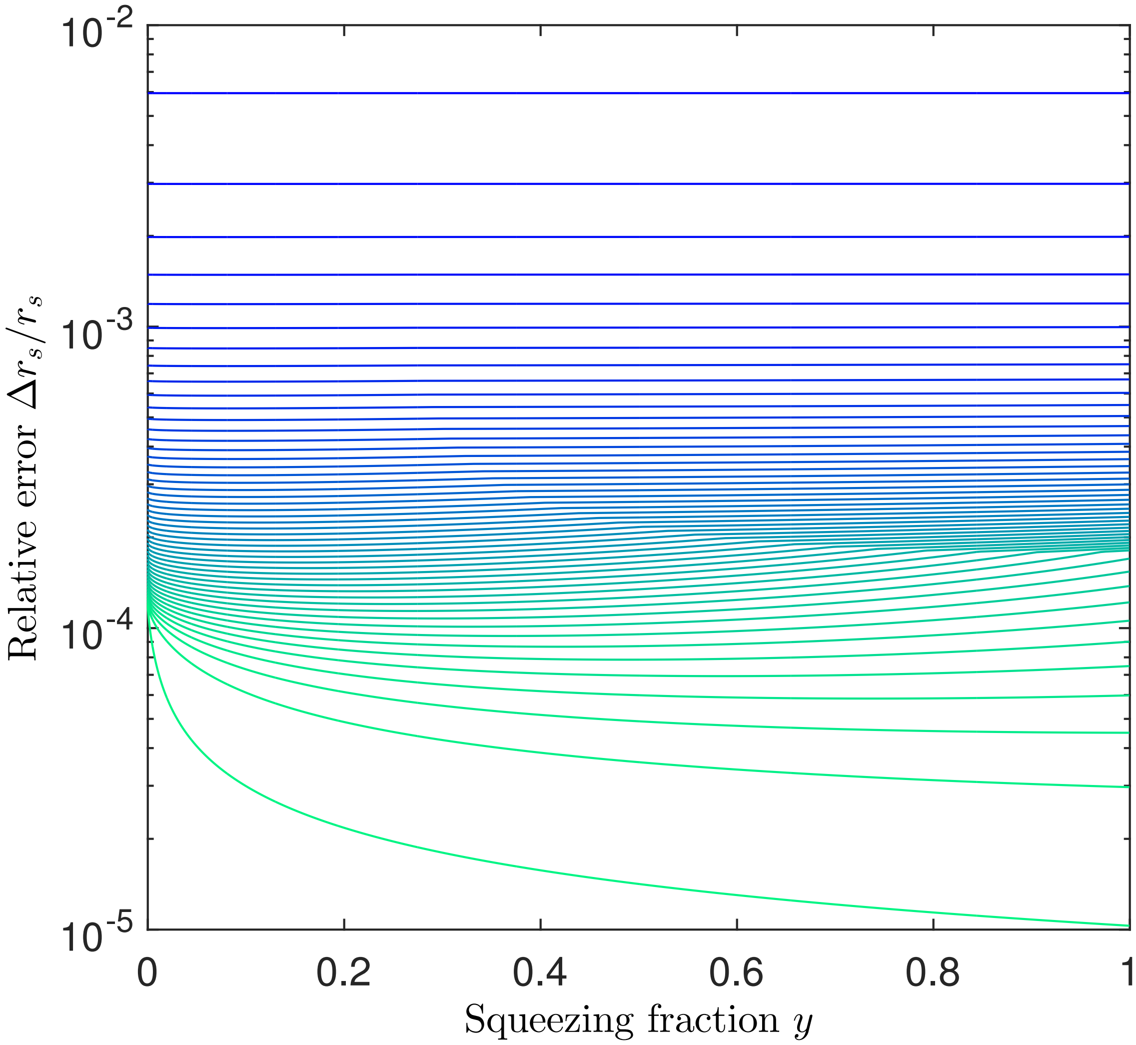

Figure 4.15: The Schwarzschild radius lower error bound optimized for each squeezing fraction y and transmission parameter t for the smoothed rectangular function. Using the Θ in Fig. 4.13 we determined $r_s\frac{d\Theta}{dr_s} = r_s\frac{d\delta}{dr_s}\frac{d\Theta}{d\delta}$ and determined the optimal Θ that minimizes $\Delta r_s/r_s$. We note that $t = 1$ is bounded because $\frac{d\Theta}{dr_s} \to 0$ as $\delta \to \epsilon$ and the relative error of r_s approaches a limit.(Other parameters: $\Delta = 0.01$, $\tilde{n} = 2$).

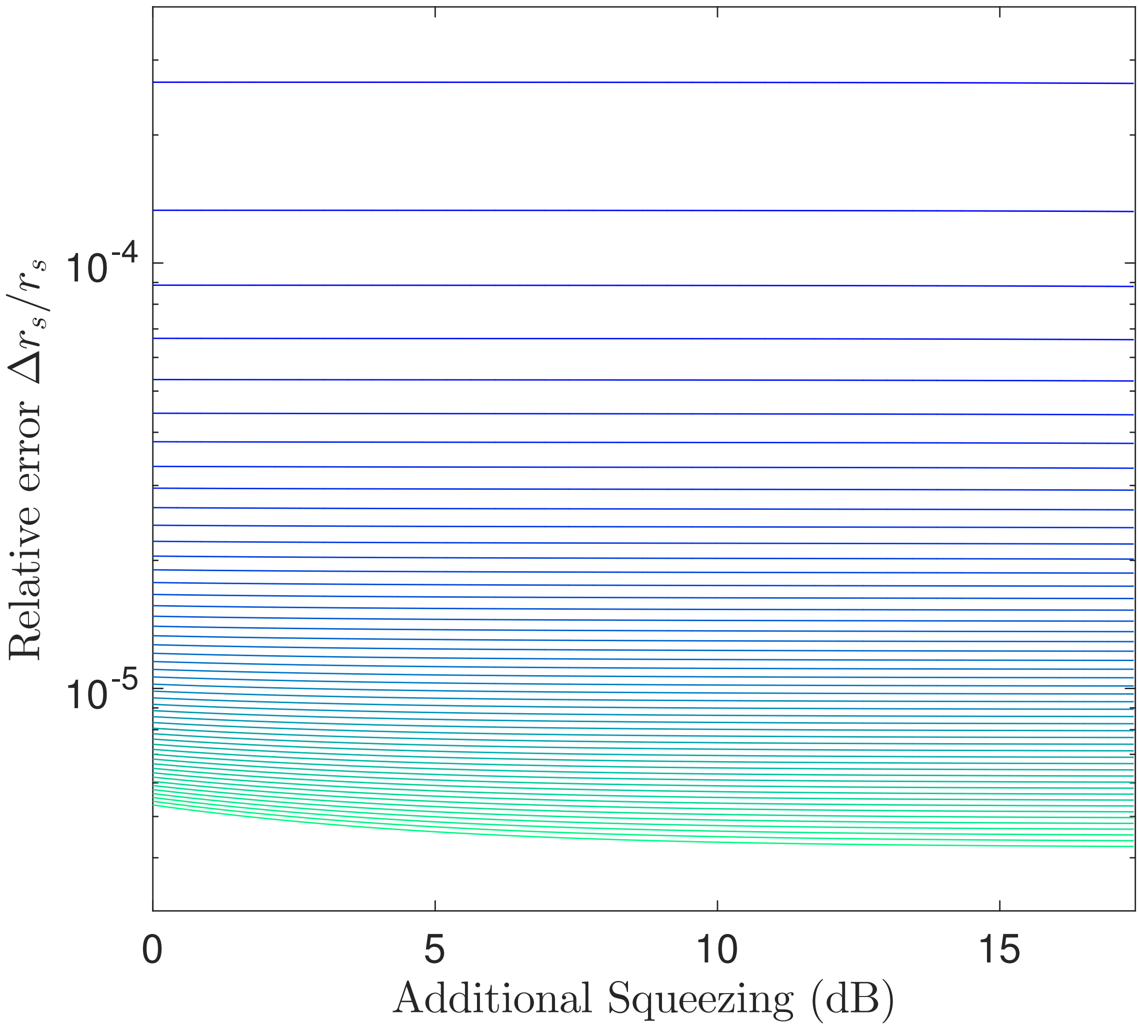

Figure 4.16: The relative Schwarzschild error for a coherent pulse of energy $\tilde{n} = 1000$ with injection of additional squeezing for Gaussian frequency profile at optimal operating point $x_{opt} = 1/2$. The squeezing parameter is given in units of decibels with respect to the shot noise quadrature variance. Squeezing has little effect on the lossy channels. (Parameters: $(\delta - \epsilon_{opt})\omega_0 = 2\sigma$ Hz and all other parameters the same as in Fig. 4.12).

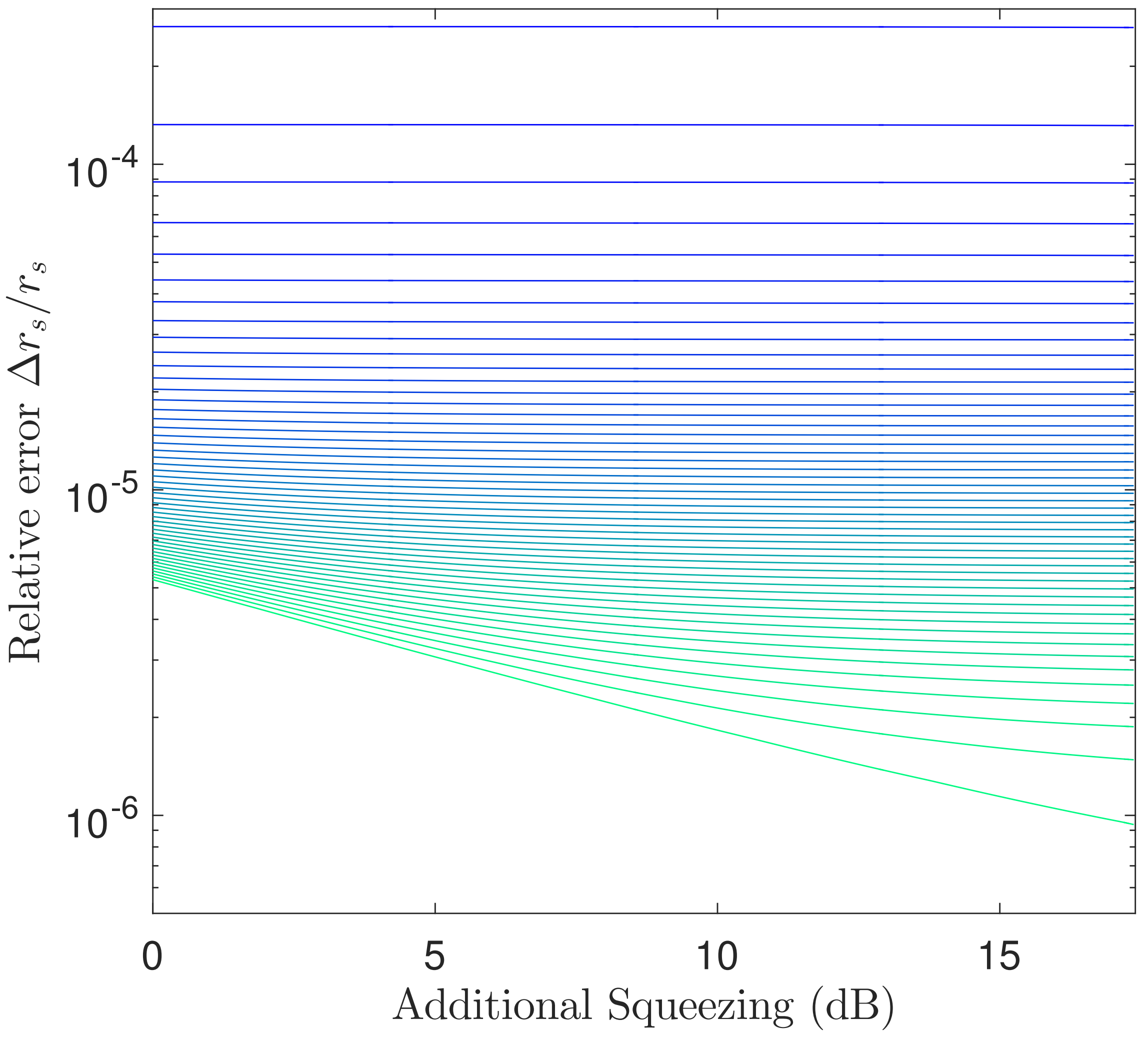

Figure 4.17: As in Fig. 4.16 but for $\Delta = 0.01$ rectangular frequency profile at the optimal operating point $\Theta = 0.999$ with $\tilde{n} = 1000$. For almost no loss, squeezing improves the error bound up to a factor of $\frac{1}{2}$ for 17.4 dB of squeezing.

model the attenuation with distance of the Gaussian beam using the characteristic Rayleigh length defined by $z_R = \frac{\pi w_0^2}{\lambda}$ where w_0 is the width of the beam and λ is the centre wavelength [36]. The initial position of Bob corresponds to the position of the Rayleigh length and we assume that the detector has a width $\sqrt{2}\, w_0$ which captures all the intensity. Therefore, the transmission coefficient $t = 1$ at this point. Away from the Rayleigh length, the transmission decreases with distance L as

$$t = t_0 \sqrt{\frac{2}{1 + \left(\frac{L}{z_R}\right)^2}} \, . \tag{4.44}$$

For the Gaussian frequency profile, the relative Schwarzschild error is plotted in Fig. 4.18 for two Rayleigh lengths (blue curves). We compare between fully coherent photon probe states $\tilde{n} = 1000$ (solid lines) and with additional squeezing of 10 dB (dashed lines). With 10 dB of squeezing, if Bob's distance is exactly at the Rayleigh length, the error is of the same order as the minima at $L \approx 10^5$ m. Nonetheless, the best situation is when $z_R = 10^3$ m corresponding to a beam width of $w_0 = 1.4$ cm which has a minimum error of 10^{-1} between $L = 10^4$ m and $L = 10^6$ m. Squeezing has no effect on this minimum because the signal is heavily attenuated at Bob's location. For the Gaussian frequency profile, the best relative error is rather poor. We now present the tanh rectangular frequency profile as an alternative to this resource intensive scheme.

Now consider the red curves in Fig. 4.18, which report the relative error for the same parameters using a rectangular frequency profile with $\Delta = 0.001$. We immediately note for the squeezed coherent probe state that there are no minima at any location. The minimum occurs at the Rayleigh lengths (where $t = 1$) with an impressive 1 order of magnitude improvement in precision over the Gaussian frequency profile. Thus, it is now possible to measure the Schwarzschild radius with excellent precision with Bob at the Rayleigh lengths $L = z_R = 100$ m and $L = z_R = 1000$ m to achieve 10^{-1} and 10^{-2} relative error respectively. We note that squeezing has a significant effect at the Rayleigh length because $\Theta \approx 1$ since L is small and the transmission coefficient is $t = 1$. In this regime, squeezing becomes important. We observe that the precision increases up to a factor of 5×10^{-1} for both Rayleigh lengths with the added 10 dB of squeezing. However, for fully coherent photons, the minima are recovered and occur at approximately $L = 10^5$ m. Therefore, a $\Delta = 0.001$ rectangular frequency profile works well for short distances and is always up to 10 times more precise than Gaussian profiles of the same frequency spread.

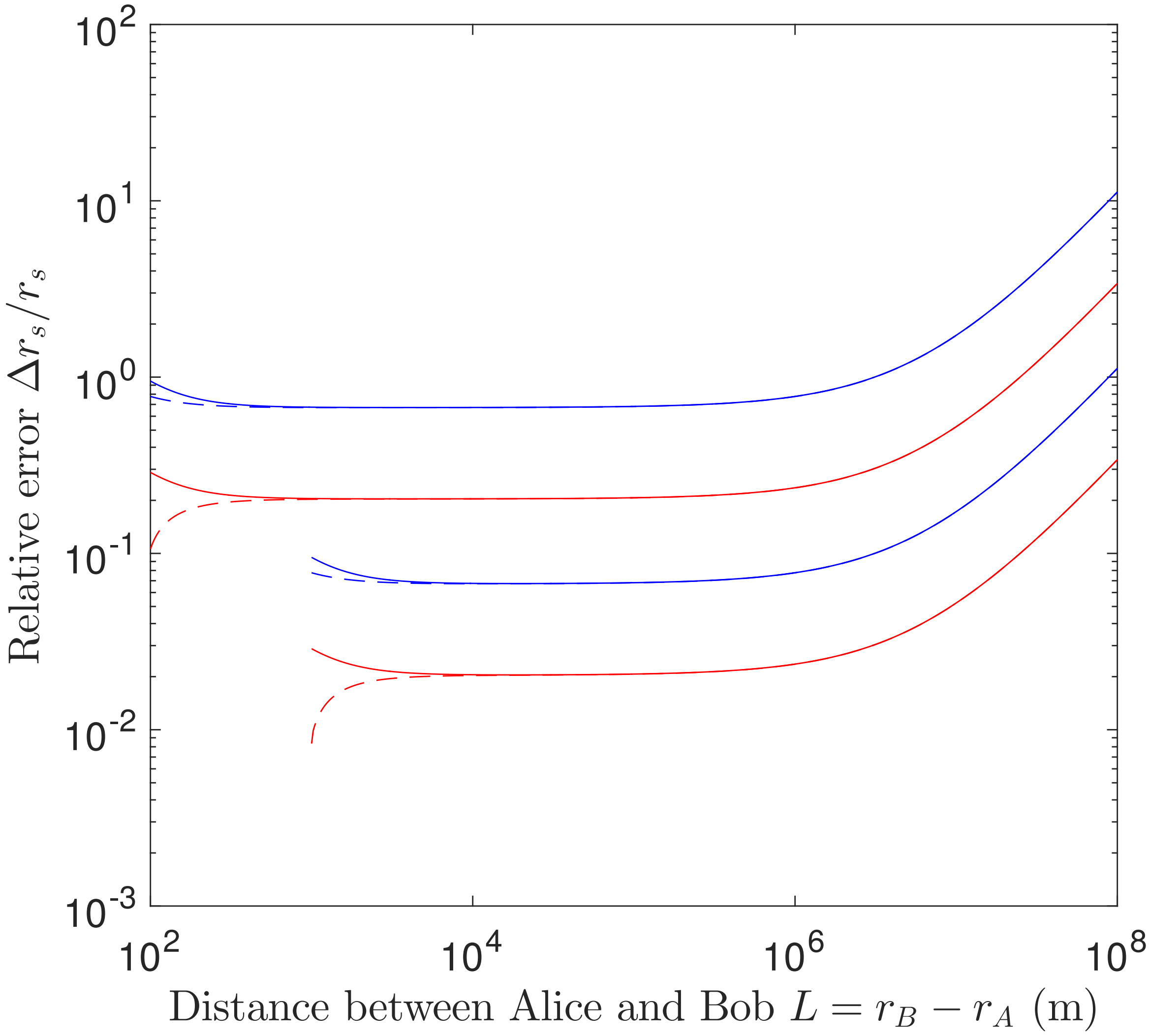

Figure 4.18: Log- log plot of relative Schwarzschild error for Rayleigh lengths $z_R = 100$m and $z_R = 1000$m using Gaussian frequency profile (blue) at the optimal point $x = 1/2$ and $\Delta = 0.001$ rectangular frequency profile (red) also at its optimal point with $\tilde{n} = 1000$. The solid lines are fully coherent photons with no squeezing, and the dashed lines have an added squeezing of 10 dB. (Other parameters: $N = 200$ measurements, $r_A = 6.37 \times 10^6$m, $r_B = 42.0 \times 10^6$ m, $\sigma = 2000$, $\omega_0 = 700$ THz and hence $\delta = 6.0 \times 10^{-10}$)

4.6.4 Measurement basis of r_s

In our derivation, the Bures distance definition of the QFI assumes a Gaussian measurement basis. To determine the measurement basis, we refer back to the definition of the QFI used by Ref [11]. The eigenspace of $\hat{\Lambda}(\Theta)$ represents the optimal measurement for which the Fisher information is maximised. We note that the measurement strategy in Ref [17] takes this into account and a one-step adaptive strategy is proposed. In the first step, one makes a fraction of the total measurements N^{ξ} where $1/2 < \xi < 1$ and provides an estimate for the parameter Θ_0. Consequently, the eigenspace $\hat{\Lambda}(\Theta_0)$ can be built from the knowledge of Θ_0 and used to make a better estimate on the remaining measurements.

In Ref [11], it has been proven that the optimal measurement for the beamsplitter parameter using a pure Gaussian probe state is of the form $D(\alpha)S(r)S^{\dagger}(\eta)D(\beta)\left|n\right\rangle$. Here, $D(\alpha) = \exp(\alpha a^{\dagger} - \alpha^* a)$ is the displacement operator and $S(r) = \exp(\frac{1}{2}r^2 a^{\dagger 2} - \frac{1}{2}r^{*2}a^2)$ is the squeezing operator. The coherent amplitude β and squeezing parameter η depend on the final evolved state. The measurement bases for the beamsplitter parameter using a lossy probe state are Gaussian operations and photon counting [11].

4.7 Conclusion

We have studied the optimal estimation of the beamsplitter parameter using a Gaussian quantum probe that is mixed due to loss. We determined the relevant quantum Fisher informations using the definition of the Bures distance and an expression for the fidelity in terms of the quadrature variances. Using this convenient expression, we have considered a squeezed coherent probe state prepared by Alice. We have optimized the QFI with respect to the squeezing fraction and found that for very lossy probe states or low beamsplitter transmission, coherent states are more favourable. However, for low loss and high beamsplitter transmission, squeezing the photons is more advantageous. We have applied these results to a situation where loss is inevitable. In particular we have studied the use of a lossy probe state to estimate the Schwarzschild radius r_s of Earth. We have shown that the frequency profile of the modes sent by Alice is important. By identifying the optimal point that Bob can choose to achieve the best precision, we determined that an approximate rectangular frequency profile achieves error bounds an order of magnitude better than a Gaussian. We also considered more realistic scenarios in which the transmission coefficient depends on the distance from the source and found that approximate rectangular mode shapes are better overall.

The current analysis is restricted to Gaussian states. Other non-classical probe states such as NOON and entangled coherent states (ECS) may enhance the precision even further. Also, the current analysis assumes a specific protocol for estimating r_s. A comparison with other strategies would be interesting.

Acknowledgements

We would like to thank Daiqin Su and Antony Lee for useful discussions. This research was supported in part by the Australian Research Council Centre of Excellence for Quantum Computation and Communication Technology.

Bibliography

[1] *Estimating space-time parameters with a quantum probe in a lossy environment*, S. P. Kish, T. C. Ralph, Phys. Rev. D **93**, 105013 (2016).

[2] *Advances in Quantum Metrology*, V. Giovanetti, S. L. Lloyd, and L. Maccone, Nat. Photonics **5**, 222 (2011).

[3] D. F. Walls, G. J. Milburn, *Quantum Optics*, Springer-Verlag (1995).

[4] *First Long-Term Application of Squeezed States of Light in a Gravitational-Wave Observatory*, H. Grote, K. Danzmann, K.L. Dooley, R. Schnabel, J. Slutsky, H. Vahlbruch, Phys. Rev. Lett. **110**, 181101 (2013) .

[5] *The Space Atom Interferometer project: status and prospects*, F. Sorrentino, K. Bongs, P. Bouyer, L. Cacciapuoti, M. D. Angelis, H. Dittus, W. Ertmer, J. Hartwig, M. Hauth, S. Herrmann et al., J. Phys. Conf. Ser. **327**, 012050 (2011).

[6] N. D. Birrell and P. C. W. Davies, Quantum Fields in Curved Space (Cambridge University Press, Cambridge, 1982).

[7] *Quantum Estimation of Parameters of Classical Spacetimes*, T. G. Downes, J. R. van Meter, E. Knill, G. J. Milburn, C. M. Caves, Phys. Rev. D. **96** 105004 (2016).

[8] *Quantum metrology for relativistic quantum fields*, M. Ahmadi, D. E. Bruschi, and I. Fuentes, Phys. Rev. D **89**, 065028 (2014).

[9] *Relativistic Quantum Metrology: Exploiting relativity to improve quantum measurement technologies* , M. Ahmadi, D. E. Bruschi, C. Sabin, G. Adesso, and I. Fuentes, Sci. Rep. **4**, 4996 (2014).

[10] *Quantum estimation of the Schwarzschild spacetime parameters of the Earth*, Edward Bruschi, Animesh Datta, Rupert Ursin, Timothy C. Ralph and Ivette Fuentes, Phys Rev D, **90**, 124001 (2014).

[11] *Optimal Quantum Estimation of Loss in Bosonic Channels*, A. Monras and M. G. A. Paris, Phys. Rev. Lett. **98**, 160401 (2007).

[12] *Geometry of Quantum States: An Introduction to Quantum Entanglement*, K. Życzkowski, I. Bengtsson, Cambridge University Press May (2006).

[13] *Quantum and classical fidelities for Gaussian states*, H. Jeong, T.C. Ralph, W.P. Bowen, J. Opt. Soc. Am. B **24**, 355-362 (2007)

[14] *Bures and statistical distance for squeezed thermal states*, J. Twamley, J. Phys. A **29**, 3723 (1996).

[15] *Bures fidelity of displaced squeezed thermal states*, X.- B. Wang, C. H. Oh, and L. C. Kwek, Phys. Rev. A **58**, 4186 (1998).

[16] H. Cramér, *Mathematical methods of statistics*, Princeton University Press (1946).

[17] *Optimal phase measurements with pure Gaussian states*, A. Monras, Phys. Rev. A **73**, 033821 (2006).

[18] *State estimation for large ensembles*, R. Gill and S. Massar, Phys. Rev. A **61**, 042312 (2000).

[19] *Achieving the Heisenberg limit in quantum metrology using quantum error correction*, S. Zhou, M. Zhang, J. Preskill, L. Jiang, Nat. Com. **9**, Article number: 78 (2018).

[20] *Space-QUEST: Experiments with quantum entanglement in space*, Ursin, R. et al., Paper presented at 59th International Astronautical Congress, Glasgow, United Kingdom, 2008. IAC Proc. A2.1.3 (2008).

[21] *The Space Optical Clocks Project: Development of high-performance transportable and breadboard optical clocks and advanced subsystems*, Schiller, S. et al. e-print arXiv:1206.3765 [quant-ph] (2012).

[22] *Spacetime effects on satellite-based quantum communications*, D. E. Bruschi, T. C. Ralph, I. Fuentes, T. Jennewein, and M. Razavi, Phys. Rev. D **90**, 045041 (2014).

[23] C. W. Misner, K. S. Thorne, and J. A. Wheeler, Gravitation (W. H. Freeman and Company, San Francisco, 1973).

[24] R. M. Wald, General Relativity (The University of Chicago Press, Chicago, 1984).

[25] *Quantum parameter estimation using multi-mode Gaussian states*, Dominik Šafránek, Antony R. Lee, Ivette Fuentes, New J. Phys. **17** (2015).

[26] *Spectral structure and decompositions of optical states*, P. P. Rohde, W. Mauerer, and C. Silberhorn, New Journal of Physics **9**, 91 (2007).

[27] U. Leonhardt, Measuring the Quantum State of Light, Cambridge Studies in Modern Optics (Cambridge University Press, Cambridge, 2005).

[28] *Scalar, spinor, and photon fields under relativistic cavity motion*, N. Friis, A. R. Lee, and J. Louko, Phys. Rev. D **88**, 064028 (2013).

[29] *A quantum pulse gate based on spectrally engineered sum frequency generation*, A. Eckstein, B. Brecht, and C. Silberhorn, Opt. Express **19**, 13770 (2011).

[30] *Time evolution techniques for detectors in relativistic quantum information*, D. E. Bruschi, A. R. Lee, and I. Fuentes, Journal of Physics A: Mathematical and Theoretical **46**, 165303 (2013).

[31] *Optimal photons for quantum-information processing*, Peter P. Rohde, Timothy C. Ralph, Michael A. Nielsen, Phys. Rev. A **72**, 052332 (2005).

[32] *Fast optical source for quantum key distribution based on semiconductor optical amplifiers*, M. Jofre, A. Gardelein, G. Anzolin, W. Amaya, J. Capmany, R. Ursin, L. Penate, D. Lopez, J. L. S. Juan, J. A. Carrasco, et al., Opt. Express **19**, 3825 (2011).

[33] *Quantum key distribution and 1 Gbps data encryption over a single fibre*, P. Eraerds, N. Walenta, M. Legre, N. Gisin, and H. Zbinden, New Journal of Physics **12**, 063027 (2010).

[34] *Enhanced sensitivity of the LIGO gravitational wave detector by using squeezed states of light*, J. Aasi, J. Abadie, et al. Nat. Photon. **7**, 613-619 (2013).

[35] *Detection of 15 dB Squeezed States of Light and their Application for the Absolute Calibration of Photoelectric Quantum Efficiency*, H. Vahlbruch, M. Mehmet, K. Danzmann, and R. Schnabel, Phys. Rev. Lett. **117**, 110801 (2016).

[36] Hans-A. Bachor., Timothy C. Ralph, A Guide To Experiments in Quantum Optics, ISBN 978-3-527-40393-6 (2004).

[37] *Quantum connectivity of space-time and gravitationally induced decorrelation of entanglement*, T.C. Ralph, G.J. Milburn, and T. Downes, Physical Review A **79**, 022121 (2009).

4.8 Appendix A: Mode Splitter

Consider that we have an input mode that can be written:

$$a' = \sqrt{\epsilon}\ \ a + \sqrt{1-\epsilon}\ \ a'' \tag{4.45}$$

For our purposes the mode a' can be considered the mode that Alice sent, as it appears when it reaches Bob, whilst a is the mode that Bob expects. The mode a'' is the unmatched part which has the property $[a, a''^{\dagger}] = 0$. Now Bob applies a mode sensitive beamsplitter described by the unitary:

$$U = \exp i\theta(ab^{\dagger} + ba^{\dagger}) \tag{4.46}$$

This looks like a normal beamsplitter but it is not because it only acts specifically on the modes a and b (where the vacuum mode entering the other beamsplitter port can be assumed to be in the mode b without loss of generality). The transfer functions for the modes through the beamsplitter can be written, for the transmitted beam:

$$a'_T = \sqrt{\epsilon}\,(\sqrt{\eta}\ \ a + \sqrt{1-\eta}\ \ b) + \sqrt{1-\epsilon}\ \ a'' \tag{4.47}$$

where $\sqrt{\eta}\ = \cos\theta$. For the reflected beam:

$$\begin{aligned} a'_R &= \sqrt{1-\eta}\ \ a - \sqrt{\eta}\ \ b \\ &= \sqrt{1-\eta}\,(\sqrt{\epsilon}\ \ a' + \sqrt{1-\epsilon}\ \ v') - \sqrt{\eta}\ \ b \end{aligned} \tag{4.48}$$

where in the second line we have introduced a vacuum mode defined as $v' = \sqrt{1-\epsilon}\quad a - \sqrt{\epsilon}\quad a''$. Notice if we set $\theta = \pi/2$ and hence $\eta = 0$ we get the transformation we desire, i.e. $a'_R = \sqrt{\epsilon}\ \ a' + \sqrt{1-\epsilon}\ \ v'$ where $\sqrt{\epsilon}\ = [a, a'^{\dagger}]$.

One way to implement the mode-sensitive beamsplitter of Eq. (4.4) is described in Ref [29].

The following publication has been incorporated as Chapter 5.

[1] **S. P. Kish**, T. C. Ralph, *Quantum limited measurement of space-time curvature with scaling beyond the conventional Heisenberg limit*, Phys. Rev. A 96, 041801(R) (2017).

S. P. Kish has a 80% weighting and T. C. Ralph a 20% weighting of contribution to the paper *Quantum limited measurement of space-time curvature with scaling beyond the conventional Heisenberg limit*. We equally did the results analysis and interpretation. I did most of the theoretical derivations and numerical calculations. I have done the majority of writing and preparation of figures. My supervisor Timothy C. Ralph had the initial idea, guided the project in the right direction and contributed to the proofreading.

Chapter 5

Quantum limited measurement of space-time curvature with scaling beyond the conventional Heisenberg limit

In the previous chapter we considered non-classical squeezed states, which in some cases, enhanced the precision of estimating the Schwarzschild radius. In the following chapter, we propose using a nonlinear interferometer to enhance the sensitivity of a measurement apparatus to changes of the parameter r_s. The increased sensitivity will reduce the size of current optical interferometers and potentially make them practical for small scale probing of the gravitational field. We study the problem of estimating the phase shift due to the general relativistic time dilation in the interference of photons using a nonlinear Mach-Zehnder interferometer setup. By introducing two nonlinear Kerr materials, one in the bottom and one in the top arm, we can measure the nonlinear phase ϕ_{NL} produced by the space-time curvature and achieve a scaling of the standard deviation with photon number (N) of $1/N^{\beta}$ where $\beta > 1$, which exceeds the conventional Heisenberg limit of a linear interferometer ($1/N$). The nonlinear phase shift is an effect that is amplified by the intensity of the probe field. In a regime of high photon number, this effect can dominate over the linear phase shift.

5.1 Introduction

Metrology can be seen as an important application driving technological advancement. The ability to estimate parameters of physical systems is restricted by quantum mechanics. Quantum metrology studies how the fundamental bounds on the resolution of such estimates depend on resources such as energy [2]. It is hoped that such studies will lead to new techniques allowing the development of measurement devices of unprecedented precision.

For example, the use of a laser probe to measure a phase-shift, θ, is fundamentally limited by the quantum noise of the probe coherent state. The standard deviation of the estimate, $\langle\Delta\theta\rangle$, scales with the average photon number of the probe states, N, as $\langle\Delta\theta\rangle \propto 1/\sqrt{N}$. This is known as the standard quantum limit. Very high laser powers are used in gravitational wave interferometers to exploit this scaling [3]. It is well known that a squeezed state probe can do better, leading ideally to a $\langle\Delta\theta\rangle \propto 1/N$ scaling known as the Heisenberg limit [4]. Achieving the Heisenberg limit under practical conditions is extremely demanding.

Recently it has been observed that if there is a strong nonlinear coupling to the probe then energy scalings better than the conventional Heisenberg limit can be achieved [5,6]. These claims have generated some controversy [7,8]. Nevertheless a spin-based experimental system has been demonstrated [9]. In the optical domain an example is that of probe transmission through a Kerr medium where it has been shown that estimation of the nonlinear parameter, χ, can be achieved with a $\langle\Delta\chi\rangle \propto 1/N^{3/2}$ scaling [10]. Whilst this is intriguing, there have been few proposed applications for such an effect [11]. Normally we would be interested in estimating some external parameter – not the strength of the measurement system nonlinearity itself.

In this chapter we note that, due to time dilation, the effective nonlinearity of a fixed length of a nonlinear medium is a function of the local gravitational field. This is in addition to the linear phase that is also a function of the proper time. We use this effect to construct an interferometric arrangement that allows one to estimate the space-time curvature of the field with a scaling beyond the conventional Heisenberg energy limit of a linear interferometer [12]. Current techniques for measuring gravity such as atom interferometry [13] are limited to the standard quantum limit (SQL). Squeezing and entanglement could enhance the performance of atom interferometers [14–17] but only up to the Heisenberg limit.

Consider light propagating through a Kerr nonlinearity in a gravitational field described by the Schwarzschild metric. We assume that the metric is approximately constant over the length of the medium. The Kerr nonlinearity constant χ is coupled to the proper time τ it takes to interact with the medium, as measured locally [18]. Thus the effective nonlinearity becomes $\chi' = \chi\tau$. This essentially means that the effective nonlinearity depends on the curvature of space-time. For a nonlinearity of length L, the light propagation time in the medium as measured by the observer at radius $r = r_0$, relative to a reference observer situated at a different radius, is the proper time $\tau \approx (1 - \frac{Kr_s}{2r_0})\frac{L}{c}$ where $r_s = \frac{2GM}{c^2}$ is the Schwarzschild radius and K is a constant that depends on the position of the reference observer. The local clocks of the two observers are compared to determine the amount of time dilation. We can see that the nonlinear coupling is approximately proportional to the Schwarzschild radius. The stronger the curvature r_s, the stronger the space-time coupling to the nonlinearity. In principle we can estimate the spacetime curvature using this dependence.

We model the transmission of a coherent state probe with amplitude α through the medium as the unitary evolution $|\alpha_{NL}(\tau)\rangle = \hat{U}\,|\alpha\rangle$ where $\hat{U} = e^{i\chi\tau\hat{n}(\hat{n}+1)+i\hat{n}kc\tau}$ with $\hat{n}$ the number operator, and k the wave number of the optical mode [19] (see Chapter 2). Hence we find

$$|\alpha_{NL}(\tau)\rangle = e^{-|\alpha|^2/2}\sum_{n=0}^{\infty}\frac{(\alpha e^{i\chi\tau(n+1)+ik\phi(\tau)})^n}{\sqrt{n!}}\,|n\rangle\,. \tag{5.1}$$

We want to determine the ultimate quantum bound for estimating r_s using nonlinear couplings. The bound for the variance of an unbiased estimator $\hat{\tau}$ is determined by the Cramér-Rao inequality [20]. In quantum information theory, for M independent measurements, the inequality is $\langle\Delta\hat{\tau}^2\rangle \geq \frac{1}{M\mathcal{H}(\tau)}$. Where $\mathcal{H}(\tau)$ is the quantum Fisher Information which characterizes the ultimate achievable parameter estimation precision by an optimal quantum measurement [21]. This type of analysis determines the local precision [7] i.e. it assumes we start with a good initial estimate of r_s, which we seek to refine.

We determine the quantum Fisher Information via [22–26]

$$\mathcal{H}(\tau) = \lim_{d\tau\to 0}\frac{8(1-\sqrt{\mathcal{F}(\rho(\tau),\rho(\tau+d\tau))}\,)}{d\tau^2}, \tag{5.2}$$

where $\mathcal{F}(\rho,\sigma) = (Tr(\sqrt{\sqrt{\rho}\,\sigma\sqrt{\rho}}\,))^2$ is the Uhlmann fidelity between two density matrices ρ and σ. We want to determine the QFI for the probe coherent state undergoing the nonlinear evolution (Eq. (5.1)). We disregard orders higher than

2 in $d\tau$ as $d\tau \to 0$ and N_a is finite. Therefore we find the modified fidelity is (see Appendix 5.7 for the calculation of the overlap)

$$\begin{aligned}\mathcal{F} &= |\langle \alpha_{NL}(\tau + d\tau)|\alpha_{NL}(\tau)\rangle|^2 \\ &= 1 - d\tau^2 N_a(2(2 + 5N_a + 2N_a^2)\chi^2 + 4(1 + N_a)\chi\omega + \omega^2)\end{aligned} \tag{5.3}$$

and hence

$$\mathcal{H}(\tau) = 4N_a((\omega + 2(N_a + 1)\chi)^2 + 2N_a\chi^2), \tag{5.4}$$

Where $\omega = kc$ is the frequency and $N_a = |\alpha|^2$ is the photon number of the single mode. As in Chapter 4.4, by noting that $\mathcal{H}(r_s) = (\frac{d\tau}{dr_s})^2\mathcal{H}(\tau)$ and $\frac{d\tau}{dr_s} = \frac{-KL}{2cr_0}$, we find the relative error of the space-time parameter r_s is given by

$$\frac{\langle \Delta r_s \rangle_{opt}}{r_s} \geq \frac{cr_0}{KLr_s\sqrt{N_a((\omega + 2(N_a + 1)\chi)^2 + 2N_a\chi^2)}}. \tag{5.5}$$

For large N_a we see the scaling beyond the conventional Heisenberg limit of the relative error.

We can generalize this result for the case of higher nonlinearities where the light that propagates through nonlinear media experiences self-interaction described by the general Hamiltonian $\hat{H} = \chi(a^\dagger a)^q$. Where $q \geq 2$ and χ is a coupling constant. For large N_a the relative error of the parameter r_s is given by (see Appendix 5.8)

$$\frac{\langle \Delta r_s \rangle_{opt}}{r_s} \geq \frac{cr_0}{KLr_s\sqrt{N_a(q\chi N_a^{q-1} + \omega)^2}}. \tag{5.6}$$

Clearly, the standard deviation of the space-time parameter scales as $\langle \Delta r_s \rangle_{opt} \propto \frac{1}{q\chi N_a^{\frac{2q-1}{2}}}$. Since the time dilation is coupled to the nonlinearity, when $q\chi N_a^{q-1} >> \omega$, it is advantageous to measure the nonlinear phase rather than the linear phase.

5.2 A nonlinear interferometer

We now propose a device for realising the enhanced sensitivity suggested by Eq. (5.5). We consider the Mach-Zehnder interferometer shown diagrammatically in Fig 5.1. We describe the gravitational field via the Schwarzschild metric with line element $ds^2 = g_{\mu\nu}dx^\mu dx^\nu = -f(r)dt^2 + \frac{1}{f(r)}dr^2 + r^2 d\phi^2$ where $f(r) = 1 - \frac{r_s}{r}$. An observer at a fixed radius $r = r_0$ will measure the proper time $\tau = \int ds = \int f(r)dt = \sqrt{f(r_0)}\,t$ where t is the proper time measured by an observer at infinite distance $r = \infty$.

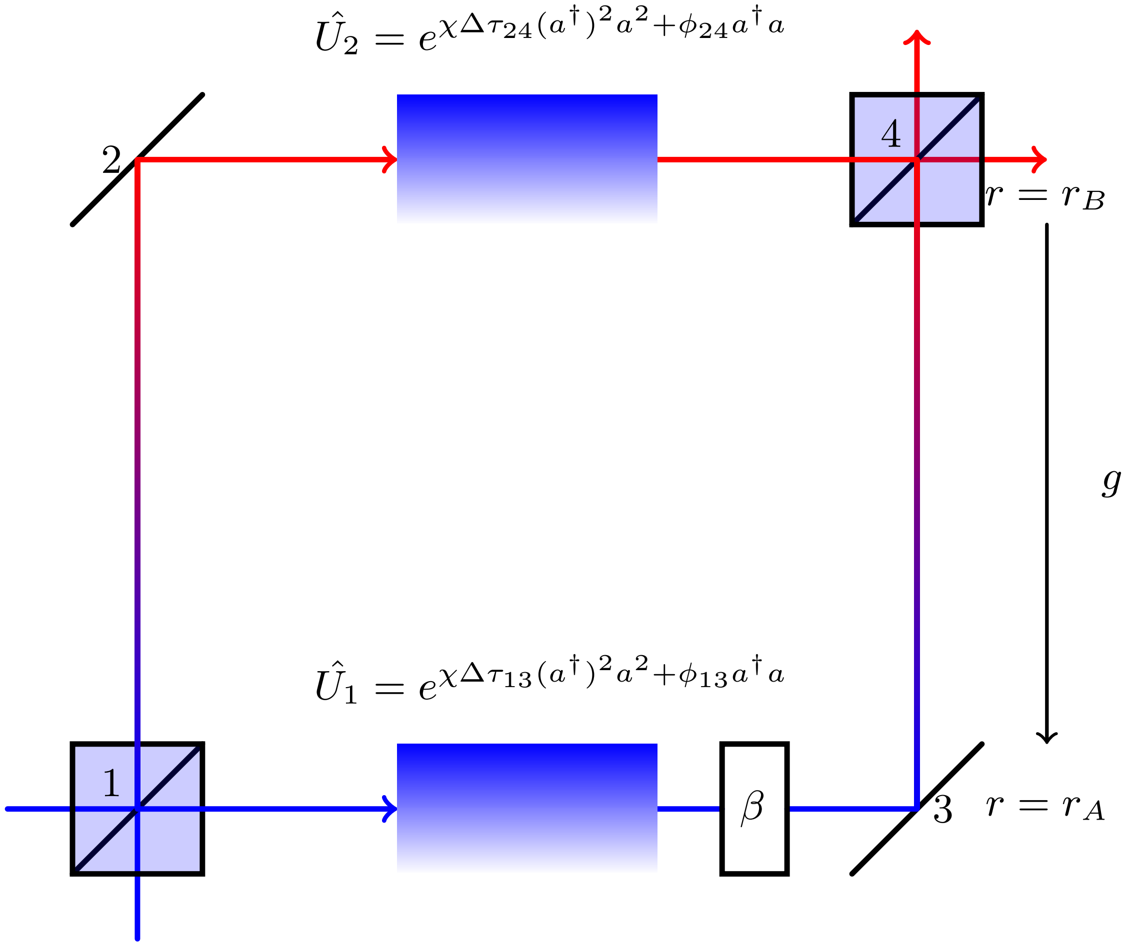

Figure 5.1: Nonlinear interferometer of arm length L in a gravitational field pointing downwards (Note that $r_B > r_A$). Coherent light passes through a 50/50 beamsplitter at 1. The phase from 1 to 3 at $r = r_A$ is set to $\phi_{13} = 0$ and the time interval that light traverses is $\tau_{13} = \frac{L}{c}$. The effect of the gravitational redshift cancels out and no phase shift is accumulated as light traverses vertically. In the top and bottom arms, we have a nonlinear medium with χ coupling. A phase difference due to shorter interaction time with the nonlinearity in the bottom arm is detected after recombining at the second beamsplitter. The time intervals $\Delta\tau_{13}$ and $\Delta\tau_{24}$ contain the Schwarzschild radius r_s. β represents an adjustable linear phase shift.

Without loss of generality we have assumed we are in the equatorial plane with $d\phi$ the usual angular coordinate. Let us first consider evolution of a probe state through the interferometer in Fig 6.1 without the Kerr nonlinearities.

The output modes can be written in terms of the input modes as (see Chapter 2.5.2) [12]

$$\begin{aligned} b_k = \frac{1}{2}(a_k(e^{-ik(\phi_{12}+\phi_{24})} - e^{-ik(\phi_{13}+\phi_{34})}) \\ + v_k(e^{-ik(\phi_{12}+\phi_{24})} + e^{-ik(\phi_{13}+\phi_{34})})), \end{aligned} \tag{5.7}$$

where a_k is prepared in the coherent state and v_k in the vacuum state. The phase shifts in the vertical arms are equal and so cancel out. Therefore we can set $\phi_{12} = \phi_{34} = 0$ without loss of generality. In the bottom horizontal arm, we can choose the time interval so that the phase $\phi_{13} = 0$ and thus $\Delta x_{r_A,13} = c\Delta\tau_{r_A,13}$. We are assuming that $\Delta x_{r_A,13}$ is sufficiently small that we can disregard the curvature of space-time in the horizontal direction. The unknown phase shift is $\phi_{24} = \Delta x_{r_B,24} - \frac{c}{n'}\Delta\tau_{r_B,24}$, where n' is the first order refractive index of the material. In the Schwarzschild metric, the proper time interval at $r = r_A$ is $c\Delta\tau_{r_A} = c\sqrt{1-\frac{r_s}{r_A}}\,\Delta t = \Delta x_{r_A}$, where Δt is the time interval as seen by a far-away observer, and $r_s = \frac{2GM}{c^2}$ is the Schwarzschild radius. We also know that at $r = r_B$ the proper time is

$$\frac{c}{n'}\Delta\tau_{24} = \frac{c}{n'}\sqrt{1-\frac{r_s}{r_B}}\,\Delta t = \frac{\sqrt{1-\frac{r_s}{r_B}}}{n'\sqrt{1-\frac{r_s}{r_A}}}\Delta x_{24}. \tag{5.8}$$

Since the length of the top arm is the same as the bottom arm we set $\Delta x_{13} = \Delta x_{24} = L$, and to simplify the nomenclature we redefine $\tau_{13} = \tau_1$ and $\tau_{24} = \tau_2$, $\tau_2 = \frac{\sqrt{1-\frac{r_s}{r_B}}}{\sqrt{1-\frac{r_s}{r_A}}}\tau_1 \approx (1-\frac{r_s h}{2r_A r_B})\frac{L}{c} = (1-\delta)\frac{L}{c}$, where we have defined $\delta = \frac{r_s h}{2r_A r_B}$. This approximation assumes $r_{A,B} >> r_s$. The *linear* phase simplifies to

$$\phi_{24} = \phi_2 = L - \frac{c}{n'}\tau_2 = (1 - \frac{\sqrt{1-\frac{r_s}{r_B}}}{n'\sqrt{1-\frac{r_s}{r_A}}})L \approx (1 - \frac{1}{n'} + \frac{r_s h}{2r_A r_B n'})L. \tag{5.9}$$

Now we place two nonlinear Kerr media in the top and bottom arms, we expect a phase shift due to the same time dilation, but the Kerr nonlinear medium induces an additional intensity dependent phase shift. The Heisenberg evolution of the annihilation operator for the Kerr nonlinear effect is $a_k(\tau) = e^{i\chi\tau a_k^\dagger a_k}a_k$ [27]. Thus the output mode of the Mach-Zehnder nonlinear interferometer is given by

$$\begin{aligned} b_k =& \frac{1}{2}((e^{-ik\phi_2+i\chi\tau_2 a_k^\dagger a_k} - e^{-ik\phi_1+i\chi\tau_1 a_k^\dagger a_k+i\beta})a_k \\ &+ (e^{-ik\phi_2+i\chi\tau_2 a_k^\dagger a_k} + e^{-ik\phi_1+i\chi\tau_1 a_k^\dagger a_k+i\beta})v_k). \end{aligned} \tag{5.10}$$

We know from Eq. (5.8) and (5.9) the measured proper time τ_2 and the phase ϕ_2. The time intervals τ_1 and τ_2 contain the Schwarzschild radius r_s. We also include an additional adjustable linear phase shift, β.

5.3 Estimating the space-time curvature

To achieve the optimal error bound, we need to make an appropriate measurement at the interferometer output. We choose to measure the quadratures which can be done using balanced homodyne detection (see Chapter 2.7). We assume the coherent amplitude of the probe is large enough to treat as a classical coherent amplitude with added vacuum fluctuations which are only retained to first order. Hence writing $a = \alpha + \delta a$, this allows us to approximate the Kerr evolution in the following way $e^{-ia^\dagger a\chi\tau}a \approx e^{-i|\alpha|^2\chi\tau - i\chi\tau(\alpha^*\delta a + \alpha\delta a^\dagger)}(\alpha+\delta a) \approx e^{-i|\alpha|^2\chi\tau}(1 - i\chi\tau(\alpha^*\delta a + \alpha\delta a^\dagger))(\alpha+\delta a) = e^{-i|\alpha|^2\chi\tau}(1 - i\chi\tau(\alpha^*\delta a + \alpha\delta a^\dagger))\alpha + e^{-i|\alpha|^2\chi\tau}\delta a$.

This approximation is justified provided that $\tau\chi\alpha = \tau\chi\sqrt{N} << 1$. Unlike Ref. [11] which enforce the condition $\tau\chi|\alpha|^2 = \tau\chi N << 1$, this is a looser restriction on the parameters τ, χ, and N. By remaining in the linearized Gaussian regime (where only the mean and variance characterize the state), it is a good approximation to work with single-mode pulses [28, 29]. That is, there is no mode mixing because the coherent amplitudes and the vacuum fluctuations commute. Thus, we continue our analysis in single modes. By applying this approximation to the interferometer mode at the output given by Eq. (5.10), we can write the approximate output quadrature amplitude at angle θ as

$$\begin{aligned}
X_b &= b(\tau)e^{i\theta} + b^\dagger(\tau)e^{-i\theta} \\
&= |\alpha|\cos(\theta+\zeta_2) - |\alpha|\cos(\theta+\zeta_1+\beta) \\
&- \chi|\alpha|^2(\tau_2\sin(\theta+\zeta_2) - \tau_1\sin(\theta+\zeta_1+\beta))X \\
&+ \frac{1}{2}(X_{\theta+\zeta_2} - X_{\theta+\zeta_1+\beta}) \\
&+ \frac{1}{2}(X_{v(\theta+\zeta_2)} + X_{v(\theta+\zeta_1+\beta)}),
\end{aligned} \tag{5.11}$$

where, to simplify the notation, we define $\zeta_1 = k\phi_1 - \tau_1\chi|\alpha|^2$ and $\zeta_2 = k\phi_2 - \tau_2\chi|\alpha|^2$ where $\tau_2 \approx (1-\delta)\tau_1$. We find $\langle X_b\rangle = |\alpha|(\cos(\theta+\zeta_2) - \cos(\theta+\zeta_1+\beta))$. Therefore, the dark port occurs at $\beta_{dark} = \zeta_2 - \zeta_1$. Noting that $\frac{d\tau_2}{dr_s} = -\frac{\delta}{r_s}\frac{L}{c}$ and $\frac{d\tau_1}{dr_s} = 0$ we find the derivative w.r.t. r_s of the quadrature is $\frac{d\langle X_b\rangle}{dr_s} = -|\alpha|(\frac{kc}{n'} + |\alpha|^2\chi)(\frac{d\tau_2}{dr_s}\sin(\theta+\zeta_2) - \frac{d\tau_1}{dr_s}\sin(\theta+\zeta_1+\beta)) = |\alpha|(\frac{kc}{n'} + |\alpha|^2\chi)\frac{\delta L}{r_s c}\sin(\theta+\zeta_2))$. The quadrature variance is given by $\langle(\Delta X_b)^2\rangle = \chi^2|\alpha|^4(\tau_2 \sin(\theta+\zeta_2) - \tau_1 \sin(\theta+\zeta_1+\beta))^2 - \chi|\alpha|^2(\tau_2 \sin(\theta+\zeta_2) - \tau_1 \sin(\theta+\zeta_1+\beta)) \times (\cos(\theta+\zeta_2) - \cos(\theta+\zeta_1+\beta)) + 1$.

The effect of the nonlinearity creates undesirable noise from anti-squeezing in the axis of rotation. However, we can optimize for our choice of β to force the variance to be shot noise. More generally the solution is $\frac{\sin(\theta+\zeta_2)}{\sin(\theta+\zeta_1+\beta)} = \frac{\tau_1}{\tau_2}$ implying that we require $\beta = -\theta - \zeta_1 + \arcsin(\frac{\tau_2}{\tau_1}\sin(\theta+\zeta_2))$. Furthermore, the derivative of the quadrature is $|\alpha|(\frac{kc}{n'} + |\alpha|^2\chi)\frac{\delta L}{r_s c}\sin(\theta+\zeta_1+\beta)(1+\frac{\tau_1}{\tau_2}) = |\alpha|(\frac{kc}{n'} + |\alpha|^2\chi)\frac{\delta L}{r_s c}(\frac{\tau_2}{\tau_1}\sin(\theta+\zeta_2))(1+\frac{\tau_1}{\tau_2})$. The optimal measurement angle is $\theta = \frac{\pi}{2} - \zeta_2$, and $\beta = \zeta_2 - \zeta_1 - \frac{\pi}{2} + \arcsin(\frac{\tau_2}{\tau_1}) \approx \zeta_2 - \zeta_1 - 2\sqrt{\delta}$. Thus the maximum derivative with respect to the Schwarzschild parameter r_s is $|\alpha|(\frac{kc}{n'} + |\alpha|^2\chi)\frac{\delta L}{r_s c}(1+\frac{\tau_2}{\tau_1})$.

Putting all this together we are able to estimate the error bound of the Schwarzschild radius r_s. The variance of the estimator is

$$\begin{aligned}\frac{\langle(\Delta r_s)^2\rangle}{r_s^2} &= \frac{\langle(\Delta X)^2\rangle}{r_s^2(\frac{d\langle X\rangle}{d\tau}\frac{d\tau}{dr_s})^2} \\ &= \frac{\langle\Delta X^2\rangle}{r_s^2|\alpha|^2(\frac{kc}{n'}+|\alpha|^2\chi)^2(\frac{L}{c}\frac{\delta}{r_s})^2(1+\frac{\tau_2}{\tau_1})^2} \\ &\approx \frac{1}{N(\frac{kc}{n'}+N\chi)^2(\frac{L}{c})^2(\frac{r_s h}{r_A r_B})^2(1-\frac{r_s h}{2r_A r_B})^2},\end{aligned} \tag{5.12}$$

where $N = |\alpha|^2$ is the average number of coherent photons injected into the interferometer. Thus the relative error of the Schwarzschild radius r_s of M measurements is

$$\frac{\langle\Delta r_s\rangle}{r_s} \approx \frac{r_A r_B c}{Lhr_s(1-\frac{r_s h}{2r_A r_B})\sqrt{MN(\frac{\omega}{n'}+N\chi)^2}}. \tag{5.13}$$

This can be compared to the Fisher information bound obtained from Eq. (5.5) where the lower bound is exact.

$$\frac{\langle\Delta r_s\rangle_{opt}}{r_s} \geq \frac{r_A r_B c}{Lhr_s\sqrt{MN_a((\omega+2(N_a+1)\chi)^2+2N_a\chi^2)}}. \tag{5.14}$$

Although the nonlinear interferometer does not saturate the Fisher bound it does have the same photon number scaling for large intensities $1/N^{3/2}$, which is beyond the usual Heisenberg limit.

5.4 Beyond-conventional-Heisenberg advantage for measuring space-time curvature

We now wish to know at which point the scaling beyond the conventional Heisenberg limit becomes apparent. In Fig. 5.2, we plot the optimized error bound of the Schwarzschild radius against the number of coherent photons for various nonlinear couplings χ. We have optimized this error with respect to the quadrature measurement angle. We have fixed the interferometer arm lengths to $L = 1$ cm to ensure the condition $|\alpha|\chi\tau << 1$ for all values of $|\alpha|\chi$ in Fig. 5.2.

Furthermore, the height $h = 10$ m with light at a central frequency of $\omega = 100$ THz and $M = 10$ measurements in a second which are reasonable repetition rates [30]. The $\propto \frac{1}{N^{3/2}}$ scaling becomes apparent for increasing number of photons N. As expected, for stronger coupling χ, the scaling beyond the Heisenberg limit becomes dominant for smaller numbers of photons. The quadrature measurement (dashed line) follows but never reaches the ultimate precision bound (Eq. (5.14)) represented by the solid line. We also plot the SNL for interferometer heights $h = 10$ m, 10^2 m and 10^3 m represented by the red solid lines. For a pulse with 10^{18} photons, we'd only need $\chi = 0.1$ for a precision of 10^{-8} which is a 4 order of magnitude improvement over the SQL scaling. State-of-the-art laser-cooled atom interferometry can measure gravity with a resolution of 2×10^{-8} for a $1.3s$ measurement [13]. However, this is limited to the SQL scaling. Future atom interferometers may be able to exploit entanglement resources to approach Heisenberg scaling and improve up to an order of 10^3, as well as using a much longer measurement time [14]. Nonetheless, our optical scheme has the potential to outperform current state-of-the-art gravity measuring devices.

By adding the Kerr nonlinearities we reduce the area of the interferometer needed for a particular precision significantly. More generally, in terms of the dimensionless parameter $\tilde{y} = \frac{N\chi n'}{\omega}$ we find that the effect of the nonlinearity becomes significant when $\tilde{y} \approx 1$, and dominates the scaling when $\tilde{y} \approx 100$. However, we have previously assumed the condition $\chi\tau\alpha = \tilde{y}\omega\frac{L}{c\sqrt{N}} << 1 \approx 0.01$. Therefore, for $N = 10^{15}$, we have to limit the size of the nonlinearity to $L = \frac{0.01c\sqrt{N}}{100\omega} \approx 0.01$ m. Comparing the $h = 10$ m nonlinear noise limit and SQL, we see two or more orders of magnitude improvement equivalent to having a larger linear interferometer $h = 10^3$ m. Thus by introducing the nonlinearity, we can downsize the interferometer size while keeping the precision the same. We note that the anti-squeezing noise for an error in the phase β of $\Delta\beta = 10^{-3}$ radians only changes $\langle \Delta X^2 \rangle$ by 1 dB (see Appendix 5.9) and thus $\Delta r_s/r_s$ only increases an order of magnitude. Our scheme allows us to measure standard error in the phase of 10^{-10} radians in a single shot measurement, thus the added noise is negligible and doesn't affect $\Delta r_s/r_s$.

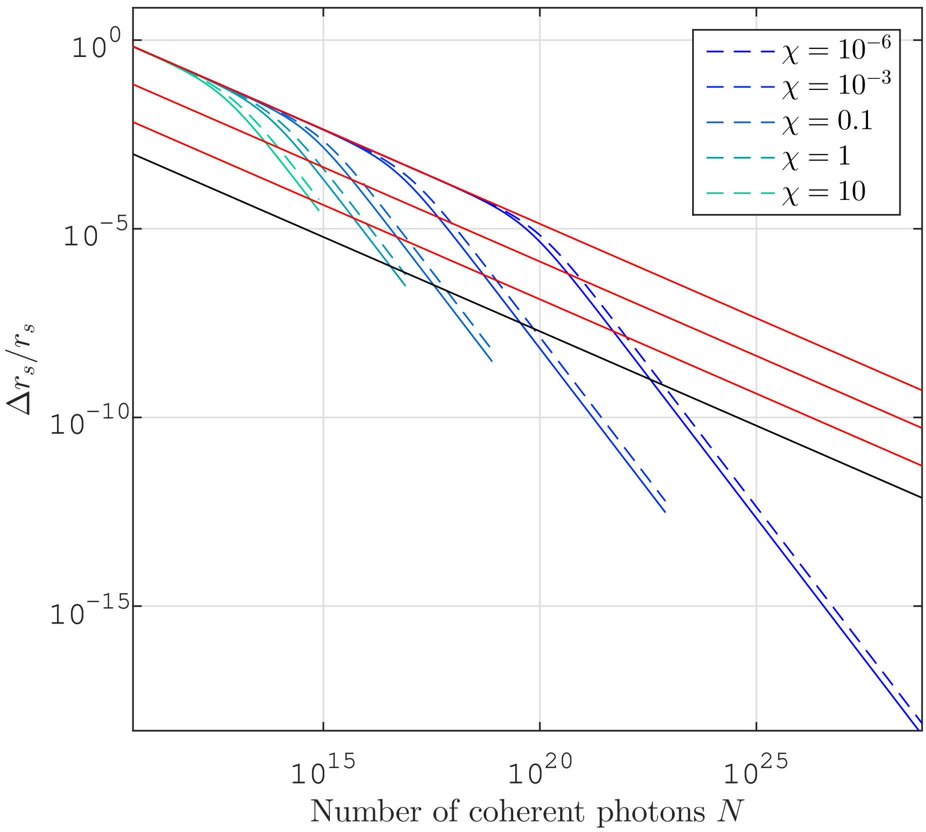

Figure 5.2: Error bound of the Schwarzschild radius plotted against number of coherent photons for various nonlinearity couplings of interferometer arm size $L = 1$ cm and height $h = 10$ m (blue/ green lines). The solid lines represent the exact lower bound for the best possible measurement. The dashed lines are the quadrature measurement error bounds. These lines terminate before the condition $|\alpha|\chi\tau << 1$ is violated (this depends on the values of χ). The solid black line is the case where squeezing of all photons is used to enhance the sensitivity, however small amounts of loss ($\epsilon = 1 - 10^{-6}$) means the scaling is still at the SQL ($h = 10\ m$). From top to bottom, the red solid lines represent the SQL limit for a linear interferometer of heights $h = 10$ m, 10^2 m and 10^3 m. (Other parameters: Number of measurements $M = 10^{10}$, the central frequency $\omega = 100$ THz and the radius $r_A = 6.37 \times 10^6$ m (Earth's radius)).

5.4.1 The effect of loss

- Whilst loss has a highly detrimental effect on the resolution improvements achieved via squeezing, it has a much smaller effect on the nonlinear interferometer. We can model loss introduced due to non-unit detection efficiency via a beamsplitter of transmission ϵ_a after the nonlinearities, and insertion losses on the probe via a beamsplitter of transmission ϵ_b before the nonlinearities. These effects are straightforward to incorporate in the model (see Appendix 5.11) giving the revised error bound

$$\frac{\langle \Delta r_s \rangle}{r_s} = \frac{r_A r_B c}{L h r_s (1 - \frac{r_s h}{2 r_A r_B}) \sqrt{\epsilon_a \epsilon_b N (\frac{\omega}{n'} + \epsilon_b N \chi)^2}}. \tag{5.15}$$

The loss reduces the effective size of the coherent amplitude but does not change the beyond-conventional-Heisenberg scaling. In contrast, a squeezed coherent state will rapidly lose its non-classical properties through a lossy quantum channel. In Fig. 5.2 we have plotted for comparison the performance of an equivalent linear interferometer of the same size ($h = 10$ m) with squeezed light injected [31]. As shown, the presence of a very small amount of loss keeps the scaling at the SQL whilst having virtually no effect on the Schwarzschild bounds of the nonlinear interferometer as seen in Eq. (5.15).

5.5 Experimental feasibility

Surpassing the conventional Heisenberg limit for the parameter χ, rather than τ was recently demonstrated experimentally [32]. The energy scaling was seen in a regime of low photon numbers by canceling the linear phase. Unlike in our approach, effects of anti-squeezing were not considered and a stricter condition of $\chi \tau N << 1$ was imposed, limiting the photon number to $N < 10^8$. In our proposal, the values of the nonlinearity χ and number of photons N at which we get a significant improvement in the precision of r_s are more challenging but may become available in the future. We note that the Kerr nonlinearity constant depends on the pulse duration and the finite time of interaction of the single mode [28]. Our definition of χ describes an effective nonlinearity that is determined from classical theory (see Appendix 5.10). For femto-second pulses in glass fibre the nonlinearity is $\chi \approx 10^{-6}$ which would require over 10^{20} photons per pulse to see the enhancement. In Ref. [33], 30 femto-second pulses at $\omega = 100$ THz frequency with $P = 440$ GW peak power were produced, corresponding to $N = 10^{18}$ photons per pulse, too low to observe the nonlinear phase difference in glass fibre. However, in Ref [2], pico-second pulses in photonic crystal fibres were shown to exhibit a much larger nonlinearity of $\chi \approx 6$ which implies from our results that over $N = 10^{15}$ photons are needed. A further requirement is to ensure that the nonlinear material can withstand intense pulses without optical damage, Kerr saturation or plasma cladding [35–37].

5.6 Conclusion

We have studied the problem of estimating the phase shift due to the general relativistic time dilation in the interference of photons. We have identified that a nonlinear interferometer with Kerr nonlinearities χ in both arms couples to the space-time via a nonlinear phase difference ϕ_{NL}. The quantum error bound of the Schwarzschild radius was found to scale beyond the Heisenberg limit for a coherent probe state input. In principle, nonlinear interactions of order $q \geq 2$ would scale $\propto \frac{1}{N^{q-\frac{1}{2}}}$. We analysed a sub-optimal quadrature measurement that nevertheless shows the same scaling. We found that our nonlinear interferometer is more practical against loss compared to using squeezed coherent states. Finally, we believe that we are within reach of future experiments.

Acknowledgements. This work was supported in part by the Australian Research Council Centre of Excellence for Quantum Computation and Communication Technology (Project No. CE110001027) and financial support by an Australian Government Research Training Program Scholarship.

Bibliography

[1] *Quantum limited measurement of space-time curvature with scaling beyond the conventional Heisenberg limit*, S. P. Kish, T. C. Ralph, Phys. Rev. A **96**, 041801(R) (2017).

[2] *Advances in quantum metrology*, V. Giovanetti, S. Lloyd, and L. Maccone, Nat. Photon. **5**, 222 (2011).

[3] *Observation of Gravitational Waves from a Binary Black Hole Merger*, B. P. Abbott et al., Phys. Rev. Lett. **116**, 061102 (2016).

[4] *Quantum-mechanical noise in an interferometer*, C. M. Caves, Phys. Rev. D **23**, 1693 (1981).

[5] *Breaking the Heisenberg limit with inefficient detectors*, J. Beltrán and A. Luis, Phys. Rev. A **72**, 045801 (2005)

[6] *Generalised limits for single-parameter quantum estimation*, S. Boixo, S. T. Flammia, C. M. Caves, Phys. Rev. Lett., **98**, 090401 (2007).

[7] *Does Nonlinear Metrology Offer Improved Resolution? Answers from Quantum Information Theory*, M. J. W. Hall and H. M. Wiseman, Phys. Rev. X **2**, 041006 (2012).

[8] *General optimality of the Heisenberg limit for quantum metrology*, Marcin Zwierz, Carlos A. Perez-Delgado, Pieter Kok, Phys. Rev. Lett. **105**, 180402 (2010).

[9] *Interaction-based quantum metrology showing scaling beyond the Heisenberg limit*, M. Napolitano, et al., Nature, **471**, 486 (2011).

[10] *Quantum metrology for non-linear phase shifts with entangled coherent states*, Jaewoo Joo, Kimin Park, Hyunseok Jeong, William J. Munro, Kae Nemoto, Timothy P. Spiller, Phys. Rev. A **86**, 043828 (2012).

[11] *Nonlinear Michelson interferometer for improved quantum metrology*, A. Luis, A. Rivas, Phys. Rev. A **92**, 022104 (2015).

[12] *General relativistic effects in quantum interference of photons*, Magdalena Zych, Fabio Costa, Igor Pikovski, Timothy C. Ralph and Caslav Brukner, Class. Quantum Grav. **29** 224010 (2012).

[13] *High-precision gravity measurements using atom interferometry*, A. Peters, K. Y. Chung, S. Chu, Metrologia **38**, 25 (2001).

[14] *Testing General Relativity with Atom Interferometry*, S. Dimopoulos, P. W. Graham, J. M. Hogan, M. A. Kasevich, Phys. Rev. Lett. **98**, 111102 (2007).

[15] *Squeezed-light-enhanced atom interferometry below the standard quantum limit*, S. S. Szigeti, B. Tonekaboni, W. Y. S. Lau, S. N. Hood, and S. A. Haine, Phys. Rev. A **90**, 063630 (2014).

[16] *Squeezing and entanglement in a Bose Einstein condensate*, J. Esteve, C. Gross, A. Weller, S. Giovanazzi, M. K. Oberthaler, Nature **455**, 1216-1219 (2008).

[17] *Nonlinear atom interferometer surpasses classical precision limit*, C. Gross, T. Zibold, E. Nicklas, J. Estve, M. K. Oberthaler, Nature **464**, 1165-1169 (2010).

[18] *Quantum Field Theory*, M. Srednicki, Cambridge University Press pg. 10 (2007).

[19] *Quantum Optics*, D. F. Walls, Gerard J. Milburn, 2nd Edition Springer-Verlag Berlin Heidelberg (2008).

[20] *Mathematical methods of statistics*, H. Cramér, Princeton University Press, (1946).

[21] *Optimal Quantum Estimation of Loss in Bosonic Channels*, A. Monras and M. G. A. Paris, Phys. Rev. Lett. **98**, 160401 (2007).

[22] *Quantum Information: An Introduction*, M. Hayashi, Berlin: Springer (2006).

[23] *Heisenberg scaling in Gaussian quantum metrology*, N. Friis, M. Skotiniotis, I. Fuentes, and W. Dur, Phys. Rev. A **92**, 022106 (2015).

[24] *Quantum parameter estimation using multi-mode Gaussian states* D. Šafránek, A. R. Lee, and I. Fuentes, New J. Phys. **17**, 073016 (2015).

[25] *Statistical distance and the geometry of quantum states*, S. L. Braunstein and C. M. Caves, Phys. Rev. Lett. **72**, 3439 (1994).

[26] *Quantum Metrology. Fisher Information and Entanglement of Non-Gaussian Spin States*, H. Strobel, W. Muessel, D. Linnemann, T. Zibold, D. B. Hume, L. Pezz, A. Smerzi, and M. K. Oberthaler, Science **345**, 424 (2014) .

[27] *Theory of Nonclassical States of Light, Chapter 6: Nonclassical states of light propagating in Kerr media*, pg. 285, V. V. Dodonov, V. I. Man'ko, R. Tanas, Taylor & Francis (2003).

[28] *Quantum propagation in a Kerr medium: lossless, dispersionless fiber*, L. G. Joneckis and J. H. Shapiro, J. Opt. Soc. Am. B **10**, 1102 (1993).

[29] *Number-phase minimum-uncertainty state with reduced number uncertainty in a Kerr nonlinear interferometer*, M. Kitagawa and Y. Yamamoto, Phys. Rev. A **34**, 3974 (1986).

[30] *10-GHz, 1.3-ps erbium fiber laser employing soliton pulse shortening*, T. F. Carruthers, I. N. Duling, Optics Letters **21**, 23:1927-1929 (1996).

[31] *Quantum optical metrology in the lossy SU(2) and SU(1,1) interferometers*, Y. Gao, Phys. Rev. A **94**, 023834 (2016).

[32] *Surpassing the conventional Heisenberg limit using classical resources*, X. Jin, M. Lebrat, L. Zhang, K. Lee, T. Bartley, M. Barbieri, J. Nunn, A. Datta, and I. A. Walmsley, CLEO: QELS Fundamental Science 2013 paper QF2B.2, San Jose, CA, OSA Technical Digest (online) (OSA, Washington, D.C., 2013).

[33] *Multi-millijoule few-cycle mid-infrared pulses through nonlinear self-compression in bulk*, V. Shumakova, P. Malevich, S. Alisauskas, A. Voronin, A. M. Zheltikov, D. Faccio, D. Kartashov, A. Baltuka, and A. Puglys, Nat. Commun. **7**:12877 (2016).

[34] *Observation of optical-fibre Kerr nonlinearity at the single-photon level*, N. Matsuda, R. Shimizu, Y. Mitsumori, H. Kosaka, K. Edamatsu, Nat. Photon. **3**, 95 (2009).

[35] *Saturation of the all-optical Kerr Effect*, C. Bree, A. Demircan, G. Steinmeyer, Phys. Rev. Lett. **106**, 183902 (2011).

[36] *Saturation of the all-optical Kerr effect in solids*, B. Borchers, C. Bree, S. Birkholz, A. Demircan, G. Steinmeyer, Optics Letters **37** 9 (2012).

[37] *Nonlinear Optics (Third Edition)*, Chap 4.7, R. W. Boyd, Elsevier (2008).

5.7 Appendix A: Calculation of coherent state overlap in Eq. (5.3)

We consider the coherent state undergoing the nonlinear evolution $U_{NL} = e^{-i\chi\tau(a^\dagger a)^2}$. To determine the fidelity $\mathcal{F} = |\langle\alpha(\tau)|\alpha(\tau+d\tau)\rangle|^2$ for a small change in the measured parameter τ, we first determine the overlap:

$$\begin{aligned}
&\langle\alpha_{NL}(\tau+d\tau)|\alpha_{NL}(\tau)\rangle = e^{-|\alpha|^2}\sum_{n=0}^{\infty}\frac{(|\alpha|^2 e^{-i\chi d\tau(n+1)+ikcd\tau})^n}{n!}\\
&\approx e^{-|\alpha|^2}\sum_{n=0}^{\infty}\frac{|\alpha|^{2n}e^{inkcd\tau}}{n!}(1-i\chi d\tau(n+1)n\\
&-\frac{\chi^2 d\tau^2(n+1)^2n^2}{2})\\
&= e^{-|\alpha|^2(1-e^{ikcd\tau})}(1-i\alpha^2 e^{i\omega d\tau}(2+\alpha^2 e^{i\omega d\tau})\chi d\tau\\
&-\frac{|\alpha|^2 e^{i\omega d\tau}}{2}(4+14e^{i\omega d\tau}|\alpha|^2+8e^{2i\omega d\tau}|\alpha|^4\\
&+e^{3i\omega d\tau}|\alpha|^6)\chi^2 d\tau^2)
\end{aligned} \tag{5.16}$$

Expanding and only retaining terms up to second order in $d\tau$ gives Eq. 3 in the main text.

5.8 Appendix B: Approximate quantum Fisher Information for q order nonlinearity

We want to determine the Cramér-Rao bound for q order nonlinear interaction with Hamiltonian $H = \chi(a^\dagger a)^q$. We can approximate the unitary evolution using $a \approx |\alpha| + \delta a$ for very large coherent amplitude. Thus, the evolved coherent state becomes $e^{i\chi\tau(a^\dagger a)^q}|\alpha\rangle \approx e^{i\chi\tau|\alpha|^{2q}(1+\frac{q\delta a^\dagger}{|\alpha|})(1+\frac{q\delta a}{|\alpha|})}|\alpha\rangle \approx e^{i\chi\tau|\alpha|^{2q}}e^{i\chi\tau q|\alpha|^{2q-1}(\delta a^\dagger+\delta a)}e^{|\alpha|(\delta a^\dagger-\delta a)}|0\rangle \approx e^{i\chi\tau|\alpha|^{2q}}|\alpha(1+iq\chi\tau|\alpha|^{2(q-1)})\rangle$. In general, for $q \geq 2$,

$$\begin{aligned}
&\langle\alpha_{NL}(\tau+d\tau)|\alpha_{NL}(\tau)\rangle\\
&= e^{\frac{|\alpha|^2}{2}|(1-iq\chi(\tau+d\tau)|\alpha|^{2(q-1)})e^{ikc(\tau+d\tau)}-(1-iq\chi d\tau|\alpha|^{2(q-1)})e^{ikc\tau}|^2}\\
&\approx e^{-\frac{|\alpha|^2}{2}(q\chi|\alpha|^{2(q-1)}d\tau+kcd\tau)^2}
\end{aligned} \tag{5.17}$$

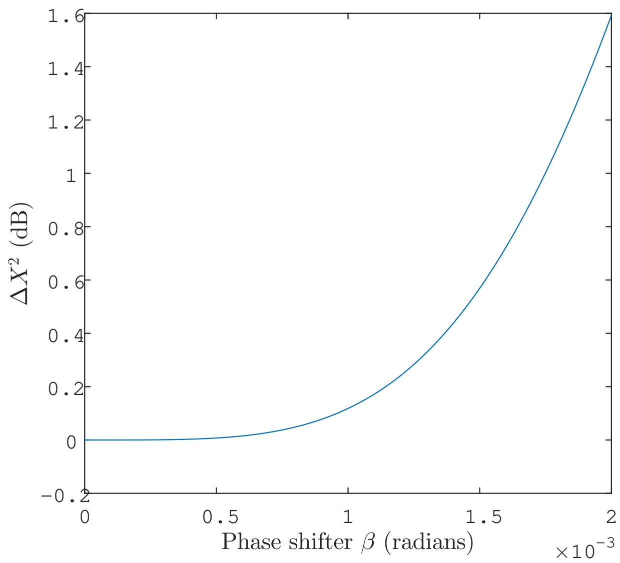

Figure 5.3: Quadrature noise at the chosen measurement angle $\theta = \frac{\pi}{2} - \zeta_2$. For approximately $\Delta\beta = \beta_a - \beta = 1.5 \times 10^{-3}$ corresponding to a large systematic phase error, we only have an increase of 1 dB of noise.

Therefore, the fidelity is

$$\mathcal{F} = 1 - N(q\chi N^{q-1} + kc)^2 d\tau^2 \tag{5.18}$$

And the quantum Fisher information is:

$$\mathcal{H}(\tau) = 4N(q\chi N^{q-1} + kc)^2 \tag{5.19}$$

5.9 Appendix C: Quadrature noise

We consider the effect of how a systematic error in the choice of the phase β can change the amount of noise. For the parameters $\chi = 0.1$ and $N = |\alpha|^2 = 10^{17}$, we choose $\theta + \zeta_2 = \frac{\pi}{2}$ and β is the independent variable. As it turns out, for a small off-set from the optimum point of 10^{-3} radians in this β phase, less than 1 dB of noise is added (see Fig. 5.3). This doesn't seem to be a major issue since we predict a $\Delta r_s/r_s = 10^{-3}$ and thus we can detect an absolute change of 10^{-10} radians in the phase for a single shot measurement. Therefore, a large systematic error doesn't add significant noise to destroy the beyond-conventional-Heisenberg scaling.

5.10 Appendix D: Experimental feasibility

In Fig. 5.4, we present the relative Schwarzschild error bound plotted against the dimensionless parameter $\tilde{y} = \frac{N\chi n'}{\omega}$. Thus, we can rewrite the error bounds as:

$$\frac{\langle \Delta r_s \rangle}{r_s} = \frac{r_A r_B c n'}{Lhr_s\omega(1 - \frac{r_s h}{2r_A r_B})\sqrt{MN(1+\tilde{y})^2}} \tag{5.20}$$

And

$$\frac{\langle \Delta r_s \rangle_{opt}}{r_s} \geq \frac{r_A r_B c n'}{2Lhr_s\omega\sqrt{MN_a((1+2\tilde{y}+2\chi)^2 + 2\tilde{y}\chi)}} \tag{5.21}$$

Where M is the number of single shot measurements. From these expressions, we expect that the turning point at which the nonlinearity becomes significant is approximately when $\tilde{y} \approx 10$. As seen in Fig. 5.4, for a fixed number of photons N and central frequency ω, there is approximately an order of magnitude improvement over a SNL linear interferometer. A conservative estimate of χ for $N = 10^{15}$, 10^{17}, 10^{20} respectively is $\chi = \frac{\tilde{y}\omega}{N} = 1$, 10^{-2} and 10^{-5}. Let's consider the case of $\chi = 10^{-5}$ for which the number of photons per $\Delta t = 30\ fs$ pulse duration is $N = 10^{20}$ with $M = 10^{10}$ number of measurements would correspond to a peak power of $P = \frac{N\hbar\omega}{\Delta t} \approx 4 \times 10^{13}$ W=40 TW (Average power $\tilde{P} = 10$ GW). On the other hand, for a stronger linearity of $\chi = 1$, the peak power required to see the enhancement with $N = 10^{15}$ photons per pulse would reduce to $P = 400$ MW and an average power of $\tilde{P} = 100$ kW. We note similarities in these values with Ref. [1].

The definition of the nonlinearity constant χ' in Ref. [1] is slightly different from our definition. Namely, χ' represents the phase shift per unit photon. It is defined as:

$$\chi' = \frac{\tilde{n}}{n_0}\frac{\hbar\omega}{A\Delta t} \tag{5.22}$$

Where $\tilde{n}$ is the second order refractive index from the expansion $n = n_0 + \tilde{n}I$, A is the area of the pulse, and Δt is its duration. Thus, the nonlinear phase shift per photon can be increased by reducing the area and the pulse duration. It follows that the phase shift is given by $\phi'_{NL} = \frac{n_0\omega L}{c}\frac{\chi'}{2}N$. Comparing with our phase shift $\phi_{NL} = \frac{L}{c}\chi N$, the relation between our nonlinear coefficient and that in Ref [1] is $\chi = \frac{n_0}{2}\omega\chi'$.

The values of the nonlinearities quoted in the main text are based on converting the given formula of the phase $\phi_{NL} = |\alpha|^2\chi\tau$ from the values given. For example,

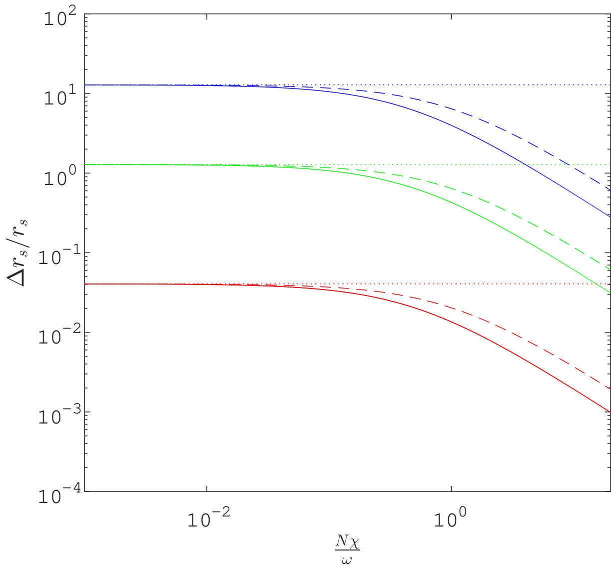

Figure 5.4: Error bound of the Schwarzschild radius plotted against the dimensionless quantity $\frac{N\chi}{\omega}$ for various N and fixed length $L = 1000$ m and $h = 1$ m. From top to bottom, each colour represents $N = 10^{15}$, $N = 10^{17}$ and $N = 10^{20}$. The solid lines represent the theoretical quantum error bound. The dashed represent the quadrature measurement. The dotted lines represent the shot noise limit for a linear interferometer. (Other parameters are $M = 10^{10}$)

a nonlinear phase shift of $10^{-8} - 10^{-7}$ with the given fibre length of $L = 4.5$ m in Ref. [2] for a single photon correponds to $\chi = 1$ to $\chi = 6$. The same calculation was done for the optical fibre.

5.11 Appendix E: Including loss

The effect of loss on the nonlinear interferometer - Whilst loss has a highly detrimental effect on the resolution improvements achieved via squeezing, it has a much smaller effect on the nonlinear interferometer. We can model loss introduced due to non-unit detection efficiency via a beamsplitter of transmission ϵ_a after the nonlinearities, and insertion losses on the probe via a beamsplitter of transmission ϵ_b before the nonlinearities. These effects are straightforward to incorporate in the model giving the revised error bound in Eq. (5.15).

Loss after the nonlinearity leads to $e^{-ia^\dagger a\chi\tau}a \to e^{-ia^\dagger a\chi\tau}\sqrt{\epsilon_a}\, a + \sqrt{1-\epsilon_a}\, d$ and after the beamsplitter becomes:

$$\begin{aligned}
X_b &= b(\tau)e^{i\theta} + b^\dagger(\tau)e^{-i\theta} \\
&= \sqrt{\epsilon_a}\,|\alpha|\cos(\theta+\zeta_2) - \sqrt{\epsilon_a}\,|\alpha|\cos(\theta+\zeta_1+\beta) \\
&- \chi|\alpha|^2(\tau_2\sin(\theta+\zeta_2) - \tau_1\sin(\theta+\zeta_1+\beta))\sqrt{\epsilon_a}\,\delta X_a \\
&+ \frac{\sqrt{\epsilon}}{2}(\delta X_{a(\theta+\zeta_2)} - \delta X_{a(\theta+\zeta_1+\beta)}) \\
&+ \frac{\sqrt{1-\epsilon}}{\sqrt{2}}(\delta X_{d(\theta+\zeta_2)} - \delta X_{d'(\theta+\zeta_1+\beta)}) \\
&+ \frac{\sqrt{\epsilon}}{2}(X_{v(\theta+\zeta_2)} + X_{v(\theta+\zeta_1+\beta)})
\end{aligned} \tag{5.23}$$

And the variance is:

$$\begin{aligned}
\langle\Delta X_b^2\rangle &= \epsilon_a\chi^2|\alpha|^4(\tau_2\sin(\theta+\zeta_2) - \tau_1\sin(\theta+\zeta_1+\beta))^2 \\
&- \epsilon_a\chi|\alpha|^2(\tau_2\sin(\theta+\zeta_2) - \tau_1\sin(\theta+\zeta_1+\beta)) \\
&\times(\cos(\theta+\zeta_2) - \cos(\theta+\zeta_1+\beta)) + 1
\end{aligned} \tag{5.24}$$

For the optimal angle, the variance reduces also to shot noise $\langle\Delta X^2\rangle = 1$. Loss before the nonlinearities simply reduces the input photon number by the factor ϵ_b. Therefore, the error bound for the combined case of having loss before and after the nonlinearities is:

$$\frac{\langle\Delta r_s\rangle}{r_s} = \frac{r_A r_B c}{Lhr_s(1-\frac{r_s h}{2r_A r_B})\sqrt{\epsilon_a\epsilon_b N(\frac{\omega}{n'} + \epsilon_b N\chi)^2}} \tag{5.25}$$

The loss reduces the effective size of the coherent amplitude but does not change the super-Heisenberg scaling. In contrast, a squeezed coherent state will lose its non-classical properties through a lossy quantum channel. In Fig. 5.2 of the main text we have plotted for comparison the performance of an equivalent linear interferometer with squeezed light injected [3]. As shown, the presence of a very small amount of loss destroys the advantage of the squeezing whilst having virtually no effect on the nonlinear interferometer. The ultimate limit for a lossy interferometer with squeezed coherent probe states is [3]:

$$\frac{\langle\Delta r_s\rangle}{r_s} \geq \frac{r_A r_B c n'}{2Lhr_s\omega\sqrt{\frac{\epsilon N_c}{1-\epsilon+\epsilon e^{-2r}} + \epsilon N_s}} \tag{5.26}$$

Where N_c and N_s is the number of coherent and squeezed photons, respectively. We assume the squeezing parameter r is positive and very large. Consequently, for significant loss $\epsilon << 1$, the Heisenberg scaling of $\propto \frac{1}{N}$ is lost for the optimal number of squeezed photons $N_s = N_c$ and reduces to the SNL. Loss on the order of

$\epsilon \approx 1 - \frac{1}{N_\chi}$ where N_χ is the turning point of the scaling for the respective value of the nonlinearity is enough to destroy the Heisenberg scaling as seen in Fig. 5.2 of the main text. On the other hand, our nonlinear interferometer setup requires only a $\frac{1}{\epsilon}$ increase in the input number of coherent photons to compensate for the loss.

Bibliography

[1] *Nonlinear Michelson interferometer for improved quantum metrology*, A. Luis, A. Rivas, Phys. Rev. A **92**, 022104 (2015)

[2] *Observation of optical-fibre Kerr nonlinearity at the single-photon level*, N. Matsuda, R. Shimizu, Y. Mitsumori, H. Kosaka, K. Edamatsu, Nat. Photon. **3**, 95 (2009)

[3] *Quantum optical metrology in the lossy SU(2) and SU(1,1) interferometers*, Y. Gao, Phys. Rev. A **94**, 023834 (2016)

The following publication has been incorporated as Chapter 6.

[1] **S. P. Kish**, T. C. Ralph, *Quantum metrology in the Kerr metric*, Phys. Rev. D 99, 124015 (2019).

S. P. Kish has a 80% weighting and T. C. Ralph a 20% weighting of contribution to the paper *Quantum Metrology in the Kerr Metric*. We equally did the results analysis and interpretation. I did most of the theoretical derivations and numerical calculations. I have done the majority of writing and preparation of figures. My supervisor Timothy C. Ralph had the initial idea, guided the project in the right direction and contributed to the proofreading.

Chapter 6

Quantum metrology in the Kerr metric

The aim of this thesis is to consider the measurement of space-time curvature using quantum metrology tools. In this chapter, we consider the Kerr metric around a rotating massive body and consider the quantum limits for precision of estimating the frame dragging effect characteristic of this metric. A surprising feature of the Kerr metric is the anisotropy of the speed of light. The angular momentum of a rotating massive object causes co- and counter-propagating light paths to move at faster and slower velocities, respectively as determined by a far-away clock. Based on this effect we derive ultimate quantum limits for the measurement of the Kerr rotation parameter a using a interferometric setup. As a possible implementation, we propose a Mach-Zehnder interferometer to measure the “one-way height differential” time effect. We isolate the effect by calibrating to a dark port and rotating the interferometer such that only the direction dependent Kerr-metric induced phase term remains. We transform to the Zero Angular Momentum Observer (ZAMO) flat metric where the observers see $c = 1$. We use this metric and the Lorentz transformations to calculate the same Kerr phase shift. We then consider non-stationary observers moving with a planet’s rotation, and find a method for cancelling the additional phase from the classical relative motion, thus leaving only the curvature induced phase.

6.1 Introduction

Quantum metrology is the study of the lower limits for the estimation of physical parameters [2]. Techniques in quantum metrology can assist in developing devices to measure the fundamental interplay between quantum mechanics and general relativity at state-of-the-art precision. A prime example is the detection of gravitational waves from black-hole mergers by LIGO [3].

Recently there have been investigations of how we can exploit quantum resources to measure space-time parameters such as the Schwarzschild radius r_s and the Kerr parameter a in the rotating Kerr metric [4–7]. Quantum communications were shown to be affected by the rotation of Earth [8]. However, more fundamental effects in general relativity induced by the Kerr metric were not analysed. One interesting feature of the Kerr metric is the anisotropy of the velocity of light (null geodesics). The rotating massive object causes co- and counter- propagating light to move at faster and slower velocities, respectively.

In this chapter, we note that there is a phase shift of co-moving light beams at different radial positions in the Kerr metric. We use a Mach-Zehnder (MZ) interferometer to probe this phase. We isolate the effect by calibrating to a dark port and rotating the interferometer and due to the anisotropy of c, only the Kerr phase term remains. From this, we can construct lower bounds for the variance of parameter estimation of the Kerr rotation parameter a using Quantum Information techniques [4, 7, 9].

Locally, we can find a co-rotating frame in which the space-time is locally flat ("the zero angular momentum ring-riders") [10]. We find that the locally measured velocity of light is $c = 1$ as expected in the flat metric. If an observer Alice compares the locally measured time with Bob who is a ring-rider at a different radius, there will be a disagreement of simultaneity of events. We also consider non-stationary observers that are moving in the rotational plane of Earth. As expected, we find an additional phase term from rotation and special relativistic time dilation. We find that this term is dominant compared to the Kerr phase. Finally, we compare the magnitude of the Kerr phase on Earth to that achievable by microwave resonator experiments [11].

This chapter is organized as follows. We first introduce the full Kerr metric in Section 6.2 for a rotating black hole. In Section 6.2.1, we approximate the Kerr metric to first order in angular momentum where the mass quadrupole moment for massive planets or stars is dropped in the weak field limit. In Section 6.2.2, we solve for the null geodesic to determine the velocity of light in the equatorial plane. We find the anisotropy in c. Next in Section 6.2.3, we calculate the "height differential effect" which could be detected by a Mach-Zehnder interferometer above a massive planet.

In Section 6.3, we determine quantum limits of the estimation the Kerr space-time parameter a for the height differential effect. In Section 6.3.1, we focus on the stationary Mach-Zehnder interferometer in the weak field limit and calculate the phase shift. We comment on how we can calibrate to a dark port and rotate the interferometer to isolate the Kerr phase. We compare the magnitude of the Kerr phase with the Schwarzschild phase for Earth parameters. In Section 6.4, we use the co-moving flat metric in which the so-called "ring-rider" measures $c = 1$. In Section 6.5, we demonstrate an alternative calculation using Lorentz transformations between stationary and ring-riders to find the phase detected at the output of the MZ interferometer. We also confirm that the "two-way" velocity of light is $c = 1$ as detected by a Michelson interferometer at rest in the Kerr metric. Furthermore, we consider the motion of non-stationary observers on the rotating planet. In Section 6.6, we consider an extremal black hole and we numerically find the full strong field solution of the Kerr phase. Finally, we conclude by commenting on the feasibility of detecting the light anisotropy.

6.2 Kerr Rotational Metric

The metric describing the space-time of an axially symmetric rotating massive body is given by the Hartle-Thorne metric, which includes the dimensionless mass quadrupole moment q and the angular momentum (mass normalized) j of the massive body [12, 13]. The mass quadrupole moment is $q = kj^2$ where k is a numerical constant that depends on the structure of the massive body. The Kerr metric for a black hole is obtained from the Hartle-Thorne metric by setting $q = -j^2$ and transforming to Boyer-Lindquist coordinates [14, 15].

A rotating black hole tends to drag the space-time with its rotation. The Kerr metric used to describe this space-time includes the Kerr rotation parameter "a" which quantifies the amount of space-time drag. The Kerr line element in Boyer-

Lindquist coordinates (t, r, θ, ϕ) is [10, 12, 17]

$$\begin{aligned} ds^2 = &-(1 - \frac{r_s r}{\Sigma})dt^2 + \frac{\Sigma}{\Delta}dr^2 + \Sigma d\theta^2 \\ &+ (r^2 + a^2 + \frac{r_s r a^2}{\Sigma}\sin^2\theta)\sin^2\theta d\phi^2 - \frac{2r_s r a \sin^2\theta}{\Sigma}d\phi dt, \end{aligned} \tag{6.1}$$

where $\Delta := r^2 - r_s r + a^2$, $\Sigma := r^2 + a^2\cos^2\theta$ and $a = \frac{J}{Mc}$ where J is the angular momentum of the black hole of mass M. Note that the Schwarzschild radius $r_s = \frac{2GM}{c^2} \equiv 2M$ where we work in natural units for which $c = 1$ and $G = 1$. Compared with the Schwarzschild metric, the cross term $dtd\phi$ introduces a coupling between the motion of the black hole and time, which leads to interesting effects.

When $r_s = 0$, the space-time is flat and reduces to $ds^2 = -dt^2 + \frac{1}{1+\frac{a^2}{r^2}}dr^2 + (r^2 + a^2)d\phi^2$. At first glance, this metric doesn't seem flat. However, we have used the oblong sphere coordinates $x = \sqrt{r^2 + a^2}\ \sin\theta\cos\phi$, $y = \sqrt{r^2 + a^2}\ \sin\theta\sin\phi$ and $z = r\cos\theta$.

6.2.1 Approximate Kerr metric for rotating massive bodies

The mass quadrupole moment of a *massive planet* is proportional to the angular momentum squared. Thus, we cannot use the Kerr metric in Eq. (6.1) where the proportionality constant for *black holes* is $k = -1$. However, in the weak field limit $a << r$, we can truncate the Kerr metric to first order in $\frac{a}{r}$. Thus the approximate Kerr metric is given by

$$\begin{aligned} ds^2 = &-(1 - \frac{r_s}{r})dt^2 + (1 - \frac{r_s}{r})^{-1}dr^2 + r^2 d\theta^2 \\ &+ r^2\sin^2\theta d\phi^2 - \frac{2r_s a \sin^2\theta}{r}d\phi dt. \end{aligned} \tag{6.2}$$

This approximate Kerr metric disregards the mass quadrupole moment of the massive body. It is equivalent to the Hartle-Thorne metric with the same first order approximation [16]. When we refer to a massive planet or star, we will use this approximate Kerr metric. We wish next to determine the tangential velocity of light close to the massive object as seen by a far-away observer.

6.2.2 Far-away velocity of light

As was done in the Schwarzschild metric in Chapter 3.4, we can derive the velocity of light as inferred by a far-away observer. In the equatorial plane (where $\theta = \frac{\pi}{2}$), for the null light geodesic, we set $ds^2 = 0$ and determine the solution for the tangential velocity of light according to Kerr time coordinate t. The Kerr time coordinate corresponds to a clock from the gravitating massive body hence this is the speed of light inferred by a far-away observer. Using Eq. (6.2)

$$\begin{aligned} ds^2 = 0 = -(1-\frac{r_s}{r})dt^2 + (1-\frac{r_s}{r})^{-1}dr^2 \\ + r^2 d\phi^2 - \frac{2r_s a}{r} d\phi dt. \end{aligned} \tag{6.3}$$

The tangential distance is $dx = rd\phi$ and the light geodesic solution is

$$0 = -(1-r_s/r) + \dot{x}^2 - \frac{2r_s a}{r^2}\dot{x}, \tag{6.4}$$

where $\dot{x} = \frac{dx}{dt}$. However, if $\frac{a}{r} << 1$ and $\frac{r_s}{r} << 1$ we have the weak field solution

$$\begin{aligned} \frac{dx}{dt} &\approx \frac{r_s a}{r^2} \pm \sqrt{1-\frac{r_s}{r}} \\ &\approx \pm(1-\frac{r_s}{2r} \pm \frac{r_s a}{r^2}), \end{aligned} \tag{6.5}$$

where we have used the Taylor expansion $\sqrt{1-x} \approx 1 - \frac{x}{2}$. We have two solutions representing counter- and co-rotating light. Notice that locally, $\frac{dx}{dt}\frac{dt}{d\tau} \approx (1-\frac{r_s}{2r}+\frac{r_s a}{r^2})(1+\frac{r_s}{2r}) = 1 + \frac{r_s a}{r^2}$ can exceed 1 for the positive solution. However, we cannot naively use the Schwarzschild coordinate time in this curved metric. Later we will show that there is a locally flat metric where $c = 1$.

6.2.3 Height differential effect

Let's consider a stationary observer in the Kerr metric sending co-moving beams of light that travel tangentially at velocities $c_1 = 1 - v_1 - \frac{r_s}{2r_1}$ and $c_2 = 1 - v_2 - \frac{r_s}{2r_2}$ at radiuses r_1 and $r_2 = r_1 + h$ where h is the coordinate height. For simplicity we made the weak field approximation and only retained terms from Eq. (7.3) to first order in $v_{1,2} = \frac{r_s a}{r_{1,2}^2}$. The light travels the distance L with time $t_1 = \frac{L}{c_1}$. Similarly, the second observer measures the travel time $t_2 = \frac{L}{c_2}$. The far-away observer agrees that the length L is the same for both. Thus the time delay to first order is

$$\begin{aligned} \Delta t_r = \frac{L}{c_1} - \frac{L}{c_2} &= L(\frac{1}{(1-v_1-\frac{r_s}{2r_1})} - \frac{1}{(1-v_2-\frac{r_s}{2r_2})}) \\ &\approx L(r_s a(\frac{1}{r_1^2} - \frac{1}{r_2^2})) + \frac{Lhr_s}{2r_1 r_2} \\ &\approx \frac{Lr_s ah(2r_1+h)}{r_1^4(1+\frac{h}{r_1})^2} + \frac{Lhr_s}{2r_1^2(1+\frac{h}{r_1})} \\ &\approx \frac{2Lr_s ah}{r_1^3} + \frac{Lhr_s}{2r_1^2}, \end{aligned} \tag{6.6}$$

where we have ignored the cross term $\frac{r_s v_1}{2r_1} - \frac{r_s v_2}{2r_2}$ since it is much smaller and enforced the approximation $h << r_1$. This time delay can be incorporated into a Mach-Zehnder interferometric arrangement which can be rotated along its centre to measure the phase for $+a$ and $-a$ as will be discussed shortly.

6.3 Quantum Limited Estimation of the Kerr space-time parameter

Using these time delays, we want to determine the ultimate bound for estimating the Kerr metric parameter a. The optimal variance of an unbiased estimator is determined by the Quantum Cramér-Rao (QCR) bound [9]. In quantum information theory, for M independent measurements, the QCR bound for the linear phase estimator ϕ is given by $\langle \Delta\hat{\phi}^2 \rangle \geq \frac{1}{M\mathcal{H}(\Delta\phi)}$. Where $\mathcal{H}(\phi)$ is the quantum Fisher Information which characterizes the ultimate achievable parameter estimation precision by an optimal quantum measurement.

We have seen that we can measure the phase $\Delta\phi = \omega\Delta t_r$ at different heights where ω is the central frequency of the probe and Δt_r is given by Eq. (6.6). The QCR bound for the Kerr rotation parameter is then (as in Chapter 4.4)

$$\frac{\langle \Delta a \rangle}{a} \geq \frac{r_1^3(1+\frac{h}{r_1})^2}{\omega L a r_s h (2+\frac{h}{r_1})\sqrt{M\mathcal{H}(\Delta\phi)}}. \tag{6.7}$$

In general $r_1 >> h$ and therefore the Kerr parameter standard deviation scales as $\langle \Delta a \rangle \gtrapprox \frac{r_1^3}{2\omega L r_s h\sqrt{MN}}$.

A larger height difference h or length L reduces the noise limit. For coherent probe states undergoing linear phase evolution, $\mathcal{H}(\phi) = |\alpha|^2 = N$. Therefore, we have the standard quantum noise limit $\propto \frac{1}{\sqrt{N}}$ as expected for coherent probe states. By using non-classical squeezed states the noise scales as $\frac{1}{N}$, known as the conventional Heisenberg limit [19, 20] or with χ Kerr non-linearities the noise can scale as $\frac{1}{N^{3/2}}$ [21, 22].

6.3.1 Mach-Zehnder interferometer

Let's consider a physical system that can detect the discrepancy in the velocity of light from the differential height effect in the Kerr metric. We consider a Mach-Zehnder interferometer (see Fig. 6.1) that is stationary with respect to the centre of mass of a rotating planet. We will work in far-away time coordinates. Although the

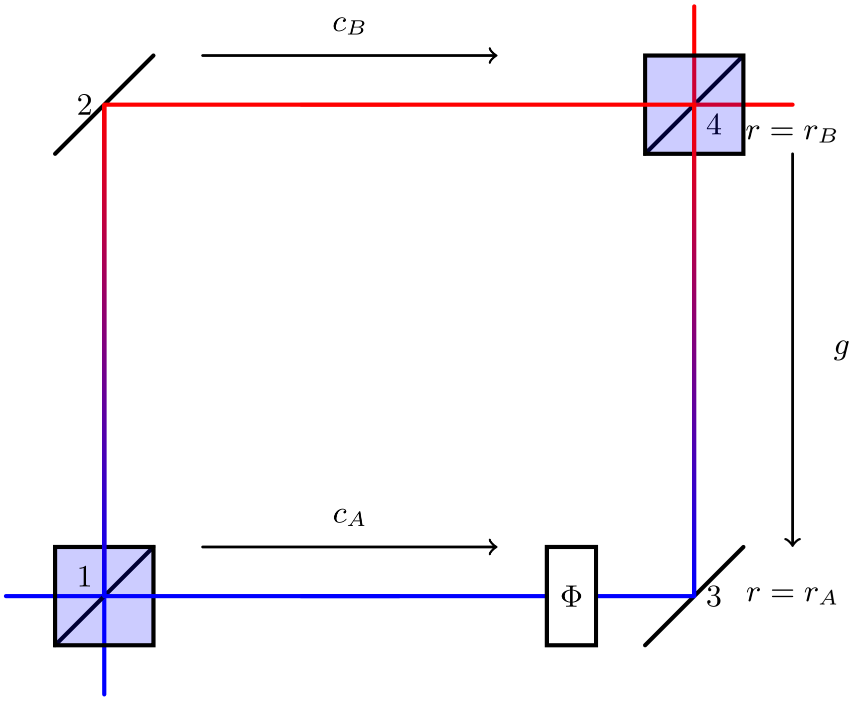

Figure 6.1: A Mach-Zehnder interferometer of length L and height h stationary above the rotating planet where $r_B > r_A$ and the direction of the gravitational field is downwards. Φ is a phase shifter in the bottom arm to calibrate the interferometer to a dark port of zero intensity.

final implications will be the same, this is an approach where no assumption is made about how the speed of light is measured locally.

The measured phase of the bottom arm of the Mach-Zehnder interferometer is $\Delta\phi_A = \omega\Delta t_A$ where ω is the frequency of light measured locally at the source and Δt_A is the time as seen by a faraway observer, and Φ is a local phase shifter. At $r = r_A$ the faraway time $\Delta t_A = \frac{L}{c_A}$ where c_A is the speed of light as measured by a faraway observer (see Eq. (7.3)) and L is the arm length also seen by a faraway observer. We have set both arm lengths to be the same. Thus, in the top arm at $r = r_B = r_A + h$, the phase is $\Delta\phi_B = \omega\Delta t_B = \omega\frac{L}{c_B}$.

We assume that $dr = 0$ and the Mach-Zehnder interferometer arms are sufficiently small that the curvature is negligible. The tangential velocity of light depends on R and the sign of a. The solution in the weak field limit is $c' = \frac{dx}{dt} = R\frac{d\phi}{dt} \approx 1 \pm \frac{r_s a}{r^2} - \frac{r_s}{2r}$. Where we have chosen the co-moving direction such that $c_A \approx 1 - \frac{r_s a}{r_A^2} - \frac{r_s}{2r_A}$ and

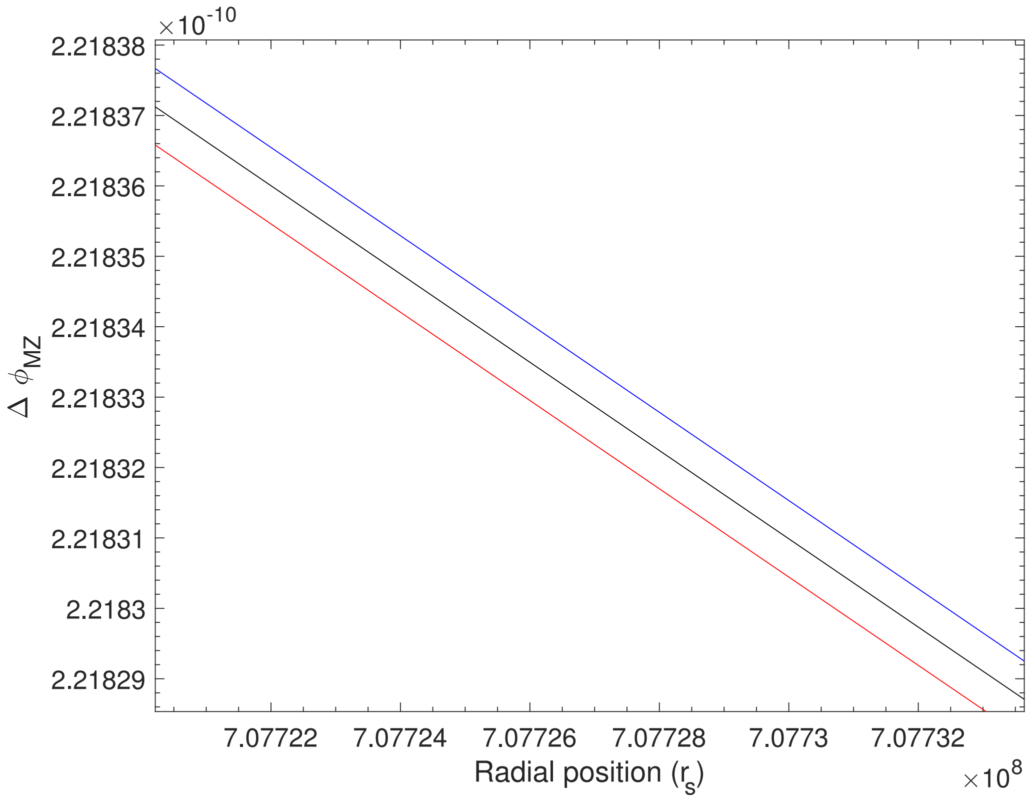

Figure 6.2: Measured phase differences of $L = 1\ m$ and $h = 1\ m$ Mach-Zehnder interferometer in co- and counter- moving directions (blue and red respectively) with respect to the radial position in units of the Schwarzschild radius r_s. Black line is in the Schwarzschild metric with $a = 0$. We use the values for the Earth's Schwarzschild radius $r_s = 9\ mm$, rotation parameter $a = 3.9\ m$ and the operating frequency of light $\omega = k = 2 \times 10^6\ m^{-1}$ corresponding to 500 nm measured locally at the source.

$c_B \approx 1 - \frac{r_s a}{r_B^2} - \frac{r_s}{2r_B}$. The phase is thus

$$\begin{aligned}
\Delta\phi_{MZ} - \Phi &= \omega\left(\frac{L}{c_B} - \frac{L}{c_A}\right) \\
&\approx \omega L\left(\left(1 + \frac{r_s a}{r_B^2} + \frac{r_s}{2r_B} + \frac{r_s^2 a}{r_B^3} + \frac{r_s^2}{4r_B^2} + \frac{r_s^2 a^2}{r_B^4}\right)\right. \\
&\quad \left. - \left(1 + \frac{r_s a}{r_A^2} + \frac{r_s}{2r_A} + \frac{r_s^2 a}{r_A^3} + \frac{r_s^2}{4r_A^2} + \frac{r_s^2 a^2}{r_B^4}\right)\right) \\
&\approx \omega L\left(-\frac{r_s a h(2r_A + h)}{r_A^4(1 + \frac{h}{r_A})^2} - \frac{h r_s}{2r_A^2(1 + \frac{h}{r_A})}\right),
\end{aligned} \tag{6.8}$$

where we have used the Taylor expansion $\frac{1}{1-x-y} \approx 1 + x + y$. Note that the quadratic terms are too small and can be neglected in further calculations. We have made the approximations $\frac{r_s}{r_{A,B}} << 1$, $\frac{a}{r_{A,B}} << 1$ and $h << r_A, r_B$. Note that for the vertical arms, the accumulated phases are equal $\Delta\phi_{12} = \Delta\phi_{34}$ implying that there is no contribution to the total output phase.

We note that on Earth scale the effect of the Kerr rotation parameter is small. If we use the values for the Earth's Schwarzschild radius $r_s = 9\ mm$, rotation parameter $a = 3.9\ m$ and radius $r_B = 6.37 \times 10^6\ m$, and take the area of the interferometer as $A = L \times h = 1\ m^2$ and the operating frequency of light $k = 2 \times 10^6\ m^{-1}$ (wavelength of 500 nm) then the order of magnitude of the dominant term for the Kerr rotating effect is

$$|\Delta\phi_{Kerr}| \approx \frac{2kr_s aLh}{r_B^3} \approx 5 \times 10^{-16}. \tag{6.9}$$

Conversely, the Schwarzschild time dilation effect is of the order $\Delta\phi_{Schwarzschild} = \frac{\omega Lhr_s}{2r_A r_B} = 2.2 \times 10^{-10}$.

MZ interferometer calibration. We set the total phase shift $\Delta\phi_{MZ} = 0$ and thus the phase shifter Φ balances the interferometer to the dark port. Isolating the Kerr phase around the dark port is an optimal strategy for maximizing signal to noise ratio. We can see in Fig. 6.2 the phase of the interferometer if it were positioned in the co- and counter-moving directions. Thus, we can rotate the Mach-Zehnder interferometer with angle π around its vertical axis and measure the a sign dependence directly. Since only the sign of a changes and Φ stays the same then we have,

$$\begin{aligned} \Delta'\phi_{MZ} - \Phi &\approx 2\omega L(\Omega_A r_A - \Omega_B r_B - r_s(\Omega_B - \Omega_A)) \\ &\approx 2|\Delta\phi_{Kerr}|. \end{aligned} \tag{6.10}$$

Note that we have defined $\Omega_{A,B} = \frac{r_s a}{r_{A,B}^3}$. Therefore, we have a signal which only depends on a. Without the anisotropy of the speed of light, there would be no signal and the phase would remain a dark port.

6.4 Zero Angular Momentum Observer metric

The co- and counter-propagating null light geodesics differ in the Kerr metric. However, locally we expect observers to isotropically measure $c = 1$. It would be useful to transform to a reference frame in which the cross terms $d\phi dt$ vanish and where locally we obtain a flat space-time metric with $c = 1$ [17]. To determine this transformation, we consider the Killing vectors ∂_t and ∂_ϕ that are responsible for two conserved quantities along the geodesic. These are the energy

$$E = -k_\mu u^\mu = -g_{t\mu}u^\mu = -p_t = (1 - \frac{r_s}{r})\frac{dt}{d\tau} + \frac{r_s a}{r}\frac{d\phi}{d\tau}, \tag{6.11}$$

and the angular momentum

$$\mathcal{L} = g_{\phi\mu}u^{\mu} = -\frac{r_s a}{r}\frac{dt}{d\tau} + r^2\frac{d\phi}{d\tau}. \tag{6.12}$$

When we set $\mathcal{L} = 0$ then we have that $\frac{d\phi}{dt} = \frac{r_s a}{r^3}$. Thus there remains an angular motion even with zero angular momentum. The interpretation here is that the rotating space-time drags an object close to the rotating mass, as seen by a far-away observer. If we are co-rotating in the zero angular momentum reference frame $d\phi' = d\phi_{ring} + \Omega dt$ with angular velocity $\Omega = \frac{r_s a}{r^3}$ then the metric cross terms $d\phi dt$ cancel out and the line element becomes

$$ds^2 = -(1 - \frac{r_s}{r})dt^2 + r^2 d\phi_{ring}^2. \tag{6.13}$$

This is known as the zero angular momentum observer (ZAMO) metric [17]. Taking $dt_{ring} = \sqrt{1 - \frac{r_{shell}}{r}}\, dt$ we have that

$$ds^2 = dt_{ring}^2 - r^2 d\phi_{ring}^2, \tag{6.14}$$

giving a locally flat metric for the ringriders in which $c = 1$.

We seek the metric in stationary shell coordinates

$$ds'^2 = dt_s^2 - r_{shell}^2 d\phi_{ring}^2, \tag{6.15}$$

where obviously again $c = 1$ locally.

However, there is a lack of simultaneity between events in the shell metric and events in the ring-rider metric (and hence faraway events). This is the source of the anisotropy of the speed of light. We have from the Lorentz transformation that a space-like event implies $dt_{ring} = \gamma(dt_s - v dx_s) = 0$ where $v = \Omega r$ and $dx_s = r_{shell} d\phi_{ring}$, thus $dt_s = v r_{shell} d\phi_{ring}$.

From the equivalence of the line elements we have

$$\begin{aligned} ds^2 &= ds'^2 \\ -r^2 d\phi_{ring}^2 &= v^2 r_{shell}^2 d\phi_{ring}^2 - r_{shell}^2 d\phi_{ring}^2. \end{aligned} \tag{6.16}$$

Therefore the ring-rider radius and stationary observer radius are equivalent $r = r_{shell}$.

We have redefined the coordinate times of the respective ring-riders as the Schwarzschild time $d\tau = \sqrt{1 - \frac{r_s}{r}}\, dt$. Between ring-riders, we have the usual Schwarzschild time dilation, as expected. The advantage of the ring-rider frame is that we can use Lorentz transformations to the stationary observer frame to determine the much more significant height differential effect.

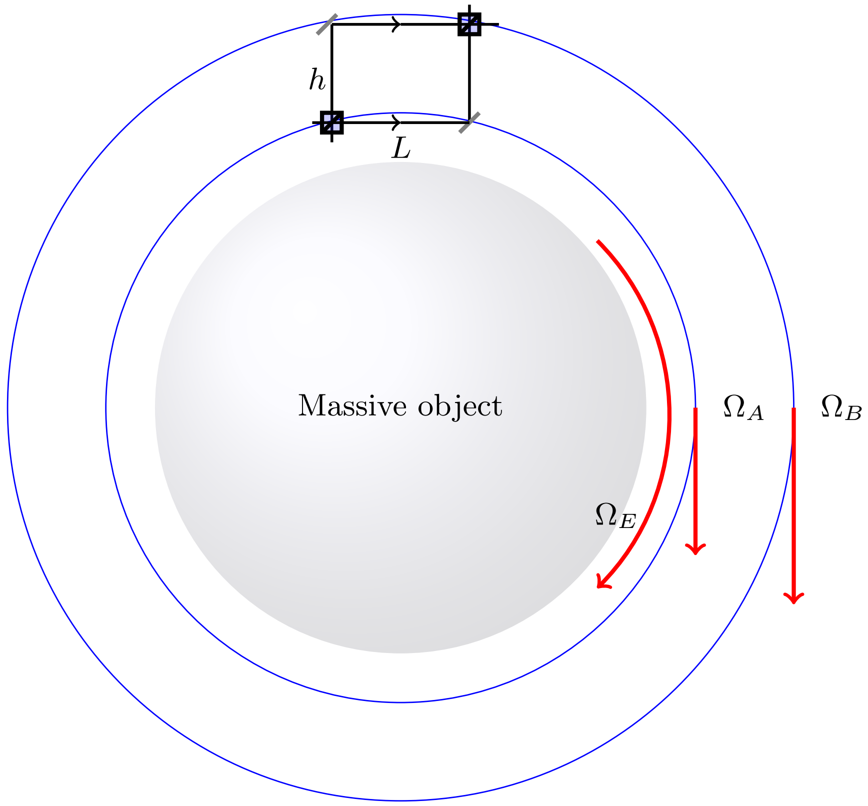

Figure 6.3: A Mach-Zehnder interferometer of length L and height h stationary above the rotating massive object in the Kerr metric. Zero angular momentum ring-riders (blue) will have a locally flat space-time with $c = 1$. Their angular frequency as seen from a far-away observer (red) are given by $\Omega_A = \frac{r_s a}{r_A^3}$ and $\Omega_B = \frac{r_s a}{r_B^3}$.

6.5 Ring-rider perspective

We have previously shown that in the ZAMO flat metric the speed of light is $c = 1$. It is helpful in understanding the physics of our estimation protocols to consider them from the perspective of ring-rider observers. This is also a convenient method to generalize to non-stationary interferometers.

6.5.1 Stationary Mach-Zehnder above rotating massive object

Let's consider the Mach-Zehnder interferometer from the reference frames of the ring-riders. The ring-riders are in the flat metric (see Fig. 6.3). Therefore, for each ring-rider, we can use the Lorentz Transformations. We maintain for now the weak field approximations that $\frac{a}{R} << 1$ and $\frac{r_s}{r} << 1$ such that the Mach-Zehnder interferometer is far enough away from the centre of the massive body. Taking into account special relativity, a stationary observer would measure the travel time of light

$$\begin{aligned} t_1' &= \gamma(t_1 + v_A x_A) = \gamma(L + v_A L) \\ &= \sqrt{\frac{1+v_A}{1-v_A}}\, L \approx (1+v_A)L, \end{aligned} \tag{6.17}$$

where $v_A = \Omega_A r_A$ is the relative velocity between the ring-rider and stationary observer at r_A and $t_1 = L$ is the travel time in the ZAMO flat metric. Note that the stationary observer as seen by the ring-rider is travelling in the negative x direction. Similarly, for the ring-rider at R_B, $t_2' = \sqrt{\frac{1+v_B}{1-v_B}}\, L \approx (1+v_B)L$ where $v_B = \Omega_B r_B$. For an observer at $r = \infty$, we use the coordinate times of the ZAMO metric. Since the coordinate times are

$$t_1'' = \frac{t_1'}{\sqrt{1-\frac{r_s}{r_A}}} \approx (1+\frac{r_s}{2r_A})L(1+v_A), \tag{6.18}$$

and

$$t_2'' = \frac{t_2'}{\sqrt{1-\frac{r_s}{r_B}}} \approx (1+\frac{r_s}{2r_B})L(1+v_B). \tag{6.19}$$

Thus the time delay is

$$\begin{aligned} \Delta t = t_2'' - t_1'' &= L((1+\frac{r_s}{2r_B})(1+\Omega_B r_B) \\ &\quad - (1+\frac{r_s}{2r_A})(1+\Omega_A r_A)) \\ &\approx L(\Omega_B r_B - \Omega_A r_A - \frac{r_s h}{2r_A r_B}). \end{aligned} \tag{6.20}$$

These calculations are equivalent with using the null geodesics obtained from using the Kerr Metric in far-away coordinates in Eq. (6.8).

6.5.2 Michelson interferometer

Given that the far-away observer sees an anisotropic speed of light it is instructive to ask why a local Michelson interferometer fails to see an effect. A stationary observer sends a light beam tangential to the equator that bounces off a mirror L distance away and returns to the observer. The time delay in this signal arm would be

$$\begin{aligned} \Delta t_{Signal} &= \frac{L}{\sqrt{1-\frac{r_s}{r}}}(1+v) \\ &\quad + \frac{L}{\sqrt{1-\frac{r_s}{r}}}(1-v) \\ &\approx 2L(1+\frac{r_s}{2r}). \end{aligned} \tag{6.21}$$

The reference arm perpendicular to the equator is approximately the Schwarzschild local time as found in Eq. (6.29) (see Appendix 6.8). This is the same phase as the signal arm $\Delta t_{Ref} \approx 2L(1+\frac{r_s}{2r})$. Thus the total phase difference is $\Delta\phi_{Michelson} = 0$, implying that the speed of light is $c = 1$ locally and isotropic, as expected from the special theory of relativity. From the point of view of the far-away observer, although the speed of light is anisotropic, they find the "two-way" speed, to the mirror and back, is the same in each direction, leading to no phase shift. It may seem a contradiction with the results of the height differential effect, which requires c to be anisotropic to see a signal in the MZ interferometer. However, this is due to a difference in the amount of space-time dragging at different radial positions in the Kerr metric that the MZ interferometer measures non-locally.

6.5.3 Non-stationary co-moving observers on Earth

In an experiment conducted say on Earth, the rotation of the non-stationary Earth observers must be taken into account. Our previous calculations have considered only a stationary Mach-Zehnder interferometer with the Earth rotating beneath. However, let's consider the bottom arm of the MZ interferometer on Earth's surface with the tangential velocity $v'_A = \Omega_E r_A - \Omega_A r_A$ and the top arm co-moving at $v'_B = \Omega_E r_B - \Omega_B r_B$ with the same angular velocity Ω_E of Earth. This relative velocity between observers introduces an additional time dilation.

Using the Lorentz transformations, a stationary observer observer would measure the travel time of light at r_A

$$\begin{aligned} t'_1 &= \gamma(t_1 + v_A x_A) = \gamma(L + v'_A L) = \sqrt{\frac{1+v'_A}{1-v'_A}}\,L \\ &\approx (1 + v'_A + \frac{v'^2_A}{2})L. \end{aligned} \tag{6.22}$$

Similarly, for the moving observer at r_B

$$t'_2 = \sqrt{\frac{1+v'_B}{1-v'_B}}\,L \approx (1 + v'_B + \frac{v'^2_B}{2})L. \tag{6.23}$$

For an observer at $r = \infty$, we use the coordinate times of the ZAMO metric,

$t''_A = \frac{t'_1}{\sqrt{1-\frac{r_s}{r_A}}}$ and $t''_B = \frac{t'_2}{\sqrt{1-\frac{r_s}{r_B}}}$. Thus

$$\begin{aligned}\Delta t &= t''_B - t''_A \\ &= L((1+\frac{r_s}{2r_B})(1+v'_B+\frac{v'^2_B}{2}) \\ &- (1+\frac{r_s}{2r_A})(1+v'_A+\frac{v'^2_A}{2})) \\ &\approx L(\frac{r_s h}{2r_A r_B}+v'_B-v'_A+\frac{r_s v'_B}{2r_B}-\frac{r_s v'_A}{2r_A}) \\ &\approx \Delta t_{MZ}+\Omega_E hL+\frac{\Omega_E^2 hL(2r_A+h)}{2},\end{aligned} \tag{6.24}$$

where we have neglected the terms $(\Omega_A r_A)^2$ and $(\Omega_B r_B)^2$. The term $\Omega_E hL$ is a classical effect due to the relative motion of the observers but the term $\frac{\Omega_E^2 h(2r_A+h)L}{2}$ is the higher order correction due to special relativity. We calibrate the MZ interferometer such that the total phase $\Delta\phi_{MZ} = 0$ and then we rotate it. The only remaining terms in Eq. (6.24) are linear with the rotation. Thus the new phase is

$$\Delta\phi'_{MZ} = 2\Delta\phi_{Kerr} + 2\omega_0\Omega_E hL. \tag{6.25}$$

The Kerr phase varies inversely with r^3, and thus in principle can be distinguished from the classical effect. However, let's consider unequal arm lengths of the interferometer such that the classical term cancels. Thus we have $r_A L_A = r_B L_B$, and the Kerr phase is

$$\begin{aligned}|\Delta\phi_{Kerr}| &\approx \frac{\omega_0 L_B r_s a}{r_B^2} - \frac{\omega_0 L_A r_s a}{r_A^2} \\ &= \omega_0 r_s a(\frac{L_A r_A}{r_A^3(1+\frac{h}{r_A})^3} - \frac{L_A}{r_A^2}) \\ &\approx \frac{3\omega_0 L_A h r_s a}{r_A^3}.\end{aligned} \tag{6.26}$$

We note that the vertical phases $\Delta\phi_{12}$ and $\Delta\phi_{34}$ are not equal to each other. However, since we rotate the Mach-Zehnder interferometer through π then $\Delta'\phi_{12} = \Delta\phi_{34}$ and $\Delta'\phi_{34} = \Delta\phi_{12}$. Thus the phase difference (given calibration to the dark port before rotation) at the output has no contribution from the phases of the vertical arms.

6.5.4 Probing the Kerr phase on Earth using MZ interferometer

An interesting calculation is to estimate how compact an object with Earth mass and spin would need to be such that the Kerr term was dominant over the effect

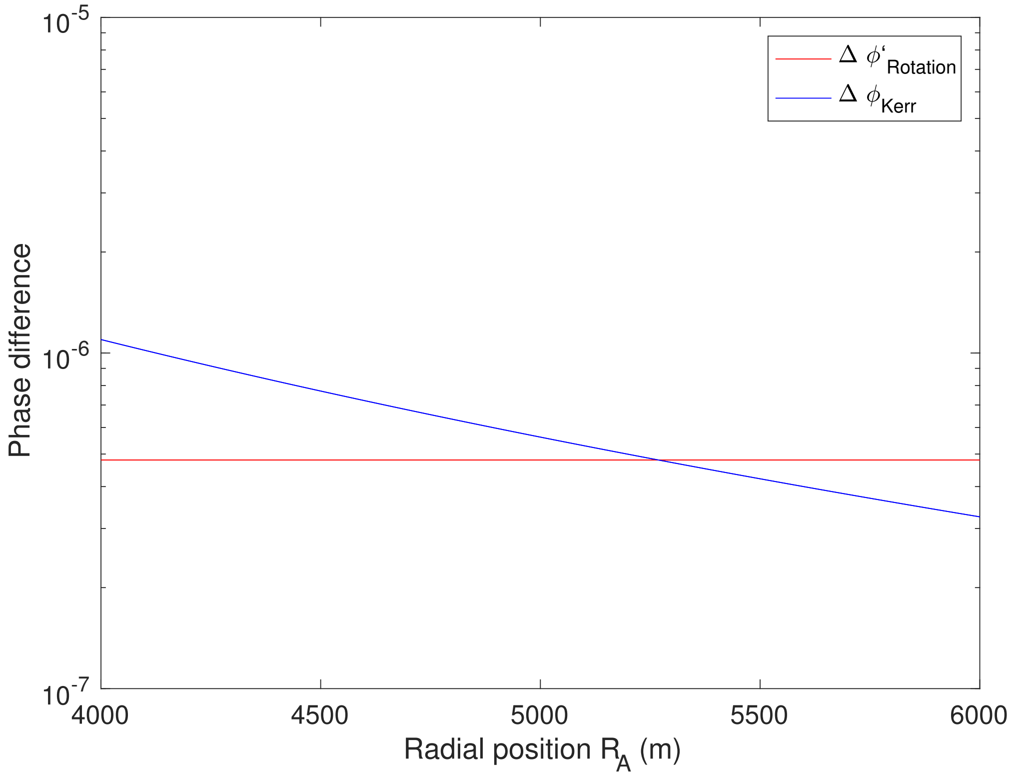

Figure 6.4: Measured phase differences of $L = 1\ m$ and $h = 1\ m$ Mach-Zehnder interferometer around the radial position at which the Kerr phase (blue) becomes dominant on Earth compared to the phase due to the classical rotation (red).

of the spin. The relative velocity term is $|\Delta\phi_{Rotation}| = \omega_0 L \Omega_E h \approx 5 \times 10^{-7}$ for a fixed interferometer with the angular frequency of the Earth $\Omega_E = \frac{7.2\times10^{-5}}{c}\ Hz$. To determine a, we need to isolate it from the dominant effect of Earth's rotation.

We can vary the position of the interferometer while keeping its size constant. The contribution from the rotation term $\Delta\phi_{Rotation} \approx \omega_0 \frac{\Omega_E h L}{2}$ is approximately constant. We want to determine at what radial position the Kerr effect becomes dominant. This occurs when $\Delta\phi_{Kerr} \geqslant \Delta\phi_{Rotation}$. Therefore, $\omega_0 L \frac{r_s a h}{r_B^3} = \omega_0 L \Omega_E h$ which implies that $r_B = (\frac{r_s a}{\Omega_E})^{1/3} \approx 5\ km$. Note that the condition $\frac{a}{R_A} << 1$ is still satisfied. In Fig. 7.3, we have the same interferometer over a range of positions extending $2\ km$ around the point at which the Kerr phase becomes significant. Clearly an Earth bound measurement is very far from this condition. However, for a compact object such as a neutron star of the same Schwarzschild radius it is possible in principle.

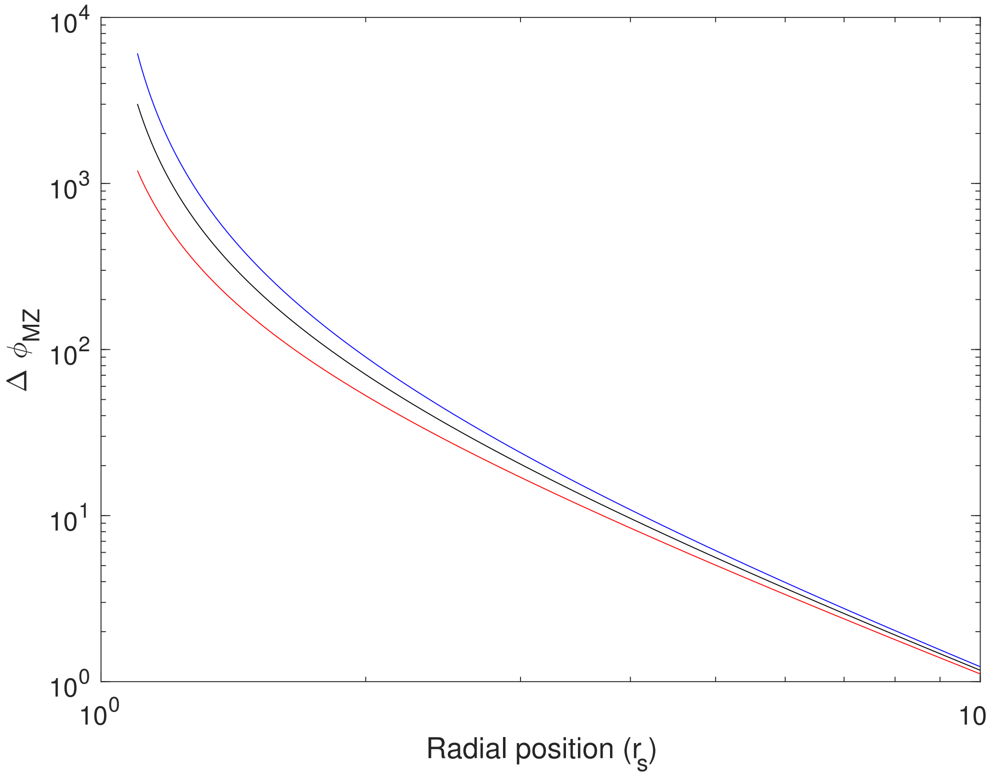

Figure 6.5: Measured phase differences of $L = 1\ m$ and $h = 1\ m$ Mach-Zehnder interferometer near a black hole of Schwarzschild radius $r_s = 10\ km$, angular momentum $a = \frac{r_s}{8}$ and the operating frequency of light $k = 2 \times 10^6\ m^{-1}$. Here we have the MZ phases for co-moving (red), counter-moving (blue) and no rotation $a = 0$ (black).

6.6 Extremal Black Holes

To explore the strong field situation, let's now lower our stationary Mach-Zehnder interferometer close to a black hole. We can no longer use the approximations $\frac{a}{r} << 1$ and $\frac{r_s}{r} << 1$. We must use the full solution of c_A and c_B of the unapproximated Kerr metric as in Eq. (6.1) and calculated in Appendix 6.9. We note that the Kerr metric is a good description for a collapsed black hole, but not for the exterior metric of neutron stars [23]. We can see in Fig. 6.5 for a black hole of Schwarzschild radius $r_s = 10\ km$ and angular momentum $a = \frac{r_s}{8}$, the phase difference for a co- (red) and counter- (blue) direction Mach Zehnder interferometer. The two directions of the Mach-Zehnder interferometer become increasingly distinguishable as it gets closer to the event horizon at $r = r_s$.

6.7 Conclusion

We have determined the quantum limits of estimating the Kerr parameter which arises from the anisotropy of the speed of light. We propose a stationary Mach-Zehnder interferometer that can directly measure the Kerr parameter a direction dependence. We identify the flat metric where the ring-rider velocity of light is locally $c = 1$. We find the same Kerr phase using Lorentz transformations between stationary and ring-riders in this ZAMO flat metric. Also, we find that the "two-way" velocity of light is isotropic and $c = 1$ as measured by a Michelson interferometer. However, our Mach-Zehnder interferometer is no longer a dark port after it is rotated by π because of the combined effect of the anisotropy of light and the difference in the amount of space-time dragging in the radial position. On Earth, we have to consider non-stationary observers which adds an additional classical phase that dominates the Kerr phase. Using a variation on the Mach-Zehnder set-up can cancel this additional classical phase with only the Kerr phase remaining.

Recent experiments using microwave resonators have been able to detect the anisotropy of light with a precision of $\Delta c/c \approx 10^{-17}$ [11]. Our Mach-Zehnder interferometer predicts a change in the speed of light due to the Kerr metric of $\Delta c_{Kerr}/c = \frac{har_s}{r^3} \approx 10^{-20}$. In principle, future devices need to increase precision by 3 orders of magnitude to measure the Kerr phase on a small scale Mach-Zehnder interferometer. Using coherent probe states, the noise of the phase is the standard noise limit (SNL) $\Delta\phi \geq \frac{1}{\sqrt{MN}}$. For $M = 10\ GHz$ measurements [24], this suggests that $N = 10^{22} - 10^{26}$ per light pulse. This would imply extremely high power, which is one of the current limiting factor to increasing phase sensitivity.

Acknowledgements

We thank Jorma Louko for pointing out an error in the original manuscript and also Robert Mann and Daiqin Su for useful discussions. This work was supported in part by the Australian Research Council Centre of Excellence for Quantum Computation and Communication Technology (Project No. CE110001027) and financial support by an Australian Government Research Training Program Scholarship.

Bibliography

[1] *Quantum Metrology in the Kerr metric*, S. P. Kish, T. C. Ralph, Phys. Rev. D **99**, 124015 (2019).

[2] *Advances in quantum metrology*, V. Giovanetti, S. Lloyd, and L. Maccone, Nat. Photon. **5**, 222 (2011).

[3] *Observation of Gravitational Waves from a Binary Black Hole Merger*, B. P. Abbott et al., Phys. Rev. Lett. **116**, 061102 (2016).

[4] *Quantum estimation of the Schwarzschild spacetime parameters of the Earth*, D. Bruschi, A. Datta, R. Ursin, T. C. Ralph, and I. Fuentes, Phys. Rev. D **90**, 124001 (2014).

[5] *Quantum Estimation of Parameters of Classical Spacetimes*, T. G. Downes, J. R. van Meter, E. Knill, G. J. Milburn, C. M. Caves, Phys. Rev. D. **96** 105004 (2016).

[6] *Detection of gravitational frame dragging using orbiting qubits*, M. Lanzagorta & M. Salgado, Class. Quantum Grav. **33** 105013 (2016).

[7] *Spacetime effects on satellite-based quantum communications*, D. Bruschi, T. C. Ralph, I. Fuentes, T. Jennewein, M. Razavi, Phys. Rev. D **90**, 045041 (2014).

[8] *Quantum communications and quantum metrology in the spacetime of a rotating planet*, Kohlrus, J., Bruschi, D.E., Louko, J. et al. EPJ Quantum Technol. (2017) 4: 7.

[9] *Mathematical methods of statistics,* H. Cramér, Princeton University Press, (1946).

[10] *The Kerr spacetime: a brief introduction*, D.L. Wiltshire, M. Visser and S.M. Scott eds., Cambridge University Press, Cambridge, U.K. (2009).

[11] *Rotating optical cavity experiment testing Lorentz invariance at the* 10^{-17} *level*, Herrmann S., Senger A., Mhle K., Nagel M., Kovalchuk E. V., Peters A., Physical Review D. **80**, 105011 (209).

[12] *Slowly Rotating Relativistic Stars*, Hartle J.B. and Thorne K. S., Astr. J. **153** 807 (1968).

[13] *Approximate Kerr-like Metric with Quadrupole*, F. Frutos- Alfaro, International Journal of Astronomy and Astrophysics, **6**, 334-345 (2016).

[14] *Circular geodesics in the Hartle-Thorne metric*, M.A. Abramowicz, G.J.E. Almergren, W. Kluzniak, A.V. Thampan, arXiv:gr-qc/0312070 (2003).

[15] *Equatorial Circular Geodesics in the Hartle-Thorne Spacetime*, D. Bini, K. Boshkayev, R. Ruffini, I. Siutsou, Il Nuovo Cimento vol. **36** C, N. 1 Suppl. 1 (2013).

[16] *Approximate Metric for a Rotating Deformed Mass*, F. Frutos-Alfaro, P. Montero-Camacho, M. Araya-Arguedas, J. Bonatti-Gonzalez, International Journal of Astronomy and Astrophysics, **5**(1):1-10 (2015).

[17] *Exploring Black Holes: Introduction to General Relativity*, E. F. Taylor, J. A Wheeler, Addison Wesley Longman (2000).

[18] *Quantum-mechanical noise in an interferometer*, C. M. Caves, Phys. Rev. D **23**, 1693 (1981).

[19] *Generalised limits for single-parameter quantum estimation*, S. Boixo, S. T. Flammia, C. M. Caves, Phys. Rev. Lett., **98**, 090401 (2007).

[20] *General optimality of the Heisenberg limit for quantum metrology*, M. Zwierz, C. A. Perez-Delgado, P. Kok, Phys. Rev. Lett. **105**, 180402 (2010).

[21] *Breaking the Heisenberg limit with inefficient detectors*, J. Beltrán and A. Luis, Phys. Rev. A **72**, 045801 (2005).

[22] *Quantum limited measurement of space-time curvature with scaling beyond the conventional Heisenberg limit*, S. P. Kish & T. C. Ralph, Phys. Rev. A **96**, 041801(R) (2017).

[23] *An all-purpose metric for the exterior of any kind of rotating neutron star*, G. Pappas, T. A. Apostolatos, MNRAS 429, 30073024 (2013).

[24] *10-GHz, 1.3-ps erbium fiber laser employing soliton pulse shortening*, T. F. Carruthers and I. N. Duling, , Opt. Lett. **21**, 1927 (1996).

6.8 Appendix A: Proper length perpendicular to the equator

Let's consider the proper length perpendicular to the equator. The Kerr metric away from the equator is [10]:

$$ds^2 = -(1 - \frac{r_s r}{\Sigma})dt^2 + \frac{\Sigma}{\Delta}dr^2 + \Sigma d\theta^2 \tag{6.27}$$

Where θ is the azimuth in spherical coordinates, and $\Sigma = r^2 + a^2 \cos\theta^2$.

Therefore, we set $dt = 0$ and $dr = 0$ and get the proper distance $d\sigma = \sqrt{r^2 + a^2\cos^2\theta}\ d\theta$. However, for a massive planet, in the weak field limit, we have $d\sigma = r\sqrt{1 + \frac{a^2}{r^2}\cos^2\theta}\ d\theta \approx rd\theta$. The velocity of light is given by solving the null geodesic for the weak field Kerr metric

$$\begin{aligned} ds^2 = 0 &= -(1 - \frac{r_s r}{r^2 + a^2\cos^2\theta})dt^2 + (r^2 + a^2\cos^2\theta)d\theta^2 \\ &\approx -(1 - \frac{r_s}{r})dt^2 + d\sigma^2 \end{aligned} \tag{6.28}$$

And thus the time travelled by light is

$$\Delta t_{Normal} = \frac{L}{\frac{d\sigma}{dt}} = \frac{L}{\sqrt{1 - \frac{r_s}{r}}} \approx 2L(1 + \frac{r_s}{2r}) \tag{6.29}$$

Which is the same as in the Schwarzschild metric.

6.9 Appendix B: Extremal black holes

Let's consider the full solution to the speed of light without any weak field approximations. The phase is therefore

$$\Delta\phi = \omega(t_B - t_A) = kL(\frac{1}{c_B} - \frac{1}{c_A}) \tag{6.30}$$

Where $c_B = \frac{r_s a}{r_B\sqrt{r_B^2 + a^2(1 + r_s/r_B)}} \pm \sqrt{\frac{r_s^2 a^2}{r_B^2(r_B^2 + a^2(1 + r_s/r_B))} + (1 - \frac{r_s}{r_B})}$. Using units of r_s, $a \to a' r_s$, $r_A \to r'_A r_s$ and $r_B \to r'_B r_s$. This simplifies to $c_B = \frac{1}{r'_B\sqrt{\frac{r'^2_B}{a'^2} + (1 + 1/r'_B)}} \pm \sqrt{\frac{1}{r'^2_B((\frac{r'^2_B}{a'^2} + (1 + 1/r'_B))} + (1 - \frac{1}{r'_B})}$. Let's consider the values of an almost extremal black

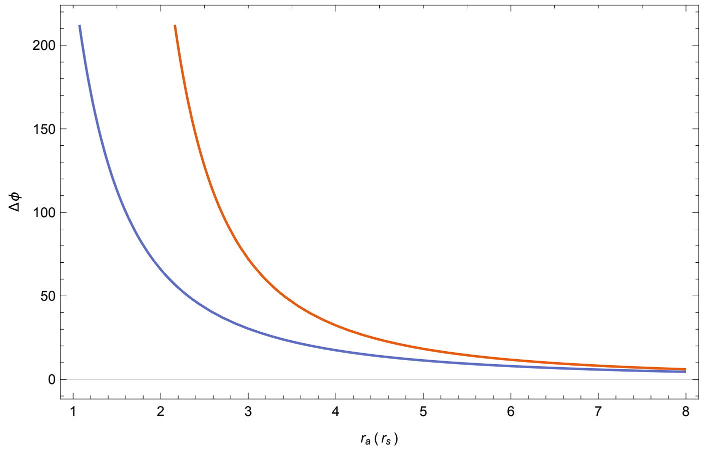

Figure 6.6: Difference in exact phase as determined numerically for full solution of c (red) and weak field approximation (blue). (Note the extremal black hole parameters $r_s = 10\ km$, $h' = 10^{-4}$ and $a' = \frac{1}{8}$)

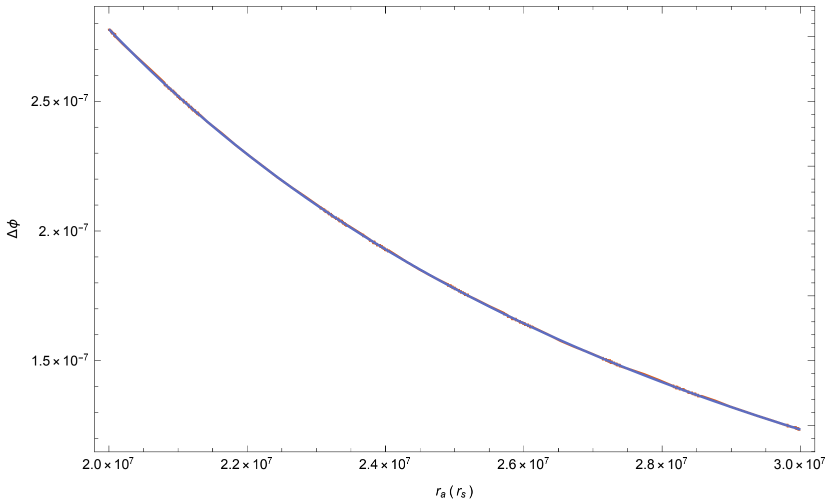

Figure 6.7: Difference in exact phase as determined numerically for full solution of c (red) and weak field approximation (blue) for Earth parameters. (Note that $r_s = 9$ mm, $h' = 111$ and $a' = 433$)

hole with $r_s = 10\ km$, $a' = \frac{1}{8}$ with $r'_B = r'_A + h'$ where $h' = \frac{1}{10000}$ since $h = 1\ m$. We can see in Fig. 7.3 the phase difference for the full solution of c (red) and the weak field approximation (blue) for this extremal black hole. The weak field approximation obviously fails near the event horizon. However, for Earth parameters $r_s = 9\ mm$, $h = 111$ and $a = 433$ representing $h = 1\ m$ and $a = 3.9\ m$, there is no difference between the exact solution for c and the weak field approximation on the Earths surface (see Fig. 6.7).

S. P. Kish has a 75% weighting and T. C. Ralph a 25% weighting of contribution to this chapter. We had both come up with the idea for the chapter. We equally did the results analysis and interpretation. I did most of the theoretical derivations and numerical calculations. I have done the majority of writing and preparation of figures. My supervisor Timothy C. Ralph guided the project in the right direction and contributed to the proofreading.

Chapter 7

Quantum effects in rotating reference frames

The aim of this thesis is to consider high precision measurements in the cross realm of quantum physics and general relativity. In this chapter, we consider a highly sensitive scheme to measure relativistic effects at the quantum level. In contrast with the previous chapter, we consider the time delay of interfering *single photons* oppositely travelling in the Kerr metric of a rotating massive object. Classically, the time delay shows up as a phase difference between coherent sources of light. In quantum mechanics, the loss in visibility of interfering photons with Gaussian mode distribution is directly related to the time delay. We can thus observe the Kerr frame dragging effect using the Hong-Ou-Mandel (HOM) dip, a purely quantum mechanical effect. By Einstein's equivalence principle, we can analogously consider a rotating turntable to simulate the Kerr metric. We look at the feasibility of such an experiment using optical fibre, and note a cancellation in the second order dispersion but a direction dependent difference in group velocity. However, for the chosen experimental parameters, we can effectively assume light propagating through a vacuum.

7.1 Introduction

Most experiments performed to date could be explained by a classical theory of curved space-time or quantum mechanics in flat space-time. These remain to large degree mutually exclusive fields of physics. One of the most fundamental questions of physics today is about the reconciliation between quantum mechanics and Einstein's theory of general relativity. Quantum mechanics in curved space-time has not been as accessible by experiment. Nonetheless, there have been many proposals to test quantum phenomena such as superposition in curved space-time. For example, Ref. [1] considers single photons in superposition at different heights in a gravitational potential. These photons will experience a classical phase shift due to time dilation that is proportional to the gravitational acceleration. The same classical phase can be detected by classical light which doesn't exhibit the quantum mechanical effect of superposition. In previous chapters of this thesis we have exploited this phase shift for parameter estimation. However, if the photons have a pulse (coherence) time comparable to the time dilation, significant loss of quantum interference occurs between the photon wavepackets. A loss in the visibility is seen at the output.

Similarly, we can consider single photons in a large Sagnac interferometer around a rotating massive body described by the Kerr metric. Due to frame dragging, photons co-propagating with the rotation will have a different arrival time compared with photons that counter-propagate with the rotation. Thus, if this time difference is comparable to the pulse time of the photon, loss of quantum interference between photon wavepackets occurs. The loss in visibility now depends on the Kerr parameter a. We can consider an analogous system on a rotating turntable. By Einstein's equivalence principle, the physics should be equivalent whether they are in the space-time of a Kerr metric or accelerating due to the rotation of the turntable. We can observe the time difference due to light velocity using the Hong-Ou-Mandel effect, a purely quantum mechanical effect [2]. The time delay due to rotation at the single photon level as a phase shift has been observed previously [3] and also more recently, with a $N = 2$ NOON state [4]. However, loss in the visibility of the quantum interference has yet to be observed.

We first consider the Kerr effect in the situation where a stationary observer sends a superposition of a co- and counter-propagating photon half-way around the Earth. We find that there is a visibility loss for Gaussian wavepackets due to the time difference of the Kerr metric. Next, we consider a turntable experiment to simulate this effect. We use a HOM Sagnac interferometer to see the loss in visibility due to the time delay caused by rotation. We also consider the relativistic effects of the optical fibre medium. Lastly, we provide calculations for the difference in dispersion of the Gaussian wavepackets. We find that the second order dispersion cancels out in agreement with Ref. [5], but small effects due to a difference in group velocity remain. Nonetheless, for the parameters proposed, we can essentially assume propagation in a vacuum.

7.2 Kerr metric

As in Chapter 6, for a rotating black hole, the Kerr metric describes the effect of the dragging of the space-time. The Kerr line element in Boyer-Lindquist coordinates (t, r, θ, ϕ) is [6]

$$\begin{aligned} ds^2 &= -(1 - \frac{r_s r}{\Sigma})dt^2 + \frac{\Sigma}{\Delta}dr^2 + \Sigma d\theta^2 \\ &+ (r^2 + a^2 + \frac{r_s r a^2}{\Sigma}\sin^2\theta)\sin^2\theta d\phi^2 - \frac{2r_s r a \sin^2\theta}{\Sigma}d\phi dt, \end{aligned} \tag{7.1}$$

where $\Delta := r^2 - r_s r + a^2$, $\Sigma := r^2 + a^2\cos^2\theta$ and $a = \frac{J}{Mc}$ where J is the angular momentum of the object of mass M. Note that the Schwarzschild radius is $r_s = \frac{2GM}{c^2} \equiv 2M$ where we work in natural units for which $c = 1$ and $G = 1$. In the equatorial plane of the metric ($\theta = \frac{\pi}{2}$), a tangential velocity of light can be obtained in terms of tangential proper distance per Kerr coordinate time, solved by setting $ds^2 = 0$. From Chapter 6, the full solution is given by (see also Ref. [7])

$$\begin{aligned} \frac{dx}{dt} &= \frac{r_s a}{r\sqrt{r^2 + a^2(1 + r_s/r)}} \\ &\pm \sqrt{\frac{r_s^2 a^2}{r^2(r^2 + a^2(1 + r_s/r))} + (1 - \frac{r_s}{r})} \,. \end{aligned} \tag{7.2}$$

However, if $\frac{a}{r} << 1$ and $\frac{r_s}{r} << 1$ we have the weak field solution valid for massive planets

$$\begin{aligned} \frac{dx}{dt} &\approx \frac{r_s a}{r^2} \pm \sqrt{1 - \frac{r_s}{r}} \\ &\approx \pm(1 - \frac{r_s}{2r} \pm \frac{r_s a}{r^2}), \end{aligned} \tag{7.3}$$

where we have used the Taylor expansion $\sqrt{1-x} \approx 1 - \frac{x}{2}$. We have two solutions representing counter- and co-rotating light.

7.2.1 Kerr phase difference

Using the solution for the speed of light as seen by a far-away observer in the weak field limit, the phase difference between co- and counter- propagating single photon wavepackets is

$$\begin{aligned}\Delta\Phi = \Phi_B - \Phi_A &= \omega L(\frac{1}{c_B} - \frac{1}{c_A}) \\ &\approx \omega L(\frac{1}{1 - \frac{r_s}{2r} + \frac{r_s a}{r\sqrt{r^2+a^2(1+r_s/r)}}} \\ &- \frac{1}{1 - \frac{r_s}{2r} - \frac{r_s a}{r\sqrt{r^2+a^2(1+r_s/r)}}}) \\ &\approx 2\omega L\frac{r_s a}{r^2}(1+\frac{r_s}{r}) \approx 2\omega\pi\frac{r_s a}{r}.\end{aligned} \tag{7.4}$$

Note that we've neglected second order terms in $\frac{a}{r}$ and above, since $r >> a$ in the weak field limit. For Earth's parameters $a = 3.9\ m$, $r_s = 9\ mm$ on the surface $r = 6.37 \times 10^7\ m$ with visible light of frequency $\omega = k = 2 \times 10^6\ m^{-1}$, the magnitude of the classical Kerr phase half way around the Earth is $\Delta\Phi_{Kerr} = \omega\Delta t_{Kerr} \approx 7 \times 10^{-3}$ where $\Delta t_{Kerr} = 2L\frac{r_s a}{r^2}$. In principle, we could use a large classical Sagnac interferometer to measure this phase.

7.3 Single photon Sagnac interferometer in the Kerr metric

Let's consider a thought experiment where a single photon is in a superposition of two paths around the rotating planet. A stationary single photon source hovering above the rotating planet releases a photon that passes through a beamsplitter and forms a superposition of the paths A and B with phases $\Phi_A = \omega t_A$ and $\Phi_B = \omega t_B$. Paths A and B move semi-circularly around the planet co- and counter- propagating, respectively, with the rotation direction of the planet. These recombine at a second beamsplitter that is half-way around the planet and are detected by a photon number counter.

We begin with the initial state $|1\rangle|0\rangle$ passing through a beamsplitter

$$|1\rangle|0\rangle \to \frac{1}{\sqrt{2}}(|1\rangle|0\rangle + i|0\rangle|1\rangle). \tag{7.5}$$

The two arms experience a different phase shift depending on their trajectories. If the photon is moving with the rotation, it will acquire the phase Φ_A and against the rotation, it will acquire the phase Φ_B. Thus we have the state after the first beamsplitter and subsequent propagation to the second beamsplitter

$$\frac{1}{\sqrt{2}}(e^{i\Phi_A}|1\rangle|0\rangle + ie^{i\Phi_B}|0\rangle|1\rangle). \tag{7.6}$$

After the second beamsplitter, the state becomes

$$\frac{1}{2}(e^{i\Phi_A}(|1\rangle|0\rangle + i|0\rangle|1\rangle + ie^{i\Phi_B}(i|0\rangle|1\rangle + |1\rangle|0\rangle)). \tag{7.7}$$

Thus the number of photons at the output of the second beamsplitter is

$$\begin{aligned}\langle N\rangle &= \langle 0|\langle 0|\frac{1}{2}(e^{-i\Phi_A} - ie^{-i\Phi_B})\frac{1}{2}(e^{i\Phi_A} + ie^{i\Phi_B})|0\rangle|0\rangle \\ &= \frac{1}{2}(1 + \sin(\Phi_A - \Phi_B)).\end{aligned} \tag{7.8}$$

This particular phase can also be measured using classical coherent probe states. Due to this reason, it's usually referred to as a "classical phase".

Consider the single photon mode distribution $f(\omega)a^\dagger_\omega|0\rangle$ where

$$f(\omega) = (\frac{1}{\pi\sigma^2})^{1/4}\exp(-\frac{1}{2\sigma^2}(\omega-\omega_0)^2), \tag{7.9}$$

is the Gaussian distribution with centre frequency ω_0 and σ is the pulse width in frequency space. Thus at the output we have

$$\begin{aligned}\langle N\rangle &= \int d\omega|f(\omega)|^2\langle a^\dagger_\omega a_\omega\rangle \\ &= \frac{1}{2}(1 + \int d\omega(\frac{1}{\pi\sigma^2})^{1/2}\exp(-\frac{1}{\sigma^2}(\omega-\omega_0)^2)\sin\omega\Delta t) \\ &= \frac{1}{2}(1 + e^{-(\frac{\Delta\Phi\sigma}{\omega_0})^2}\sin\Delta\Phi),\end{aligned} \tag{7.10}$$

where the integral is over all positive frequencies ω and $\Delta\Phi$ is given by Eq. (7.4) in the Kerr metric. The visibility is given by

$$\mathcal{V} = e^{-(\frac{\Delta\phi\sigma}{\omega})^2} = e^{-(\Delta t\sigma)^2} \tag{7.11}$$

The additional visibility loss is classified as a quantum effect because it is due to the interference of wavefunctions as opposed to interference of classical modes of the field had we used coherent probe states.

7.3.1 Two-way velocity of light

We now want to determine the average velocity of light that returns to the stationary observer. We expect this to be isotropic and equal to $c = 1$. Let's now consider a double-sided mirror at halfway around the rotating planet that reflects both of the photons back to the original source and the photons interfere. The phase of the co-propagating photon A before interfering with the counter-propagating photon B is

$$\Phi_A + \Phi'_A = \omega L(\frac{1}{1 - \frac{r_s}{2r} + \frac{r_s a}{r^2}}) + \omega L(\frac{1}{1 - \frac{r_s}{2r} - \frac{r_s a}{r^2}}) \approx \omega L(1 + \frac{r_s}{2r}), \tag{7.12}$$

where $\Phi'_A = \Phi_B$ since this the counter-propagating phase. Note we have used the weak field approximation. The mean velocity of the light as seen by a far-away observer is thus $c_{mean} = \frac{1}{1+\frac{r_s}{r}} \approx 1 - \frac{r_s}{r}$. Locally, the velocity of light is $\frac{dx}{d\tau} = c_{mean}\frac{dt}{d\tau} = 1$ where $\frac{dt}{d\tau} = (1 - \frac{r_s}{r})^{-1}$ from setting $dr = 0, d\phi = 0, d\theta = 0$ in the Kerr metric. This implies that the velocity of light is $c = 1$ and isotropic.

Similarly, for the initially counter-propagating photon we have the same phase. Thus no phase difference is detected and the observer infers that $c = 1$.

7.3.2 Visibility loss in the Kerr metric of Earth

Although the Hartle-Thorne metric describes the exterior metric of a massive object with a mass quadrupole moment q, the approximate Kerr metric in the weak field limit disregards q which is of second order in angular momentum. Therefore, massive planets or neutron stars can be described by the Kerr metric up to first order in the angular momentum. If we consider the massive planet to be Earth, the two photon paths will undergo a time delay due to the frame dragging caused by the Kerr metric. Therefore, we have $\mathcal{V} = e^{-(\Delta t_{Kerr}\sigma)^2} e^{-(\frac{2\pi r_s a\sigma}{r})^2} \approx 1 - 1.5 \times 10^{-10}$ where $a = 3.9\ m$, $r_s = 0.009\ m$ and $r = 6.37 \times 10^6\ m$. The visibility loss in the quantum interference would be far too small to be detected on Earth's surface. The radial position at which the visibility would be significant is $r = 2\pi r_s a\sigma \approx 800\ m$, assuming a neutron star with Earth's mass.

7.3.3 Extremal black holes

Let's consider the full solution to the speed of light without any weak field approximations. The phase is therefore

$$\Delta\Phi = \omega(t_B - t_A) = kL(\frac{1}{c_B} - \frac{1}{c_A}), \tag{7.13}$$

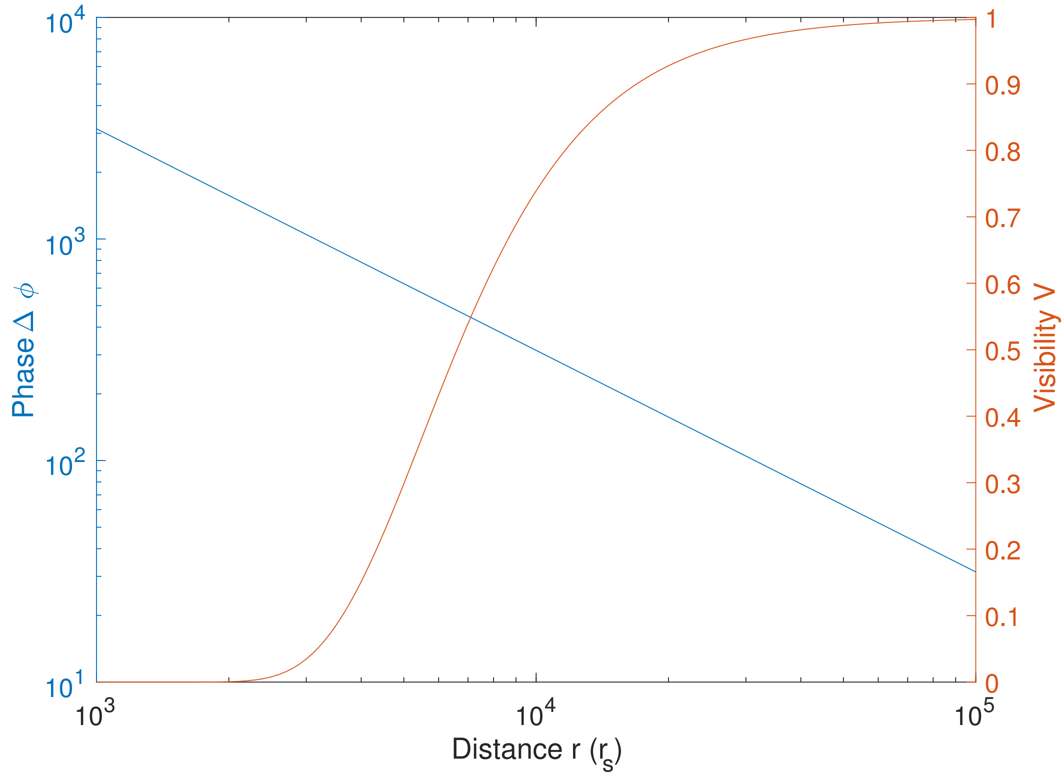

Figure 7.1: Phase difference (light blue) and visibility (orange) of single photons plotted against radial position in units of the Schwarzschild radius r_s from centre of a rotating black hole. (Note the extremal black hole parameters $r_s = 10\ km$, $a' = \frac{1}{4}$ and $\sigma = 3.5 \times 10^3\ m^{-1}$.)

where $c_B = \frac{r_s a}{r_B\sqrt{r_B^2+a^2(1+r_s/r_B)}} \pm \sqrt{\frac{r_s^2 a^2}{r_B^2(r_B^2+a^2(1+r_s/r_B))} + (1-\frac{r_s}{r_B})}$. Using units of r_s, $a \to a'r_s$, $r_A \to r'_A r_s$ and $r_B \to r'_B r_s$. This simplifies to $c_B = \frac{1}{r'_B\sqrt{\frac{r'^2_B}{a'^2}+(1+1/r'_B)}} \pm \sqrt{\frac{1}{r'^2_B((\frac{r'^2_B}{a'^2}+(1+1/r'_B))} + (1-\frac{1}{r'_B})}$. Let's consider the values of an almost extremal black hole with $r_s = 10\ km$, $a' = \frac{1}{4}$ and $\sigma = 3.5 \times 10^3\ m^{-1}$. In Fig. 7.1, we have the phase and the visibility plotted against the radial distance away from the black hole centre. At a particular radial distance, the visibility loss is significant and the wavepackets become completely separated very near the event horizon.

7.4 Rotating reference frame

In this section, we will compare the metric of an inertial observer in a rotating reference frame with an observer in the Kerr metric. Consider an inertial observer on a rotating turntable at a constant radius r with angular frequency Ω as depicted

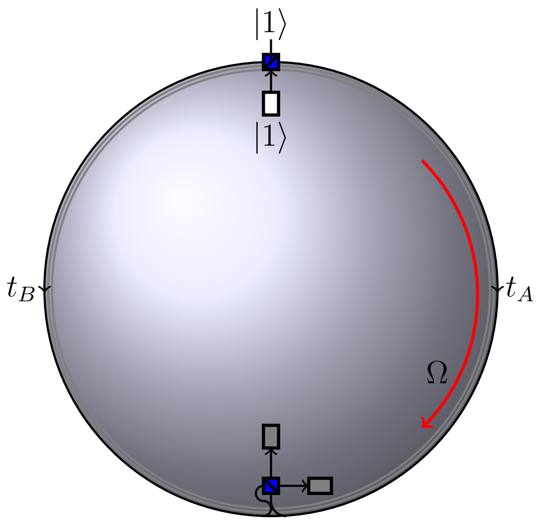

Figure 7.2: A HOM Sagnac interferometer on a turntable rotating at angular frequency Ω. A photon source (white) releases two photons that pass through a beamsplitter and forms a superposition of the paths A and B with phases Φ_A and Φ_B. These recombine at the second beamsplitter and are detected by a photon counter (gray).

in Fig. 7.2.

The metric for a rotating observer in the (1+1) space-time is given by transforming the flat metric using $d\phi \to d\phi + \Omega dt$

$$ds^2_{Rotation} = dt^2 - r^2 d\phi^2 \to (1-v^2)dt^2 - 2vr_t dt d\phi - r_t^2 d\phi^2, \tag{7.14}$$

where the t and ϕ coordinates are the inertial coordinates in the rotating metric and where $v = \Omega r_t$ is the tangential velocity. We compare the rotating metric with the Kerr metric at constant radius in a (1+1) dimensional space-time

$$ds^2_{Kerr} = (1 - \frac{r_s}{r})dt^2 - \frac{2r_s a}{r} dt d\phi - r^2 d\phi^2. \tag{7.15}$$

We require a coordinate transformation for it to match with equation 7.14. Evidently, we require that $r d\phi_{Kerr} = r_t d\phi_{Rotation}$ implying the measured tangential distances are the same. We set the size of the turntable $r_t = r$ which implies that the angular coordinates are equivalent $d\phi_{Kerr} = d\phi_{Rotation}$. However, let's make the following time coordinate transformation in the Kerr metric

$$dt \to \sqrt{\frac{1-v^2}{1-\frac{r_s}{r}}}\, dt. \tag{7.16}$$

Thus

$$ds^2_{Kerr} = (1-v^2)dt^2 - \frac{2r_s a}{r}\sqrt{\frac{1-v^2}{1-\frac{r_s}{r}}}\, dt d\phi - r^2 d\phi^2. \tag{7.17}$$

The $g_{t\phi}$ components must match and we have to solve for v in the equation $vr = \frac{r_s a}{r}\sqrt{\frac{1-v^2}{1-\frac{r_s}{r}}}$. We find that the velocity of the rotating turntable for simulating a Kerr reference frame must be

$$v = \pm\frac{r_s a}{r^2\sqrt{1-\frac{r_s}{r}+\frac{r_s^2 a^2}{r^4}}} \approx \pm\frac{r_s a}{r^2\sqrt{1-\frac{r_s}{r}}}. \tag{7.18}$$

By Einstein's equivalence principle, the observer cannot tell whether they are in the (1+1) local space-time of a Kerr metric or in an inertial rotating reference frame of a turntable. Therefore, we can simulate tangential motion in a (1+1) Kerr space-time if we choose an appropriate velocity for the turntable, and use appropriate clocks.

For example, for a turntable of Earth's radius $r = 6.37 \times 10^7\ m$, we can simulate the Earth's Kerr metric with a turntable velocity of $v = \frac{r_s a}{r^2\sqrt{1-\frac{r_s}{r}}} \approx 2.6 \times 10^{-7}\ m/s$ or angular frequency $\Omega = 4.1 \times 10^{-14}\ rad/s$. Implying that it is extremely slowly rotating. Alternatively, for an Earth mass black hole, and turntable radius of $r = 100$ m then the velocity of the turntable with the same radius would have to be $v = 110$ m/s to match the effects of the Kerr metric.

7.4.1 Time shift

An alternative scenario is where both observers in either metrics use their respective coordinate times but we require the time shifts imposed on tangentially propagating light rays to be equal. Let's consider the perspective of an inertial observer in the laboratory frame observing the rotating platform that sends light for a round trip. The round trip for the light as seen by the inertial observer is obtained by considering the distance travelled by the co-moving light $L + vt = t$ where t is the total time of the round trip. Thus

$$\Delta t = \frac{L}{1-v} - L = \frac{2\pi r_t}{\sqrt{1-v^2}\,(1-v)} - \frac{2\pi r_t}{\sqrt{1-v^2}}, \tag{7.19}$$

where r_t is the turntable radius as seen by the inertial observer in the laboratory frame (note we have accounted for the time dilation). In the Kerr metric, as seen by a far-away observer the time of the round trip (w.r.t. to the stationary observer) around a massive planet is (we have used Eq. (7.3))

$$\begin{aligned}\Delta t_{Kerr} &\approx \frac{2\pi r}{1-\frac{r_s a}{r^2}-\frac{r_s}{2r}} - \frac{2\pi r}{1-\frac{r_s}{r}} \\ &\approx 2\pi r(1+\frac{r_s}{2r}+\frac{r_s a}{r^2}) - 2\pi r(1+\frac{r_s}{2r}) = \frac{2\pi r_s a}{r},\end{aligned} \tag{7.20}$$

where r is the radius in the Kerr metric. Equating these two far-away times ($\Delta t = \Delta t_{Kerr}$) and without assuming v is small, we have

$$\frac{r_s a}{r r_t} = \frac{1}{\sqrt{1-v^2}\,(1-v)} - \frac{1}{\sqrt{1-v^2}} = \frac{v}{\sqrt{1-v^2}}. \tag{7.21}$$

Thus we have the velocity

$$v = \frac{r_s a}{r r_t \sqrt{1 + \frac{r_s^2 a^2}{r^4}}} \approx \pm \frac{r_s a}{r r_t} \tag{7.22}$$

For example, for a turntable of radius $r_t = 0.2\ m$ and $r = r_E$ equal to the Earth's radius we have a turntable velocity of $v = \pm 0.8\ m/s$ or angular frequency $\Omega = 4\ rad/s$. Compared to the previous example of an Earth size turntable, the accumulated effect on the smaller turntable is smaller and thus the velocity must be larger to compensate. We note that if the turntable radius is equal to the Kerr metric radius $r_t = r$ and we use the metric times in Equations 7.14 and 7.16. We obtain the equation

$$\frac{r_s a}{r^2} \sqrt{\frac{1-v^2}{1-\frac{r_s}{r}}} = v, \tag{7.23}$$

which, solving for v is equivalent to Eq. (7.18). Therefore, we have proven that a transformation of time coordinates isn't necessary to quantitatively simulate the Kerr metric with a rotating turntable.

7.4.2 Phase

For a rotating reference frame, we solve for the light null geodesic to obtain the tangential velocity of light $\dot{x} = r\frac{d\phi}{dt}$. Setting $ds^2 = 0$ we have $(1-v^2) - 2v\dot{x} - \dot{x}^2 = 0$. We thus have two solutions $\dot{x} = 1 \pm v$. The cross term component $dtd\phi$ once again is the cause of the anisotropy of light. With the rotation of the turntable, the phase of the photon is $\Phi_A = \omega\frac{L}{c_A} = \omega\frac{L}{1+v}$ and against the rotation, with the phase $\Phi_B = \omega\frac{L}{c_B} = \omega\frac{L}{1-v}$. Thus the phase difference for the turntable is

$$\Delta\Phi_{Rotation} = \frac{2\omega v L}{1-v^2}, \tag{7.24}$$

which is the same phase obtained by a classical Sagnac interferometer.

7.4.3 Minimum velocity for significant visibility loss

We substitute the phase in Eq. (7.24) in Eq. (7.11) to obtain the visibility

$$\mathcal{V} = e^{-\sigma^2\frac{\Delta\phi^2}{\omega^2}} = e^{-4\frac{v^2 L^2 \sigma^2}{(1-v^2)^2}} = e^{-4\frac{v^2}{(1-v^2)}\pi^2 r^2 \sigma^2}. \tag{7.25}$$

Note that L is the total contracted length travelled by the light. For the case where the photons meet half way we have $L = \pi r\sqrt{1-v^2}$. For significant visibility loss the velocity needed for the rotating platform is given by solving $4\frac{v^2}{(1-v^2)}\pi^2 R^2\sigma^2 = 1$. Rearranging,

$$v_{min} = \frac{1}{\sqrt{4\pi^2 r^2\sigma^2 + 1}} \approx \frac{1}{2\pi r\sigma}. \tag{7.26}$$

Let's consider $\frac{\sigma}{c} = \frac{1}{\Delta t_p c} = 3.3\times 10^3\ m^{-1}$ corresponding to picosecond pulses and a rotating platform of radius $r = 5\ m$. Thus $v \approx \frac{1}{2\pi R\sigma} \approx 2900 m/s$. If smaller pulses of 100 femtoseconds are used then $v \approx 290 m/s$. The amount of g-force for this velocity is 1700 g. However, we can simply increase L by increasing the number of windings around the turntable, thus accumulating the effect, and making it significant for much lower velocities.

7.5 Two photons input (HOM interference)

In our thought experiment, we considered a superposition of a single photon travelling two paths. The probability of detection depends on the classical phase shift $\Delta\Phi$, and also the visibility of the quantum interference. The Hong-Ou-Mandel (HOM) interferometer uses two photons as input. However, in this setup, a physical time delay between the paths is explicit in the probability of detection. The loss of interference is due to loss of indistinguishability of the photons and has no classical analogue. The HOM effect can be interpreted as more quantum due to this strong quantum interference. Let's consider a source of single photons travelling paths A and B to a beamsplitter. The state after the beamsplitter becomes

$$\begin{aligned} a_1^\dagger a_2^\dagger e^{i\omega\Delta t}\left|0\right\rangle\left|0\right\rangle &\to \frac{1}{2}(a_3^\dagger + i a_4^\dagger)(a_4^\dagger + i a_3^\dagger)\left|0\right\rangle\left|0\right\rangle \\ &= \frac{e^{i\omega\Delta t} i}{2}(\left|2\right\rangle\left|0\right\rangle + \left|0\right\rangle\left|2\right\rangle), \end{aligned} \tag{7.27}$$

where $e^{i\omega\Delta t}$ is a global phase difference between the two modes. We thus have photon pair incidences at the final output of the beamsplitter. In this case the time delay doesn't affect the coincidence probability, since the photons are not distinguishable.

Now let's consider a source of photons with arbitrary frequency distributions $f(\omega_1)$ and $g(\omega_2)$ sending the initial state $\left|1\right\rangle\left|1\right\rangle = \int d\omega_1 f(\omega_1) a_1^\dagger(\omega_1) \int d\omega_2 g(\omega_2) a_2^\dagger(\omega_2) e^{-i\omega_2\Delta t}\left|0\right\rangle\left|0\right\rangle$

to a beamsplitter. The transformation is

$$\begin{aligned}
a_1^\dagger a_2^\dagger |0\rangle|0\rangle \to & \frac{1}{2}\int d\omega_1 f(\omega_1)(a_3^\dagger(\omega_1) + i a_4^\dagger(\omega_1)) \\
& \times \int d\omega_2 g(\omega_2)(a_4^\dagger(\omega_2) + i a_3^\dagger(\omega_3)) e^{-i\omega_2\Delta t}|0\rangle|0\rangle \\
& = \frac{1}{2}\int d\omega_1 f(\omega_1)\int d\omega_2 g(\omega_2) e^{-i\omega_2\Delta t} \\
& \times (i a_3^\dagger(\omega_1)a_3^\dagger(\omega_2) + a_3^\dagger(\omega_1)a_4^\dagger(\omega_2) \\
& - a_4^\dagger(\omega_1)a_3^\dagger(\omega_2) + i a_4^\dagger(\omega_1)a_4^\dagger(\omega_2))|0\rangle|0\rangle .
\end{aligned} \tag{7.28}$$

The detection probability of a photon pair in either mode is determined by modelling the detectors as having a flat frequency response with the projector $P_3 = \int d\omega a^\dagger(\omega)|0\rangle|0\rangle\langle 0|\langle 0|a(\omega)$. These calculations have been done in Ref. [9], and for photons of the same frequency distribution $f(\omega) = g(\omega)$, the probability is

$$P = \frac{1}{2} - \frac{1}{2}\int d\omega_1 |f(\omega_1)|^2 e^{-i\omega_1\Delta t}\int d\omega_2 |f(\omega_2)|^2 e^{i\omega_2\Delta t}. \tag{7.29}$$

For photons with Gaussian frequency distribution of pulse width σ, we evaluate Eq. (7.29) to obtain

$$P_{Gauss} = \frac{1}{2} - \frac{1}{2}e^{-\frac{\sigma^2\Delta t^2}{2}}. \tag{7.30}$$

For zero time delay $\Delta t = 0$, the photons are indistinguishable. At this point, the visibility $\mathcal{V} = Tr(\rho_a\rho_b)$ of the two photon states ρ_a, ρ_b is equal to the purity $Tr(\rho^2)$ of the two photons $\rho = \rho_b = \rho_a$ [9]. Thus the visibility is 100% which is known as the Hong-Ou-Mandel dip. The coincidence count drops to zero when the two input photons are completely identical. For the case of the rotating turntable, the photons will become more distinguishable as Δt increases. The velocity at which this becomes significant is the same as in Eq. (7.26) since the visibility is the same and the time delay is $\Delta t = \frac{4vL}{1-v^2}$.. We can calibrate the dip for 100 % visibility using a controlled time delay in one of the arms and vary the rotational velocity of the turntable.

Compared to using a single photon interferometer, the HOM interferometer is based on the indistinguishability of the photons interfering with each other. As in Ref. [2], the HOM effect measures a physical time delay as opposed to a phase shift.

7.5.1 Two-way velocity of light

Similarly to the Kerr metric, the two-way velocity of light as measured by the inertial observer on the rotating turntable should be isotropic. Let's now consider a double sided mirror that reflects both of the light beams back to the original source. In this case, our phase difference is $\phi'_A = \phi_A + \frac{\omega L}{c_B} = \omega L(\frac{1}{1+v} + \frac{1}{1-v}) = \frac{2\omega L}{1-v^2}$ but $L = \pi R\sqrt{1-v^2}$. Therefore $\phi'_A = \frac{2\omega L}{\sqrt{1-v^2}}$. Similarly, for the counter-propagating beam of light $\phi'_B = \phi_B + \frac{\omega L}{c_A} = \omega L(\frac{1}{1-v} + \frac{1}{1+v}) = \phi'_A$. Thus the phase difference is zero. In other words, the "two-way velocity" of light is isotropic and $c = 1$. This demonstrates that observers riding on the turntable would also measure $c = 1$ between points around the circumference.

7.6 Dispersion effects in optical fibre

In a medium, the dispersion relation describes the relation of the frequency ω to its wavenumber k. The dispersion relation is Taylor expanded as $\omega(k) = \omega(k_0) + (k-k_0)v_g + \frac{1}{2}(k-k_0)^2\frac{d^2\omega}{dk^2}$ where $v_g = \frac{1}{\alpha} = \frac{d\omega}{dk}$ is the group velocity and $\frac{1}{\beta} = \frac{d^2\omega}{dk^2}$ is the inverse group velocity dispersion. Obviously for linear dispersion $\omega = \frac{k}{n}$ implying $\frac{d^2\omega}{dk^2} = 0$ and the group velocity $v_g = \frac{1}{n} = v_p$.

In relativity, the phase velocities of light in a medium in the stationary reference frame of the laboratory transform according to the Lorentz transformations.

7.6.1 Lorentz transformations in a moving medium

We consider using fibre optic cable to guide the photon half-way around the turntable as seen in Fig. 7.2. In a medium, the velocity of light is slowed down by the factor $1/n$ where n is the refractive index. The velocity of light in the medium depends on direction of the rotation relative to the observer in the laboratory reference frame.

According to the velocity composition law, for a moving medium, the velocity of light as seen in the laboratory reference frame of the rotating reference frame is

$$c_A = \frac{\frac{c}{n} - v}{1 - \frac{v}{cn}}, \tag{7.31}$$

which is equivalently the phase velocity. Therefore, $L - vt = t\frac{\frac{c}{n}-v}{1-\frac{v}{cn}}$, and $t = \frac{L(n-v)}{1-v^2}$ implying that the velocity of light is $c'_A = \frac{1-v^2}{n-v}$. Then we can approximate $c'_A = \frac{1-v^2}{n+v}$. Similarly, $c'_B = \frac{1-v^2}{n-v}$.

7.6.2 Phase velocity

Using the phase velocity in Eq. (7.31), the new phase is therefore $\Delta\Phi = \omega_0(\frac{L}{c'_A} - \frac{L}{c'_B}) = \frac{2v}{1-v^2}\omega_0 L$. Coincidentally, the final phase doesn't depend on the

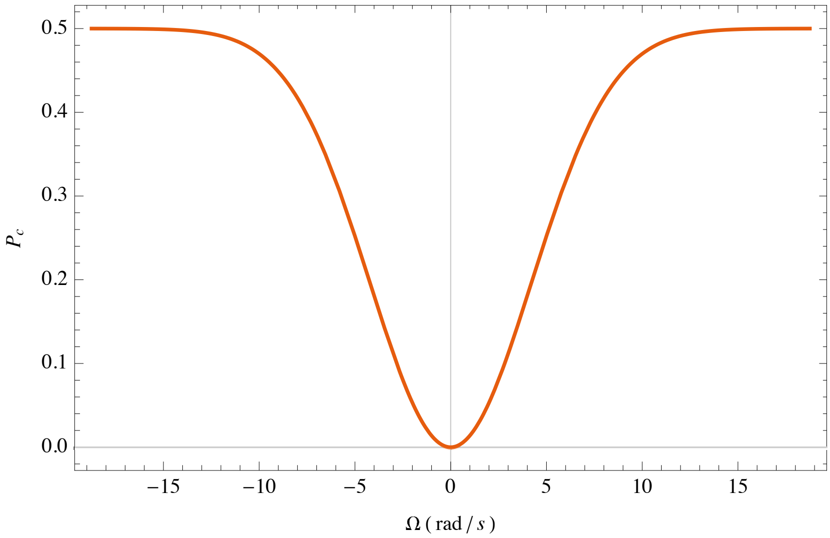

Figure 7.3: Probability of photon detection with angular frequency of turntable for parameters $L = 10\ km$, $R = 20\ cm$ and $\sigma = 4000\pi$.

refractive index if the fibres are equal length L. However, if these are unequal $L_A = L$ and $L_B = L + \Delta L$, then $\Delta\Phi' = \Delta\Phi + \omega_0 \Delta L \frac{n}{1-v^2}$. The HOM dip will measure the time delay $\Delta t' = \frac{4vL+2n\Delta L}{1-v^2}$. If ΔL is on the length scale of the coherence length then we can simply cancel this out with a controlled time delay.

As in Fig. 7.3, a time delay initially sets the visibility to 100% with the turntable at rest. The turntable is slowly rotated and the visibility decreases to 0%. The HOM dip will be initially centered around $v = 0$ where $\Delta t'_0 = 2\Delta L n + \Delta t_{Control} = 0$. Thus as the turntable is slowly rotated we have

$$\begin{aligned} \Delta t' &= \frac{4vL}{1-v^2} + 2\Delta L \frac{n}{1-v^2} - 2\Delta L n \\ &\approx \frac{4vL}{1-v^2} + 2\Delta L n v^2. \end{aligned} \tag{7.32}$$

There is as shift in the centre of the HOM dip. ΔL depends on the experimental error of the measured fibre lengths and the velocity of the turntable. For example, for a slowly rotating turntable of $\Omega = 2\pi\ rad/s$ and $R = 20\ cm$, a mismatch in the length of the optical fibres of $\Delta L = 1\ cm$ would shift the HOM dip by $\Delta t_{Error} = 2\Delta L n v^2 \approx 3 \times 10^{-11}\ s$ or relative to the leading term $\frac{\Delta t_{Error}}{\Delta t} = \frac{\Delta L n v}{2L} \approx 3 \times 10^{-11}$ smaller. Since v is extremely small, the propagated error in the time difference and thus the zero point of the HOM dip would be negligible.

7.6.3 Coherence length of photons

We note that we can extend the time of rotation by increasing windings and therefore $L' = (2N+1)\pi R\sqrt{1-v^2}$ where N is the number of windings. Thus the visibility for very slow rotation becomes $\mathcal{V} = e^{-4\frac{v^2}{1-v^2}(2N+1)^2\pi^2R^2\sigma^2}$. Thus far, we have been assuming timed pulses of light. Alternatively, the source of down-converted photons could be continuous characterized by a coherence length. Note that the coherence length is defined as $\Delta x = \frac{2\pi}{\sigma}$ where σ is the width in frequency space. We consider parameters of $v = \frac{\Omega R}{c}$ where $R = 20\ cm$ and $\Omega = 2\pi\ Hz$ with optical fibre of length $L' = 10\ km$. Therefore, the coherence length needed for significant visibility loss is $\Delta x = 4\pi L'\frac{\Omega R}{c} \approx 500\ \mu m$ which is the typical coherence length of down-converted photons. In the next section, we will consider a quasi-continuous source and the effect of dispersion.

7.6.4 Dispersion cancellation

We've seen that the phase velocity isn't affected by the relativity of the co- and counter- propagating light for fibre of equal length. However, we now consider the full treatment of the effects of dispersive broadening and the group velocity. In a moving medium, the phase velocity of light for co- and counter- propagating light is given by

$$v_{p\pm} = \frac{\omega}{k} = \frac{1-v^2}{n(k) \mp v}, \tag{7.33}$$

and the group velocity is given by

$$v_{g\pm} = \frac{1}{\alpha_\pm} = v_{p\pm} - \frac{dn(k)}{dk}\frac{1-v^2}{(n(k)\mp v)^2} = v_{p\pm}(1 - \frac{n'(k)}{n(k)\mp v}), \tag{7.34}$$

where $\alpha_\pm = \frac{dk}{d\omega}$ is the inverse group velocity. The second order effect responsible for broadening is

$$\frac{d^2\omega}{dk^2} = \frac{1}{\beta_\pm} = v_{g\pm} - v_{p\pm} - \frac{d^2n(k)}{dk^2}\frac{1-v^2}{(n(k)\mp v)^2} + 2(\frac{dn(k)}{dk})^2\frac{1-v^2}{(n(k)\mp v)^3}, \tag{7.35}$$

where the group velocity dispersion (GVD) is defined as $\beta = \frac{d^2k}{d\omega^2}$. For example, for fused silica, the index of refraction is approximately linear with the wavelength. Thus as a function of k, $n(k) = \frac{100000}{k} + 1.44$ around the wavenumber $k_0 = 8\times10^6$ m^{-1}. Thus $n(k_0) = 1.453$ and the derivative is $\frac{dn(k_0)}{dk} = -\frac{10^5}{k_0^2} = -1.6\times10^{-9}\ m$. The second derivative is $\frac{d^2n(k_0)}{dk^2} = \frac{2\times10^5}{k_0^3} = 4\times10^{-16}\ m^2$. Thus $\frac{d^2\omega}{dk^2} \approx 1\times10^{-9}\ m^2/s^2$.

Let's consider the following quasi continuous wave input state of down-converted light

$$|\psi\rangle = \int d\omega' f(\omega') \, |\omega_0 + \omega'\rangle_A \, |\omega_0 - \omega'\rangle_B. \tag{7.36}$$

After passing through the beamsplitter the modes in the two arms 1 and 2 are

$$\begin{aligned} a_1(\omega_1) &= \frac{i}{\sqrt{2}} a_A(\omega_1) e^{ik_A(\omega_1)L} + \frac{1}{\sqrt{2}} a_B(\omega_1) e^{ik_B(\omega_1)L}, & (7.37) \\ a_2(\omega_2) &= \frac{i}{\sqrt{2}} a_B(\omega_2) e^{ik_B(\omega_2)L} + \frac{1}{\sqrt{2}} a_A(\omega_2) e^{ik_A(\omega_2)L}, & (7.38) \end{aligned}$$

where $k_A = k_0 + \alpha^+(\omega - \omega_0) + \beta^+(\omega - \omega_0)^2$ is the wavenumber of the co-propagating light as by the laboratory reference frame. Similarly, $k_B = k_0 + \alpha^-(\omega - \omega_0) + \beta^-(\omega - \omega_0)^2$ is the counter- propagating light.

As in Ref. [5], we assume a gate window time that is much larger than the dispersive broadening. This implies that cross terms of annihilation operators at different frequencies disappear for sufficiently long detector time scales. Thus the probability P_c is

$$P_c \propto \int d\omega_1 \int d\omega_2 \, \langle\psi| a_1^\dagger(\omega_1) a_2^\dagger(\omega_2) a_1(\omega_1) a_2(\omega_2) |\psi\rangle \, . \tag{7.39}$$

As it turns out, the phase term $\beta(\omega - \omega_0)^2$ acquired is the same in both interferometer arms due to the condition that $\omega_p = \omega_A + \omega_B$. The kernel is

$$\begin{aligned} &\langle\psi| a_1^\dagger(\omega_1) a_2^\dagger(\omega_2) a_1(\omega_1) a_2(\omega_2) |\psi\rangle \\ =&|\frac{1}{2}\delta(\omega_p - \omega_1 - \omega_2) f(\omega')[e^{ik_B(\omega_1)L + ik_A(\omega_2)L} - e^{-ik_B(\omega_2)L - ik_A(\omega_1)L}]|^2 \\ =& \, |\frac{1}{2}\delta(\omega_p - \omega_1 - \omega_2) f(\omega')[e^{i(\Delta\alpha\omega' + \beta'\omega'^2} - e^{i(-\Delta\alpha\omega' + \beta'\omega'^2)L}]|^2, \end{aligned} \tag{7.40}$$

where $\Delta\alpha = \alpha^+ - \alpha^-$ and $\beta' = \beta_A + \beta_B$. Evaluating the absolute squares

$$P_c = \int d\omega' |f(\omega')|^2 (1 - \cos{(2\omega'\Delta\alpha L)}). \tag{7.41}$$

This gives the usual phase but with a correction

$$\Delta\phi_{v_g} = 2\omega' L (\frac{1}{v_g^-} - \frac{1}{v_g^+}) \approx \frac{4\omega_0 v L}{1 - v^2}(1 + \frac{n'(k_0)v}{1 - v^2}), \tag{7.42}$$

where $\omega' = \omega_1 - \omega_0 = \omega_0 - \omega_2$. Thus, as expected when the index of refraction is a constant $v_g = v_p$ and $n'(k_0) = 0$ we obtain the usual phase shift with the cancellation of the refractive index. The correction is negligible for an $L = 10 \; km$ long fibre at extremely slow rotation of $\Omega = 2\pi \; Hz$ and radius $R = 20 \; cm$. For optical fibre $n'(k_0) = -10^{-9} \; m$, which is much less than unity.

Let's consider the frequency distribution $|f(\omega')|^2 = (\frac{1}{\pi\sigma^2})^{1/2}\exp(-\frac{\omega'^2}{\sigma^2})$. The probability is therefore

$$\begin{aligned} P_c &= \int d\omega'|f(\omega')|^2(1-\cos{(2\omega'\Delta\alpha L)}) \\ &= \frac{1}{2}(1-\exp{(-4\sigma^2(\frac{vL}{1-v^2}(1+\frac{n'(k_0)v}{1-v^2}))^2)}). \end{aligned} \tag{7.43}$$

Thus, we have the visibility with the corrected time delay from the group velocity. Ultimately, the effect of dispersion due to the material is cancelled out, and the group velocity effect is far too small ($n'(k) \approx -10^{-9}$ in silicon fibre) for the parameters suggested. For unequal lengths of the optical fibre, the phase term due to the index of refraction can be cancelled out using a time delay.

7.7 Conclusion

We have shown how to measure the visibility loss of interfering paths of a photon travelling in the Kerr metric. The Kerr effect manifests as a classical phase but the effect of Kerr time dilation can be measured by the visibility of the detection probability. We have analogously shown that the metric for light travelling around a turntable is the same. We can directly measure the time delay and loss in the visibility of quantum interference using a HOM Sagnac interferometer. Dispersion in the optical fibre cancels out and the difference in group velocity is negligible for the parameters considered. Photons can be treated as if travelling in free space. We thus propose an experiment that will detect a relativistic effect in a quantum mechanical setting. We find realistic parameters for a feasible experiment with current quantum technology.

Acknowledgements. We thank Matthias Fink and Rupert Ursin from the Institute for Quantum Optics and Quantum Information of the Austrian Academy of Sciences for discussions of potential experimental set ups. This work was supported in part by the Australian Research Council Centre of Excellence for Quantum Computation and Communication Technology (Project No. CE110001027) and financial support by an Australian Government Research Training Program Scholarship.

Bibliography

[1] *General relativistic effects in quantum interference of photons*, Magdalena Zych, Fabio Costa, Igor Pikovski, Timothy C. Ralph and Caslav Brukner, Class. Quantum Grav. **29** 224010 (2012).

[2] *Phase shifts vs time delays: Sagnac and Hong-Ou-Mandel*, S. J. van Enk, arXiv preprint: arXiv:1104.0970(2011).

[3] *Single-photon Sagnac interferometer*, G. Bertocchi, O. Alibart, D.B. Ostrowsky, S. Tanzilli and P. Baldi, J. Phys. B: At. Mol. Opt. Phys. **39**, 1011-1016 (2006).

[4] *Entanglement-enhanced optical gyroscope*, Matthias Fink, Fabian Steinlechner, Johannes Handsteiner, Jonathan P. Dowling, Thomas Scheidl, Rupert Ursin, arXiv preprint: arXiv:1810.02213 (2018).

[5] *Dispersion cancellation and high-resolution time measurements in a fourth-order optical interferometer*, Aephraim M. Steinberg, Paul G Kwiat and Raymond Y. Chiao, Phys Rev A. **1**;45(9):6659-6665 (1992).

[6] *The Kerr spacetime: a brief introduction*, D.L. Wiltshire, M. Visser and S.M. Scott eds., Cambridge University Press, Cambridge, U.K. (2009).

[7] *Quantum metrology in the Kerr metric*, S. P. Kish, T. C. Ralph, Phys. Rev. D **99**, 124015 (2019).

[8] *Measurement of subpicosecond time intervals between two photons by interference* C. K. Hong, Z. Y. Ou, and L. Mandel, Phys. Rev. Lett. **59**, 2044 (1987).

[9] *Hong-Ou-Mandel Interference*, A. M. Branczyk, arXiv preprint: arXiv:1711.00080 (2017).

Chapter 8

Conclusion

In this chapter, we consider the unanswered questions that could motivate future research. Finally, we conclude the thesis by summarizing our work and the impact of our research in a broader context.

8.1 Future outlook and open questions

1. *What are the optimal measurements for lossy Gaussian quantum channels?* In Chapter 4, we have assumed that the measurement basis is optimal for the lossy quantum channel. We have not specified the exact basis, and whether this is experimentally feasible. Although we have some clues that the basis must be Gaussian as in Chapter 4.6.4 and one must also have *a priori* knowledge of the parameter that needs to be estimated. Nonetheless, the question remains open.

2. *How else can we use the nonlinear interferometer?* We could potentially consider the same nonlinear interferometer in Chapter 5 in the Kerr metric. Since the time dilation couples to the nonlinearity in the same way as the Schwarzschild time, we would have similar scaling and quantum limits for the Kerr parameter a. Additionally, we note that Ref. [2] explores to measure the nonlinear phase shift in traversable wormhole metrics using the same nonlinear interferometer. The calculations by the authors are based upon work done by us.

3. *Does an anisotropy of light arise in radial null geodesics that could be detected by SU(1,1) interferometers?* In Chapter 3.3.1, we can see that metrics of the

ingoing and outgoing photons in the Eddington-Finkelstein coordinates have cross terms $dvdr$ and $dudr$. This would result in the null geodesics having an anisotropy in the speed of light.

It could be instructive to consider the SU(1,1) interferometer in Ref. [1] which essentially measures the proper time of a photon that does a round trip in a gravitational field. In this case, the phase difference is related to $\frac{h^2}{r^2}$ as opposed to the area of the Mach-Zehnder interferometer $\frac{hL}{r^2}$. We can consider whether we obtain the same phase difference but instead of considering the proper time in the Schwarzschild metric, we would make use of the null geodesics in the ingoing/ outgoing Eddington-Finkelstein metrics of a black hole.

4. *How does Unruh or Hawking temperature affect the quantum limits of acceleration or Schwarzschild parameters?* A major result from quantum field theory for accelerating observers and observers in curved space-time is the non-uniqueness of the vacuum state [3]. The vacuum state of an accelerating observer is defined with respect to Rindler modes which transform to the Unruh modes [5]. Unruh modes correspond to positive-frequency superpositions of Minkowski modes via a Bogoliubov transformation. Unruh's prediction is that an accelerating detector will observe a thermal bath with temperature given by [4]

$$T_{Unruh} = \frac{\hbar a}{2\pi c k_B}, \tag{8.1}$$

where a is the proper acceleration. The Rindler space-time has an event horizon which is locally equivalent to that of a non-extremal black hole. Thus, the Unruh thermal radiation would be the Hawking radiation near the horizon but with the acceleration equal to the gravitational acceleration g. A question arises on whether the thermal radiation affects the fundamental quantum limit on parameter estimation of the proper acceleration a or the Schwarzschild radius r_s. This would essentially require the interaction of the probe with the thermal environment.

5. *How does metric backaction affect the quantum limits of strong lasers?* Thus far, we have considered the space-time background to be classical and photons are quanta of the electromagnetic field. This forms the semi-classical approximation. However, in the regime of dense high energy photons, we enter a regime that necessitates space-time to be quantized. The energy fluctuations would be high enough to "gravitate". That is, the energy-momentum tensor in the Einstein equation is a quantum operator. In the semi-classical regime, fundamental

quantum limits have been determined for the speed of light c in a cavity in Ref. [6]. However, the speed of light was interpreted as an energy dependent dispersion effect, and is a classical effect from general relativity. This is a consequence of taking the quantum mechanical expectation value of the energy-momentum tensor $T^{\mu\nu}$. Any back-action on the metric due to large numbers of photons and their fluctuations were disregarded. This motivates the open question: *How does metric backaction affect the quantum limits of strong lasers?* An approach to answering this question is using stochastic gravity [7].

8.2 Conclusion

The aim of this thesis is to provide the building blocks of unprecedented high precision measurements in the overlap of quantum physics and general relativity. We have hoped to establish the tools of quantum metrology applied to curved space-time to an audience familiar only with undergraduate physics. Throughout the thesis, we had made use of the definition of the Quantum Fisher Information related to the Bures distance. This allowed us to easily derive ultimate quantum bounds on estimation of parameters without the knowledge of the optimal measurement basis. Subsequently, as in Chapters 4, 5 and 6 we applied this to calculate bounds on the space-time parameters of the Schwarzschild and Kerr metrics. With these tools, we can essentially design a quantum channel which encodes a space-time parameter unitarily and allows us to easily determine the error scalings.

To summarize, in Chapter 4, we applied quantum metrology techniques to the estimation of the Schwarzschild radius r_s. We showed the optimal energy resources and squeezing that are needed for light propagating in the Schwarzschild space-time of Earth including the inevitable losses due to atmospheric distortion. This would provide useful tools for Earth to satellite based quantum experiments, and will be essential for designing continuous variable protocols for parameter estimation of space-time parameters in lossy channels.

In Chapter 5, we proposed a new quantum interferometer using higher order Kerr nonlinearities to improve the sensitivity of estimating r_s. In principle, we would be able to downsize linear interferometers and probe gravity over a small scale potentially making it practical for measuring gravitational gradients. Also, the robustness against loss of this protocol can be used to design protocols in lossy free-space channels.

In Chapter 6, we studied the interesting features of the metric around a rotating massive body known as the Kerr metric. We made use of the anisotropy of light to measure the Kerr rotation parameter a. We determined the quantum limits of estimating this parameter. As a possible implementation, we considered a stationary Mach-Zehnder interferometer set at a dark port that measures a phase due to the anisotropy of light. Additionally, we found a geometry of the interferometer which cancels out the phase due to the Earth's rotation.

In Chapter 7, we studied the quantum effects of single photon systems in the Kerr metric and rotating reference frames. We considered the superposition of a co- and counter- propagating photon around the Kerr space-time of a rotating planet. We have proven that we can simulate this space-time using an inertially rotating reference frame i.e. a rotating turntable. We proposed to use the Hong-Ou-Mandel (HOM) effect to measure the visibility loss of quantum interference due to the time difference between co- and counter- propagating photons on a rotating turntable. The importance of this is that a relativistic effect due to rotation has not yet been observed in a purely quantum mechanical setting.

Ultimately, future quantum technologies will become more precise, and will enter a new regime where general relativistic effects can be measured. The application of quantum metrology to the estimation of space-time parameters as we have done, will hopefully contribute to this effort. Our results could also help with the building of future space-based experiments and Earth to satellite quantum communication.

Bibliography

[1] *Estimation of gravitational acceleration with quantum optical interferometers*, S. Y. Chen, T. C. Ralph, Phys. Rev. A **99**, 023803 (2019).

[2] *Parameter Estimation of Wormholes beyond the Heisenberg Limit*, C. Sabin, C. S. Vaca, Universe **4**, 115 (2018).

[3] *Quantum Field Theory in Curved Spacetime*, L. H. Ford, arXiv:gr-qc/9707062 (1997).

[4] *Notes on black-hole evaporation*, W. G. Unruh. Phys. Rev. D, **14**:870892 (1976).

[5] *Cavity mode entanglement in relativistic quantum information*, N. Friis, arXiv:1311.3536 (2013).

[6] *Intrinsic measurement errors for the speed of light in vacuum*, D. Braun, F. Schneiter, U. R. Fischer, Class. Quantum Grav. **34**, 175009 (2017).

[7] *Stochastic Gravity: Theory and Applications*, B.L. Hu, E. Verdaguer, Living Rev. Relativity **11** 3 (2008).

When you look at yourself from a universal standpoint, something inside always reminds or informs you that there are bigger and better things to worry about.

-Albert Einstein (Excerpt from *The World as I See It* translated by A. Harris and published in 1935 by John Lane The Bodley Head (London))